ICES J. mar. Sci., 52: 67–75. 1995

Comparison of equal-area cylindrical and circular piston transducers

Kenneth G. Foote

Foote, K. G. 1995. Comparison of equal-area cylindrical and circular piston transducers. – ICES J. mar. Sci., 52: 67–75.

Design of sondes for *in situ* measurement of zooplankton or other scatterers requires choosing among alternative transducer geometries. This contribution addresses the problem of choosing between cylindrical and circular piston transducers by comparing the performance of the two according to the principle that the acoustically active areas be equal. Computations are performed with the actual dimensions of six fabricated cylindrical transducers, whose beam patterns have been measured by the manufacturer at a total of 11 frequencies spanning the range 27–710 kHz. Nominal power levels assigned to the cylindrical transducers are also used for both transducer types. Comparison of theoretically computed beam patterns with measurement gives confidence in the radiation model, which is used to compute the directivity index and on-axis sensitivity loss due to curvature of the cylindrical transducers, referred to as the curvature loss. Under identical conditions of excitation, isotropic ambient noise, and detection threshold of 20 dB, the active sonar equation is exercised to estimate the maximum detection range of both single targets and multiple targets distributed throughout the sampling volume. In every single case, the performance of the equal-area circular piston is superior to that of the corresponding cylindrical transducer. This is directly attributable to differences in directivity index and curvature loss. Other, pragmatic considerations argue for the choice of the circular piston transducer over the cylindrical transducer. Three problems requiring future treatment are identified.

Key words: acoustic sonde, transducers, zooplankton, beam patterns.

Received 21 April 1994; accepted 17 November 1994.

K. G. Foote: Institute of Marine Research, PO Box 1870, Nordnes, N-5024 Bergen, Norway

Introduction

For some years there has been discussion on the use of cylindrical transducers on a sonde for the *in situ* measurement of zooplankton or other scatterers. An alternative is that of circular piston transducers, as used, for example, in Holliday's renowned multifrequency acoustic profiling system (MAPS) (Holliday *et al.*, 1989).

Here the ordinary active sonar equation is exercised in an ambient-noise-limited environment to compare the performance of cylindrical and circular piston transducers. An important analysis principle is that the acoustically active areas of corresponding transducers at the same frequency be equal.

Another analysis principle is use of the dimensions of cylindrical transducers as fabricated, for which the manufacturer's beam pattern measurements are available, as well as use of nominal power levels attached or assigned to the transducers. This removes some of the abstractness of the *a priori* argument compared to the partly *a fortiori* argument advanced here. This is additionally valuable for resolving somewhat a technical matter concerned with the acoustic boundary condition on the cylindrical transducer, which is generally unknown and difficult to know, but is clearly different from that which usually applies on the planar circular piston transducer.

Transducer geometries and dimensions

The idealized form of the cylindrical transducer is a right circular cylinder of length l and outer dimension 2a. The acoustically active area is thus $2\pi al$.

The circular piston transducer is assumed to be a planar circular surface of radius s set in an infinite baffle. By assumption of equal area with the respective cylindrical transducer, $\pi s^2=2\pi al$ or $s=(2al)^{1/2}$.

Six cylindrical transducers were fabricated by International Transducer Corporation, Santa Barbara, California, no later than 1988, with ITC Model no. 8151, Serial no. 001. Because of their planned sequential alignment, or stacking, on a common axis for use on a

1054–3139/95/010067+09 $08.00/0

Table 1. Transducer dimensions and nominal electrical power levels.

Section	Frequencies (kHz)	Cylinder			Piston radius (mm)	Power (W)
		Length (mm)	Diameter (mm)	Area (mm^2)		
A	27, 38	204.5	34.8	22 351	84.3	600
B	70, 88	88.8	24.2	6761	46.4	400
C	107, 120, 150	58.0	13.2	2400	27.6	200
D	200, 250	33.6	34.3	3619	33.9	150
E	375	25.3	25.5	2028	25.4	50
F	710	11.5	14.0	506	12.7	20

sonde, the transducers were referred to as "sections" by the manufacturer. The transducer associated with Section A was intended to be driven at each of two frequencies, 27 and 38 kHz. Section B was intended to be driven at 70 and 88 kHz, C at 107, 120, and 150 kHz, D at 200 and 250 kHz, E at 375 kHz, and F at 710 kHz.

Maximum overall dimensions of the six transducers, as read off ITC engineering drawing no. 017110, dated 15 April 1988, are presented in Table 1. Computed radii of corresponding equal-area circular pistons are also shown, as are nominal electrical power levels assigned to the cylindrical transducers and assumed for the corresponding circular piston transducers too.

Beam patterns

The beam pattern is defined in terms of the transmitting or receiving amplitude of the transducer. For a planar transducer, the amplitude in the farfield when transmitting is identical with that due to receiving from a source in the farfield, namely:

$$f=A^{-1}\int_A \exp(i\mathbf{k}\cdot\mathbf{r})\,dS, \tag{1}$$

where A is the acoustically active area of the transducer, **k** is the wavevector, and **r** is the position vector of the area element dS on the transducer surface. The integration is performed over the entire transducer surface.

The same expression could also apply in the idealized case of an acoustically transparent transducer of arbitrary shape, or one in which the field at any differential surface element dS is essentially unaffected by the presence of other elements. This case cannot be realized in general, for inasmuch as the element does respond to sound, it also changes the sound field, hence affects the field at other elements.

Cylindrical transducer

In the present case of a cylindrical transducer, a condition of acoustic opacity is considered realistic. Accordingly, sound is radiated outwards or received from the exterior, without internal radiation or transmission. This boundary condition is represented by an individual element directivity function to be introduced in Equation (1).

It is convenient to refer both **k** and **r** in Equation (1) to the same rectangular co-ordinate system. For a cylinder of constant radius a and length l, the position of a surface element may be described in cylindrical co-ordinates by the radius a, azimuth φ relative to the direction of evaluation, and height z relative to the horizontal plane bisecting the cylinder, hence $\mathbf{r}=(a\cos\varphi, a\sin\varphi, z)$. The direction of evaluation $\hat{k}$ is represented by the polar angle θ relative to the transducer axis and azimuth $\varphi=0$, hence $\hat{k}=(\sin\theta, 0, \cos\theta)$, and $\mathbf{k}\cdot\mathbf{r}=k(a\sin\theta\cos\varphi+z\cos\theta)$. The surface element has area $dS=a\,d\varphi\,dz$.

In this same co-ordinate system, the individual element directivity function at **r** is represented by the function cos φ, where φ is in the horizontal plane, for $-\pi/2<\varphi<\pi/2$, and 0 for $|\varphi|\geq\pi/2$. This is introduced into Equation (1) as a multiplicative factor attached to the surface element dS. Equation (1) is thus generalized:

$$f=A^{-1}\int_{-l/2}^{l/2}\int_{-\pi/2}^{\pi/2}\exp(i\mathbf{k}\cdot\mathbf{r})\cos\varphi\,a\,d\varphi\,dz, \tag{2}$$

where A is now the effective, acoustically active area of the transducer, namely:

$$A=\int_{-l/2}^{l/2}\int_{-\pi/2}^{\pi/2}\cos\varphi\,a\,d\varphi\,dz=2al. \tag{3}$$

In order to perform the integration in Equation (2), it is useful to note the respective definitions of Anger's and Weber's functions (Abramowitz, 1965):

$$\mathbf{J}_\nu(z)=\pi^{-1}\int_0^\pi \cos(\nu u-z\sin u)\,du, \tag{4a}$$

$$\mathbf{E}_\nu(z)=\pi^{-1}\int_0^\pi \sin(\nu u-z\sin u)\,du. \tag{4b}$$

The result of the integration is thus:

$$f=\frac{\sin\left(\frac{kl}{2}\cos\theta\right)}{\frac{kl}{2}\cos\theta}\,\frac{\pi}{2}\,i[\mathbf{J}_1\,(ka\sin\theta)-i\mathbf{E}_1\,(ka\sin\theta)].\quad(5)$$

This can be reduced further, for the function $\mathbf{J}_1\,(\zeta)$ is just the ordinary Bessel function of order 1, $J_1(\zeta)$, and $\mathbf{E}_1\,(\zeta)=2/\pi-\mathbf{H}_1\,(\zeta)$, where $\mathbf{H}_1\,(\zeta)$ is the Struve function of order 1.

Equation (5) is quite interesting in the present context. In the long-wavelength limit, $f(\pi/2)=1$. At shorter or finite wavelengths, $f(\pi/2)<1$. This can be understood in terms of Fresnel zones (Neubauer, 1963; Born and Wolf, 1970): because of the curvature of the transducer surface, the number of zones increases with decreasing wavelength, or increasing frequency. Because of the destructive effect of an increasing number of zones, the sensitivity of the transducer decreases with increasing frequency. This loss of sensitivity is measured by $f(\pi/2)$. It is connected with the so-called diffraction constant (Henriquez, 1964; Bobber, 1965; Milosić, 1993).

In computing the beam pattern of the acoustically opaque cylinder, therefore, the lack of normalization in f is to be remembered. The beam pattern is consequently:

$$b=\left|\frac{\sin\left(\frac{kl}{2}\cos\theta\right)}{\frac{kl}{2}\cos\theta}\right|^2\frac{\mathbf{J}_1^2\,(ka\sin\theta)+\mathbf{E}_1^2\,(ka\sin\theta)}{\mathbf{J}_1^2\,(ka)+\mathbf{E}_1^2\,(ka)}\qquad(6)$$

Another candidate boundary condition, not considered here, is that of the rigid but infinite cylinder, as described by Morse (1948). Notwithstanding description of radiation by an arbitrary azimuthal distribution of the normal component of surface velocity, it is not clear how this can be applied to the problem of transmission and reception by a cylindrical transducer of finite length.

The complicated nature of the boundary condition is illustrated by Ho (1994) for the case of an elastic cylindrical shell. The distribution of total surface pressure in azimuth is clearly non-uniform for the chosen wavenumber-radius product ka=3.05. Fundamental physical reasons for the complexity of this surface distribution, hence boundary condition too, are elaborated by Ho (1993).

Circular piston transducer

For the planar circular piston transducer of radius s in an infinite perfect baffle, the farfield beam pattern is just:

$$b=\left|\frac{2J_1\,(ks\sin\theta)}{ks\sin\theta}\right|^2\quad\text{for }\theta<\pi/2,\qquad(7)$$

and 0 otherwise. Here θ is the polar angle describing the field direction relative to the acoustic axis, which is coincident with the physical axis.

Beam pattern parameters

Several quantities are useful for describing the beam patterns of cylindrical transducers. In the longitudinal plane, including the transducer axis, these are the (1) half-width $\Delta\theta$ of the main lobe, measured from the axis to the angle at which $10\log b=-3$ dB; (2) angle θ_1 between cylinder axis and first sidelobe, or its complement $\pi/2-\theta_1$; and (3) beam pattern level at the angle θ_1, $B_1=10\log b\,(\theta_1)$. In the transverse plane, perpendicular to the transducer axis, a useful quantity is the total variation in the beam pattern with respect to the azimuthal angle, $\Delta B=10\log\{\text{Max } b_\varphi(\pi/2)\}-10\log\{\text{Min } b_\varphi(\pi/2)\}$.

For the cylindrical transducers fabricated by the International Transducer Corporation, the beam patterns were measured by the manufacturer in August 1988 over 360 degrees in both the longitudinal and transverse planes. By symmetry, each of the first three enumerated quantities is determined by four values. The four beam pattern parameters are presented in Table 2. Included with the values derived from the beam pattern plots are the corresponding results of theoretical computation based on the measured, maximum overall cylindrical transducer dimensions given in Table 1. In fact, each of transducer sections A, B, and C, covering the frequency range 27–150 kHz, is a stacked array of identical cylindrical elements. The spacing between adjacent elements is small and is consequently neglected. In the computations, the sound speed is assumed to be 1481.8 m/s (Mackenzie, 1981), as the ITC measurements were made in a freshwater tank at 20°C, at depth 1.5 m. By symmetry, the theoretical value for ΔB in the transverse plane is zero, hence is not shown.

Sonar model

Two performance measures are chosen for comparison of the equal-area cylindrical and circular piston transducers. These are the maximum detection ranges for single targets and multiple targets distributed throughout the sampling volume. The maximum detection range is computed by means of the active sonar equation with ambient-noise-limited conditions, assuming a constant detection threshold of 20 dB. Details are given here.

Source level

The usual equation for source level (Clay and Medwin, 1977) requires generalization to non-planar transducers

Table 2. Beam pattern parameters of six cylindrical transducers at 11 frequencies. The measured half-beamwidth $\Delta\theta$ and angle $\pi/2-\theta_1$ of first sidelobe relative to the broadside plane are each averages of the four corresponding values. The range of measured values of the first sidelobe level B_1 is given. In the single case of the transducer at 710 kHz, θ_1 and B_1 could not be determined because of the irregular shape of the beam pattern. The assumed sound speed in the computations is 1481.8 m/s.

Frequency (kHz)	$\Delta\theta$ (deg)		$\pi/2-\theta_1$ (deg)		B_1 (dB)		ΔB (dB) meas.
	Meas.	Comp.	Meas.	Comp.	Measured range	Comp.	
27	6.6	6.8	22	22.6	[−15.2, −11.5]	−13.2	1.6
38	4.8	4.8	16	15.8	[−13.7, −10.9]	−13.1	2.0
70	6.9	6.1	22	20.0	[−15.7, −13.0]	−12.9	6.5
88	5.8	4.8	18	15.8	[−16.8, −13.3]	−12.8	4.5
107	4.6	6.1	21	20.0	[−19.7, −14.0]	−13.0	7.7
120	5.0	5.4	16	17.8	[−15.5, −10.3]	−13.0	6.8
150	4.1	4.3	13	14.2	[−18.2, −17.0]	−13.0	6.3
200	6.5	5.5	24	18.2	[−8.2, −5.4]	−14.2	5.0
250	5.4	4.5	23	14.8	[−27.0, −15.0]	−12.2	7.0
375	5.8	3.9	20	12.9	[−17.4, −14.5]	−13.6	7.3
710	5.3	4.5	—	14.9	—	−14.1	13.0

for which there is generally a loss in sensitivity on the acoustic axis. This affects, first, the target echo level through the incident signal level, i.e. transmission process; and, second, both target echo level and ambient-noise level through the reception process, but in equal proportions. Thus, it is convenient to incorporate the described loss due to transducer curvature (CL) directly in the expression for source level SL, hence:

$$SL=10\log P+DI_T-CL+170.8, \tag{8}$$

where P is the transmitted acoustic power in watts, and DI_T is the transmitting directivity index. The acoustic power is related to the nominal electrical power P_{el} by the basic expression:

$$P=\eta P_{el}, \tag{9}$$

where η is the conversion efficiency of the transducer, assumed to be 0.6 for the particular transducers. The transmitting directivity index is defined by the expression:

$$DI_T=10\log\frac{4\pi}{\int b\, d\Omega}, \tag{10}$$

where the integration of the transmit beam pattern b is performed over all 4π sr. Numerical integration has been employed to compute the integral in Equation (10) for both transducer types. Computed values for the baffled circular piston transducer of radius s agree well with values computed according to the ordinary narrow-beam approximation (Urick, 1983), namely $DI_T=20\log(ks)$. Nominal values of the several quantities in Equation (8) are presented in Table 3. Here the sea temperature is assumed to be 5°C, salinity 35, and depth 0 m, hence the sound speed is 1470.6 m/s (Mackenzie, 1981). Since the areas of cylindrical and circular piston transducers are equal, the acoustic power is common to both. It is observed that CL=0 for the circular piston transducer.

Transmission loss

For one-way propagation over the range r, this is $TL=20\log r+\alpha r$, where α is the absorption coefficient, given by Francois and Garrison (1982). For two-way propagation, the transmission loss is just double the one-way loss, or $2TL=40\log r+2\alpha r$. In determining the absorption coefficient, the temperature, salinity, and depth take the same values as in computation of the source level, respectively 5°C, 35, and 0 m, hence with sound speed 1470.6 m/s, and the pH is assumed to be

Table 3. Acoustic power P, transmitting directivity index DI_T in decibels, transducer curvature loss CL in decibels, and source level SL in decibels re 1 µPa at 1 m, for corresponding cylindrical and equal-area baffled circular piston transducers.

Frequency (kHz)	P (W)	Cylinder			Piston	
		DI_T	CL	SL	DI_T	SL
27	360	8.8	0.9	204.3	19.8	216.1
38	360	10.3	1.7	205.0	22.8	219.1
70	240	9.3	2.7	201.2	22.9	217.5
88	240	10.2	4.1	200.8	24.8	219.4
107	120	9.3	1.9	199.0	22.0	213.6
120	120	9.8	2.4	199.0	23.1	214.7
150	120	10.7	3.6	198.7	25.0	216.6
200	90	9.6	9.7	190.2	29.3	219.6
250	90	10.5	10.7	190.2	31.2	221.5
375	30	11.1	11.2	185.5	32.2	217.8
710	12	10.4	11.3	180.7	31.7	213.3

Table 4. Additional parameter values assumed in the performance computations, namely absorption coefficient α, equivalent beam angle Ψ in decibels, noise spectral level SPL in decibels re 1-Hz band, and noise band level NL in decibels.

Frequency (kHz)	α (dB/km)	Ψ (dB)		Sea state 0		Sea state 6	
		Cylinder	Piston	SPL	NL	SPL	NL
27	6.4	0.5	−12.1	22.8	57.2	47.0	81.3
38	10.7	1.0	−15.1	22.4	58.2	44.5	80.3
70	21.6	0.0	−15.2	25.3	63.7	40.1	78.6
88	26.1	1.0	−17.2	27.1	66.5	38.6	78.0
107	29.9	0.0	−14.4	28.7	69.0	37.5	77.8
120	32.2	0.5	−15.4	29.6	70.4	36.9	77.7
150	37.2	1.4	−17.4	31.5	73.3	36.2	77.9
200	45.6	0.3	21.6	34.0	77.0	36.2	79.2
250	55.1	−1.3	23.6	36.0	79.9	37.1	81.0
375	86.1	1.8	24.6	39.5	85.2	39.8	85.5
710	226.6	−1.2	24.1	45.0	93.5	45.0	93.6

7.7. Values of α used in the performance computations are shown in Table 4.

Echo level

The two mentioned cases are distinguished. For a single target, with target strength TS, the echo level is:

$$EL = SL - 2TL + TS. \quad (11)$$

For multiple targets distributed throughout the sampling volume V, with mean volume backscattering strength S_V:

$$EL = SL - 2TL + S_V + 10 \log V. \quad (12)$$

The sampling volume is assumed to take its nominal value:

$$V = \frac{c\tau}{2} r^2 \psi, \quad (13)$$

where c is the spread of sound, τ is the pulse duration, assumed to be 0.1 ms, and ψ is the equivalent beam angle:

$$\psi = \int b^2 d\Omega. \quad (14)$$

This has been computed by numerical integration for both transducer types. The results for the circular piston transducer agree closely with the simple narrow-beam approximation (Clay and Medwin, 1977), $\psi = 5.78/(ks)^2$, and a derived expression, $\Psi = 10 \log \psi = -DI_T + 7.6$. Values assumed for Ψ in the performance computations are presented in Table 4.

Noise level

The ambient noise is assumed to be isotropic and with a level due to three different sources. The Knudsen curves describe the noise spectral level SPL due to wave action. It is a function of transducer frequency f in Hertz and sea state number n_{ss} (Bartberger, 1965):

$$SPL_{amb} = 46 + 30 \log (n_{ss} + 1) - 17 \log (f/1000). \quad (15)$$

The noise spectral level for thermal noise is described by Mellen (1952):

$$SPL_{th} = -15 + 20 \log (f/1000). \quad (16)$$

It is reasonable to assume a receiver electronic noise level that is equivalent to the thermal noise level. If S denotes the corresponding antilogarithm, then the spectral noise level due to all three sources is:

$$SPL_{tot} = 10 \log (S_{amb} + 2S_{th}). \quad (17)$$

The noise band level NL is just:

$$NL = SPL + 10 \log BW, \quad (18)$$

where BW is the receiver bandwidth in hertz. In all of the present computations, the receiver bandwidth is assumed to be 10% of the transmit frequency, hence BW=0.1f. The noise spectral levels and noise band levels assumed in the computations are stated in Table 4.

Sonar equation

The several quantities are combined in the ordinary, active sonar equation, given ambient-noise-limited conditions. This is (Urick, 1983):

$$EL - (NL - DI_R) = DT, \quad (19)$$

where DI_R is the receiving directivity index, and DT is the detection threshold. Here, $DI_R = DI_T$. The detection threshold is assumed uniformly to be 20 dB. That is, the signal-to-noise ratio is chosen to be 20 dB, in order to ensure unambiguous signal detection. The single unknown in the sonar equation where EL is given by Equation (11), assuming a parametric value for TS, is

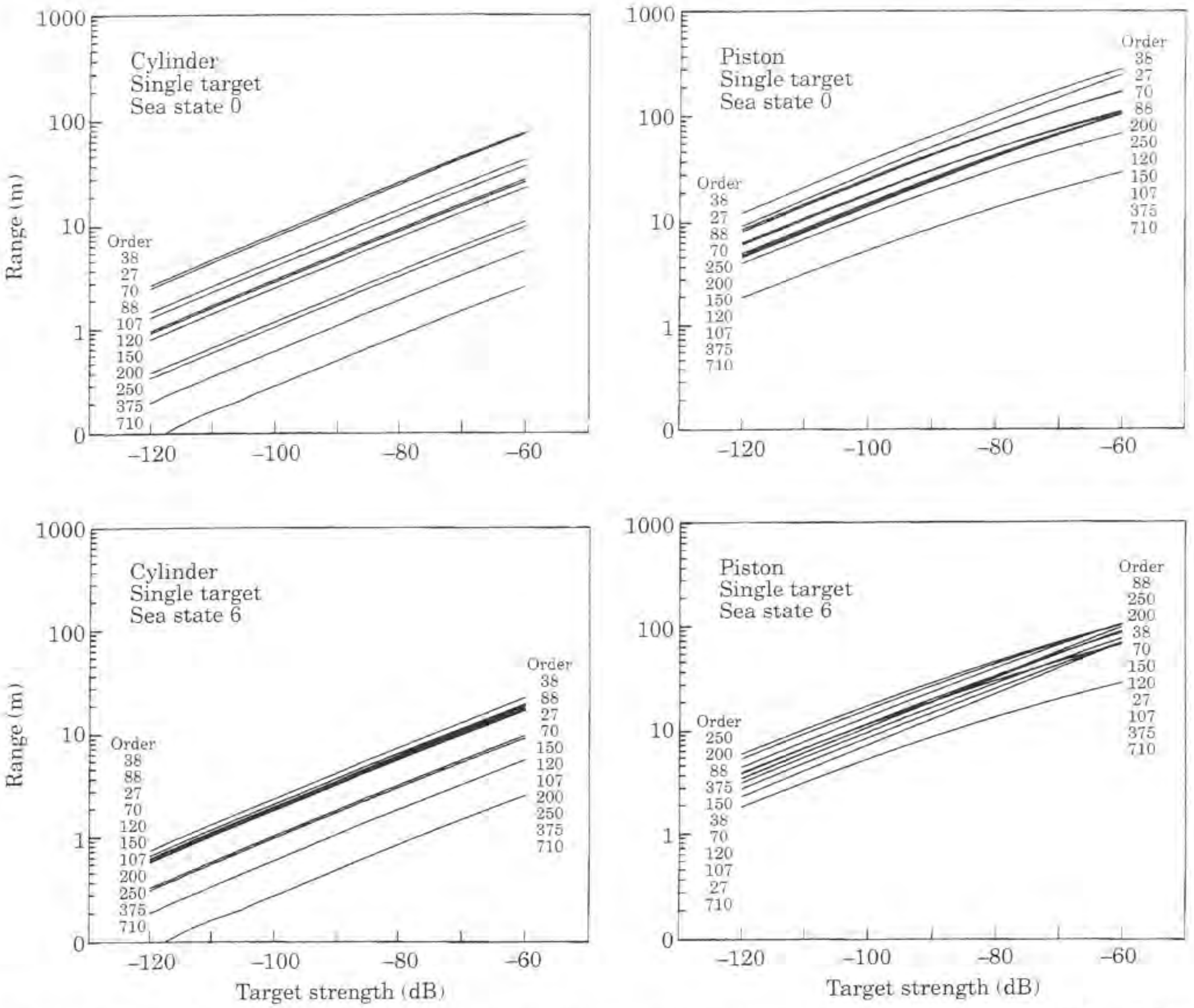

Figure 1. Maximum single-target detection range versus target strength for the transducer dimensions specified in Table 1, assuming ambient-noise-limited conditions and detection threshold of 20 dB. The 11 transducer frequencies are indicated with units of kilohertz.

the range r. This is the sought maximum range for single-target detection. The corresponding unknown in the sonar equation where EL is given by Equation (12), assuming a parametric value for S_V, is the maximum range for multiple-target detection.

Results and discussion

Results of the described performance computations are presented in both figures and tables. Figure 1 and Table 5 pertain to single targets according to Equations (11) and (19), and Figure 2 and Table 6, to multiple targets according to Equations (12) and (19). A range of values of target strength and mean volume backscattering strength are examined in Figures 1 and 2, respectively. Maximum detection ranges less than 0.1 m are not shown, but in fact ranges that are less than a certain distance, which is roughly equal to the square of the

Table 5. Maximum single-target detection range in metres for equal-area cylindrical and circular piston transducers, with dimensions in Table 1, assuming a target strength of −80 dB, ambient-noise-limited conditions, and detection threshold of 20 dB.

Frequency (kHz)	Sea state 0		Sea state 6	
	Cylinder	Piston	Cylinder	Piston
27	24.5	87.1	6.2	22.8
38	25.9	108.3	7.4	33.3
70	14.3	69.6	6.2	32.4
88	12.5	70.8	6.6	40.1
107	9.3	40.3	5.7	25.5
120	8.8	41.5	5.9	28.6
150	7.7	42.5	6.0	33.8
200	3.6	48.6	3.2	43.9
250	3.2	48.6	3.0	46.2
375	1.9	30.7	1.9	30.3
710	0.9	13.6	0.8	13.5

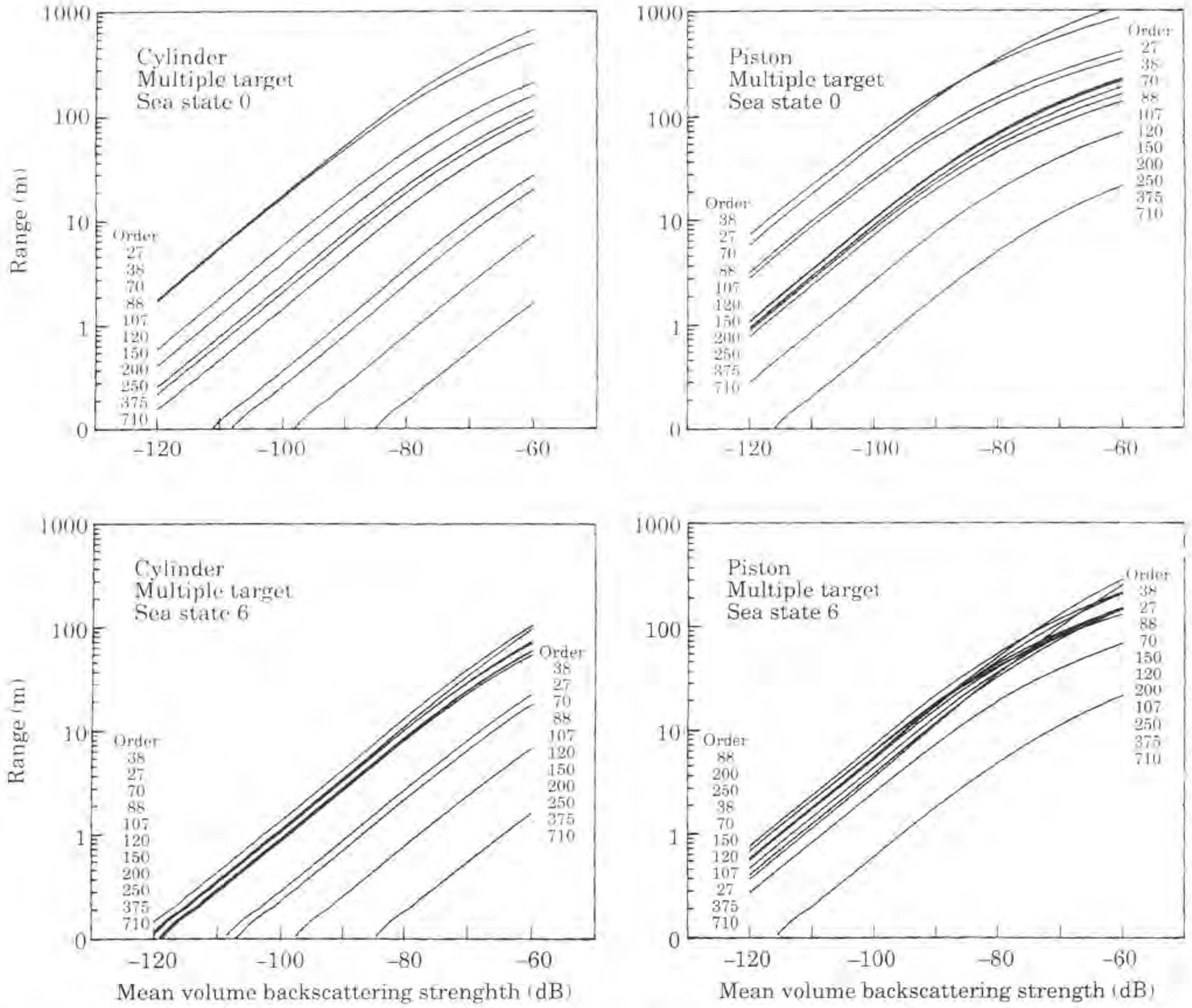

Figure 2. Maximum multiple-target detection range versus mean volume backscattering strength for the transducer dimensions specified in Table 1, assuming ambient-noise-limited conditions and detection threshold of 20 dB. The 11 transducer frequencies are indicated with units of kilohertz.

maximum transducer dimension divided by the acoustic wavelength, are uncertain for lying within the transducer nearfield.

In every single instance, the performance of the baffled planar circular piston transducer is superior to that of the respective equal-area cylindrical transducer. This is to be expected from two considerations: (1) The directivity index of the equal-area circular piston transducer is considerably greater than that of the corresponding cylindrical transducer. According to Table 3, the difference is in the approximate range 10–20 dB, but the directivity index appears twice in the ambient-noise-limited sonar equation: in the term for source level, as DI_T, and in the term for discrimination against isotropic ambient noise, as DI_R. (2) Because of the curvature of the cylindrical transducer, it suffers an on-axis loss in sensitivity to which the circular piston transducer is exempt. This is described

Table 6. Maximum multiple-target detection range in metres for equal-area cylindrical and circular piston transducers, with dimensions in Table 1, assuming a mean volume backscattering strength of −80 dB, ambient-noise-limited conditions, and detection threshold of 20 dB.

Frequency (kHz)	Sea State 0		Sea state 6	
	Cylinder	Piston	Cylinder	Piston
27	144.9	348.1	11.0	34.4
38	126.6	326.4	13.2	50.6
70	47.0	151.6	10.1	46.1
88	33.2	130.9	10.2	55.0
107	21.6	68.8	8.6	32.1
120	18.6	66.1	8.6	35.7
150	13.2	57.9	8.1	39.8
200	3.5	51.6	2.7	43.6
250	2.5	44.5	2.2	41.0
375	0.8	19.0	0.8	18.6
710	0.2	4.9	0.2	4.9

Table 7. Performance figure PF_1 for equal-area cylindrical and circular piston transducers, and acoustic intensity I on the transducer surface.

Frequency (kHz)	Sea state 0		Sea state 6		I (W/cm^2)
	Cylinder	Piston	Cylinder	Piston	
27	155.9	178.7	131.8	154.6	1.6
38	157.1	183.7	135.0	161.6	1.6
70	146.8	176.7	131.9	161.8	3.5
88	144.5	177.7	133.0	166.2	3.5
107	139.3	166.6	130.5	157.8	5.0
120	138.4	167.4	131.1	160.1	5.0
150	136.1	168.3	131.5	163.7	5.0
200	122.8	171.9	120.6	169.7	2.5
250	120.8	172.8	119.7	171.7	2.5
375	111.4	164.8	111.1	164.5	1.5
710	97.6	151.5	97.5	151.4	2.4

by the term CL in Equation (8), with numerical values in Table 3.

Computation of both the directivity index and the sensitivity loss for the cylindrical transducer, according to the present theoretical method, depends on the acoustic boundary condition. As observed in the Introduction, this is indeed problematical. However, by reference to the beam pattern measurements on the six fabricated cylindrical transducers, confidence is gained in the particular assumed boundary condition, the acoustic opacity described in the section on beam patterns. The respective values of beam pattern parameters in Table 2 support this use.

The directivity index and sensitivity loss factor may be combined in two useful measures of performance. The first, due to Urick (1983), is useful for characterizing transducer performance against single targets:

$$PF_1 = SL - (NL - DI_R). \tag{20}$$

The second measure, by simple extension, is useful for characterizing transducer performance against multiple targets distributed throughout the sampling volume:

$$PF_2 = SL + \Psi - (NL - DI_R). \tag{21}$$

The first measure is computed for each transducer type and each of the sea states in Table 7. Included in the table is the acoustic intensity I, derived by dividing the acoustic power in Table 3 by the respective total transducer area.

Reference to the cavitation threshold (Urick, 1983) indicates that this increases rapidly with frequency. The acoustic intensity for the cylindrical transducers shows the expected dependence up to about 150 kHz, although less than corresponding design values typically used by sonar manufacturers. At higher frequencies, the intensity is far less than the estimated average and far less than is ordinarily used in the design of planar, resonant transducers, for example, the circular piston transducer considered in this work. In general, such a transducer is mechanically more robust than a cylindrical transducer and can tolerate being driven at a higher electrical power level than is used with the cylindrical transducers above 150 kHz. Thus, for the circular piston transducers at these higher frequencies, the performance figures in Table 7 and the maximum detection ranges in Figures 1 and 2 and Tables 5 and 6 are underestimates.

Cylindrical transducers undoubtedly have application in underwater acoustics, including fisheries acoustics. A current example is in observation of food pellets in a fish-farming pen (Juell *et al.*, 1993). For measurement of dispersed or locally inhomogeneous aggregations of plankton and other weak scatterers, the conventional circular piston with equal area clearly gives superior performance.

There are pragmatic considerations too for choosing between different transducer types. Here, the circular piston transducer is also the better choice, for it is cheaper and easier to fabricate than is the corresponding equal-area cylindrical transducer. Inspection of the measured beam patterns in the transverse plane of the cylindrical transducers, describing the azimuthal dependence, are particularly revealing of practical difficulties in fabrication, for the range of variation with azimuth exceeds 3 dB for five of the six transducers, at nine of the 11 frequencies. In principle, it should be zero.

A further advantage of the circular piston transducer is standardization. Given the complexity of the general process of underwater acoustic mensuration, avoidance of special devices is a general rule, with particular force for multiple-frequency sondes.

Three matters not addressed here but deserving of future treatment are identified: (1) The precise range, number, and spacing of transducer frequencies require optimization for the scatterer species and sizes of interest. This naturally depends on the scattering properties of target organisms. (2) Given specification of a particular set of transducer frequencies, the radii of the transducers must be chosen apropos of their arrangement on a sonde. A major aim of this might be to ensure the greatest possible coincidence or overlap of sampling volumes. (3) Performance of the ultimately chosen set of transducers should be calculated on the basis of a generally closer approach to the cavitation limit than has been assumed at all frequencies in the present analysis. Clearly, performance will be enhanced under ambient-noise-limited conditions by driving transducers at higher power levels, consistent with avoiding cavitation and deleterious effects of heat production, especially at the highest frequencies, where absorption is a major cause of attenuation.

Acknowledgements

J. Dalen is thanked for sharing an engineering drawing of six cylindrical transducers configured as a sonde, together with the manufacturer's beam-pattern measurements of the same transducers. D. V. Holliday is thanked for communications on the transducer diffraction constant. H. Klaveness is thanked for a discussion on the cavitation limit of circular piston transducers, and H. Nes for a discussion on noise. T. Knutsen's interest in the comparative analysis and its documentation is gratefully acknowledged, as in Ø. Østensen's preparation of the figures.

References

Abramowitz, M. 1965. Struve functions and related functions. *In* Handbook of mathematical functions, pp. 495–502. Ed. by M. Abramowitz and I. A. Stegun. Dover, New York. 1046 pp.

Bartberger, C. L. 1965. Lecture notes on underwater acoustics. US Naval Air Development Center Report no. NADC-WR-6509. Johnsville, Pennsylvania. (Defense Documentation Center acquisition no. AD468869.) 415 pp.

Bobber, R. J. 1965. Diffraction constants of transducers. Journal of the Acoustical Society of America, 37: 591–595.

Born, M., and Wolf, E. 1970. Principles of optics. Fourth edition. Pergamon, Oxford. 808 pp.

Clay, C. S., and Medwin, H. 1977. Acoustical oceanography: principles and applications. J. Wiley & Sons, New York. 544 pp.

Francois, R. E., and Garrison, G. R. 1982. Sound absorption based on ocean measurements. Part II: Boric acid contribution and equation for total absorption. Journal of the Acoustical Society of America, 72: 1879–1890.

Henriquez, T. A. 1964. Diffraction constants of acoustic transducers. Journal of the Acoustical Society of America, 36: 267–269.

Ho, J.-M. 1993. Acoustic scattering by submerged elastic cylindrical shells: Uniform ray asymptotics. Journal of the Acoustical Society of America, 94: 2936–2946.

Ho, J.-M. 1994. Ray techniques in structural acoustics and vibration. *In* Proceedings of the Third International Congress on Air- and Structure-Borne Sound and Vibration, Montreal, 13–15 June 1994, pp. 293–300. Ed. by M. J. Crocker. International Scientific Publications, Auburn, Alabama.

Holliday, D. V., Pieper, R. E., and Kleppel, G. S. 1989. Determination of zooplankton size and distribution with multifrequency acoustic technology. Journal du Conseil International pour L'Exploration de la Mer, 46: 52–61.

Juell, J. E., Furevik, D. M., and Bjordal, A. 1993. Demand feeding in salmon farming by hydroacoustic food detection. Aquacultural Engineering, 12: 155–167.

Mackenzie, K. V. 1981. Nine-term equation for sound speed in the oceans. Journal of the Acoustical Society of America, 70: 807–812.

Mellen, R. H. 1952. The thermal-noise limit in the detection of underwater acoustic signals. Journal of the Acoustical Society of America, 24: 478–480.

Milosić, Z. 1993. Comments on "Diffraction constants of acoustic transducers" [Journal of the Acoustical Society of America 36, 267–269 (1964)]. Journal of the Acoustical Society of America, 93: 1202.

Morse, P. M. 1948. Vibration and sound. Second edition. McGraw-Hill, New York. 468 pp. (Reprinted by the American Institute of Physics, 1976.)

Neubauer, W. G. 1963. A summation formula for use in determining the reflection from irregular bodies. Journal of the Acoustical Society of America, 35: 279–285.

Urick, R. J. 1983. Principles of underwater sound. Third edition. McGraw-Hill, New York. 423 pp.

ICES Journal of Marine Science, 56: 606–612, 1999
Article No. jmsc.1999.0479, available online at http://www.idealibrary.com on IDEAL

Extinction cross-section of Norwegian spring-spawning herring

K. G. Foote

Foote, K. G. 1999. Extinction cross-section of Norwegian spring-spawning herring. ICES Journal of Marine Science, 56: 606–612.

Acoustic abundance estimation of dense, vertically extended aggregations of fish requires knowledge of the extinction cross-section. An established method based on a comparison of the area backscattering coefficients of fish and underlying flat bottom has been exercised for herring in Ofotfjorden in January 1994, but for the first time with the powerful combination of the SIMRAD EK500 scientific echosounder and Bergen echo integrator. This has enabled the flatness of the bottom to be controlled to within a single meter over 0.1-nautical-mile (nmi) intervals of echo integration. This control enhances the quality of the new data over those collected in three previous years. The estimate for the ratio of the extinction cross-section to the backscattering cross-section is accordingly revised. The new value for the ratio is 2.41, with standard deviation of 0.33. This has been used in acoustic abundance surveys of herring since winter 1993–1994. The variability in measurement results remains an object of investigation. This is viewed in the light of the optical literature, which suggests that the extinction cross-section of finite but complicated physical scatterers may be as sensitive to details of orientation as is the backscattering cross-section. The possibility of exploiting this property is considered.

Key words: herring, acoustic abundance estimation, extinction cross-section.

Received 9 January 1997; accepted 5 April 1999.

K. G. Foote: Institute of Marine Research, PO Box 1870 Nordnes, N-5817 Bergen, Norway (Current: Department of Applied Ocean Physics and Engineering, Woods Hole Oceanographic Institution, Woods Hole, Massachusetts 02543, USA. Tel.: +1 508 289 2445; Fax: +1 508 457 2194).

Introduction

Norwegian spring-spawning herring (*Clupea harengus*) has been wintering in the fjords of northern Norway since the winter of 1987–1988. It has been acoustically surveyed during the wintering period on a regular basis since 1992 (Foote, 1993; Røttingen *et al.*, 1994; Foote and Røttingen, 1995; Foote *et al.*, 1996, 1997). A concomitant of the wintering of such a large stock in a fjord system is a generally dense concentration. As measured acoustically, the area backscattering coefficient s_A (Knudsen, 1990; Foote and Knudsen, 1994) is often of the order of 100 000 square metres of backscattering cross-section per square nautical mile (nmi), if not much more.

Such values of s_A are characteristic of high numerical densities and large vertical extensions. They are also indicative of significant effects of acoustic extinction, by which the energy in the echo suffers an additional attenuation beyond that of spherical spreading and ordinary medium absorption. Insofar as the ordinary theory of echo integration presumes a linear relationship between the area backscattering coefficient and numerical density of fish, an underestimate in fish density can result from neglect of extinction. Certainly an attempt has been made to correct acoustic measurements of herring density during the annual winter surveys. This has been done through an algorithm (Foote, 1990), which requires knowledge of a technical parameter called the extinction cross-section.

This parameter has been described earlier for herring (Foote *et al.*, 1992), but under certain limitations that have since been overcome. Before presenting the adapted methods and new measurements, however, the nature of the extinction cross-section, methods to determine this, and the particular application to wintering herring are considered in a brief review.

Brief review of methods to determine the extinction cross-section

The extinction cross-section is a measure of the effect of an individual finite scatterer on taking energy out of the forward propagating direction of a wave (Born and

1054–3139/99/050606+07 $30.00/0

Wolf, 1970). It is thus the sum of scattering and absorption cross-sections, also called the total cross-section (Morse and Ingard, 1968).

There are a number of ways in which the extinction cross-section of fish can be determined. For example, if sufficient information is available about the scattering properties of a single fish, then the component cross-sections could be determined and summed. Alternatively, the extinction cross-section could be calculated by means of the forward-scattering theorem (Bowman *et al.*, 1969; Born and Wolf, 1970). The required information could take the form of a set of empirical observations of scattering as a function of orientation, frequency, depth, and other critical parameters. The information could also take the form of a set of morphometric data, as of the swimbladder shape, and a model for the variation in shape with depth. Given information about the orientation and depth distributions of the object fish, either kind of scattering information could be used in the determination. It is regrettable that most of the mentioned data do not exist for herring, although some of these are being sought in ongoing investigations.

The extinction cross-section could also be determined through backscattering measurements of encaged fish aggregations and tethered individual fish, when linked by a scattering model. An illustrative example is provided by an analysis (Foote, 1978) of the experiment by Røttingen (1976). The examined species was saithe (*Pollachius virens*), a gadoid and physoclist, with closed swimbladder. This is in contrast to herring, a clupeoid and phyostome, with open swimbladder. A refined method of analysis (Foote, 1983) may be useful for determining the extinction cross-section under other conditions of encaged fish measurement.

Were it possible to observe the forward-scattered wave directly, the extinction cross-section could be determined. This would necessarily involve two transducers, one functioning as a source, the other as a receiver. Under rather controlled conditions, as with stationary source and receiver, the necessary fine alignment of typically directional transducers might be achieved. If one or both of the transducers were more or less omnidirectional, as in the case of certain hydrophones, then the need for alignment could be relaxed, but at the cost of having to work at rather short ranges. Measurements done in fish pens (Ishii *et al.*, 1983; Furusawa *et al.*, 1984, 1992), for example, are illustrative in this regard. They are quite variable because of statistical fluctuations in numerical density and interference effects. In any case, application of the method to wintering herring being registered with a transducer mounted on a moving survey vessel is evidently remote.

In a variant of the foregoing method, the lower hydrophone is replaced by a reference target and the upper hydrophone, by a transducer (MacLennan *et al.*, 1990). The forward scattered wave is sensed indirectly through backscattering. A standard metal sphere has been used in caged-fish measurements. As in the case of the two-hydrophone measurements on penned fish (Furusawa *et al.*, 1992), there is a high degree of variability in the measurements.

It is to be emphasized that the application of interest is acoustic abundance surveying of Norwegian spring-spawning herring in the wintering state by means of a transducer mounted on the hull or retractable keel of a research vessel steaming at 10 knots. As fish behaviour is generally influenced by vessel speed, state of fish including physiological condition and depth (Ona, 1990), and environmental factors such as lighting and bottom depth, an *in situ* measurement performed under surveying conditions must be the desideratum.

In fact, a measurement of this kind was accomplished during experiments performed in 1988, 1990, and 1991 owing to an extraordinary circumstance: the occurrence of fish over an exceptionally flat seafloor (Foote *et al.*, 1992). That the seafloor, or bottom, can serve as a reference target had already been noted by MacLennan *et al.* (1990) and Toresen (1991). If the bottom scattering properties are sufficiently uniform over a substantial area, then the bottom echo statistics may be favourable for the measurement. At the time of the original data collections, the possibilities for bottom depth measurement were quite limited. These have since been remedied in dramatic fashion by the combination of the SIMRAD EK500 scientific echosounder (Bodholt *et al.*, 1989) and Bergen echo integrator (Foote *et al.*, 1991). Details on the adapted methods and new measurements are now presented.

Theory of measurement and method of calculation

Measurement of the extinction cross-section is based on a comparison of echo energy due to a fish layer with that due to the underlying flat bottom. The echo energy is the time-integral of the received signal intensity after application of "20 log r+2αr" time-varied gain in order to correct for ordinary propagation losses assuming scattering by a layer or planar surface. The described echo energy is thus proportional to the area backscattering coefficient, the standard measure of acoustic area density used in modern echo integrators (Bodholt *et al.*, 1989; Knudsen, 1990).

According to Foote *et al.* (1992), the respective area backscattering coefficients are linearly related to each other. Denoting the coefficient associated with the fish layer by $s_{A,F}$ and that associated with the bottom by $s_{A,B}$:

$$s_{A,B}=as_{A,F}+b. \tag{1}$$

In the absence of fish, $s_{A,B}$ assumes its maximal value. In the presence of fish, $s_{A,B}$ is generally diminished by extinction of sound energy passing through the fish layer both in transit to the bottom and in transit back to the transducer after reflection or scattering from the bottom.

As the bottom is generally not a uniform target, either in flatness or in scattering properties, and because its echo is generally very substantial, especially compared to that from fish, it requires unusual conditions for the particular method to succeed. These occur at times, however, for the spawning stock of Norwegian spring-spawning herring when wintering in Ofotfjorden. The outer part of Ofotfjorden, at about 68°24′N and 16°10′–16°40′E is exceptionally flat, and dense, extended concentrations of herring occasionally appear over this area in a distinct midwater scattering layer.

Inhomogeneities both in the density of fish concentrations and scattering properties of flat bottom require a number of simultaneous measurements of $s_{A,B}$ and $s_{A,F}$ and use of linear regression analysis to extract the significant dependences in Equation (1). If this is treated as a regression equation, then the estimated regression coefficients $\hat{a}$ and $\hat{b}$ determine the extinction cross-section σ_e, here expressed relative to the fish backscattering cross-section σ_b:

$$\sigma_e/\sigma_b = -1852^2\hat{a}/(2\hat{b}). \tag{2}$$

To express the confidence limits, Equation (1) is transformed by substituting y for $s_{A,B}$ and x for $s_{A,F}$. Thus, y=ax+b, or, with respect to the n individual paired measurements (x_i, y_i):

$$y_i = \hat{a}x_i + \hat{b} + \varepsilon_i, \tag{3}$$

where ε_i is the error term, which is minimized in a least-squares sense by performance of the linear regression analysis. The confidence limits of σ_e/σ_b are:

$$\frac{1852^2}{2}[(\bar{x}-d_1)^{-1}, (\bar{x}-d_2)^{-1}], \tag{4}$$

where $\bar{x}$ is the mean value of x, and d_1 and d_2 are the respective lesser and greater solutions of the quadratic equation (Seber, 1977):

$$d^2[\hat{a}^2 - s_e^2 F^{\alpha}_{1,n-2}/\sum_i (x_i-\bar{x})^2] - 2d\bar{y}\hat{a} + (\bar{y}^2 - s_e^2 F^{\alpha}_{1,n-2}/n) = 0 \tag{5}$$

where s_e^2 is the squared standard error of regression, $\bar{y}$ is the mean value of y, and $F^{\alpha}_{1,n-2}$ is the F-statistic at significance level α with degrees of freedom 1 and $n-2$. The statistic is widely available in tabulated form, for example, in Hald (1952) and Zelen and Severo (1965), although not always identified by the same name.

The extinction cross-section is expressed in relative terms in Equation (2). Its absolute value is derived by substituting for the backscattering cross-section σ_b. For Norwegian spring-spawning herring, this is given by the equation (Foote, 1987):

$$TS = 10\log\frac{\sigma_b}{4\pi r_o^2} = 20\log \ell - 71.9, \tag{6}$$

where r_o is the reference distance of 1 m, and ℓ is the root-mean-square fish length in centimetres. Thus, in units of square centimetres, σ_e is derived by multiplying the ratio σ_e/σ_b in Equation (2) by the constant factor $4\pi 10^{-3.19}\ell^2$.

Experimental methods

The measurements were made with the SIMRAD EK500 echosounder (Bodholt *et al.*, 1989) and Bergen echo integrator (Foote *et al.*, 1991) during the cruise with RV "Johan Hjort" 6–17 January 1994. The purpose of the cruise was abundance assessment of that part of the herring stock that winters in the Ofotfjorden-Tysfjorden system. At times, a dense, thick concentration of herring appeared midwater over the depth range 200–400 m in outer Ofotfjorden, where the bottom is quite if not exceptionally flat. In addition to measurements made during ordinary conduct of the survey, special measurements were made to determine the extinction cross-section. The periods of these are summarized in Table 1.

During the described period of measurements, the amount of daylight increased steadily, although the sun does not rise for the first time in the year until 15 January. The total period of nautical twilight is approximately 0900–1500.

Measurements were made simultaneously at each of four frequencies, 18, 38, 120, and 200 kHz. Only the measurements at 38 kHz are reported here. The SIMRAD ES38B split-beam transducer was used strictly as a single-beam device for purposes of echo integration. The pulse duration was 1 ms and receiver bandwidth, 3.8 kHz. The pulse repetition frequency was about $1\ s^{-1}$. The vessel speed was about 7–8 knots, the same as during execution of the acoustic survey.

The echosounder and echo integrator were calibrated by the standard-target method recommended by ICES (Foote *et al.*, 1987). The target at 38 kHz was the 60-mm-diameter copper sphere.

Data were stored ping by ping. During postprocessing, results of integration of the fish-layer and bottom echoes were stored with the highest standard resolution, namely 0.1-nmi. Data on the depth of the detected bottom were also condensed. For each 0.1-nmi integration interval, the average depth and extrema were stored, three values in all, allowing criteria on depth and depth stability to be imposed in selecting subsets of data for analysis. Some statistics of the bottom depth for the various measurement series are shown in Table 1.

Table 1. Periods of data collection for the extinction cross-section, including number n of 0.1-nmi intervals over which the depth changes by no more than 1 m. The total depth range [z_{min}, z_{max}], average depth z_{ave}, and standard deviation Δz are also given

Series no.	Start		End		Ship's log interval (nmi)	n	Depths (m)			
	Date	UTC	Date	UTC			z_{min}	z_{max}	z_{ave}	Δz
1	0109	0748	0109	1740	0281.0–0337.5	295	517	540	530	5
2	0111	0852	0111	1023	0561.6–0575.7	70	524	543	536	7
3	0112	0823	0112	1536	0740.0–0785.0	293	530	545	540	3
4	0114	0017	0114	1403	0935.7–0998.3	300	529	546	541	3
5	0115	1600	0115	1733	1210.8–1223.3	42	530	544	538	5
6	0116	0428	0116	0717	1305.3–1324.0	75	520	545	533	7
7	0116	1220	0116	1448	1370.2–1385.1	8	539	570	550	10

Acoustic data were supplemented by biological data derived from catching operations. Data from a total of 12 fish capture stations in outer Ofotfjorden are available for the period 5–15 January 1994. Results from these stations are expressed in Table 2 in terms of the mean length $\bar{\ell}$ and standard deviation $\Delta\ell$ of sampled distributions of total fish length ℓ. The overall measures of total length are formed by weighting the station data equally: $\bar{\ell}=33.9$, $\overline{\ell^2}^{1/2}=34.0$, and $\ell_{rms}=3.2$ cm.

Results

The described linear regression analysis was performed for each of the seven data series for each of four different criteria on depth stability. These are that the total variation in depth dz during any one 0.1-nmi interval not exceed 0, 1, 2, or 5 m. Corresponding results are shown in Table 3 for the first six data series. Results for the seventh series are omitted because of insufficient data.

Discussion

The method of data collection, with storage of individual echo time series through values of the volume backscattering strength together with value of detected bottom depth, has made possible a finer-grained analysis than was possible during previous determinations of the extinction cross-section of herring in Ofotfjorden (Foote *et al.*, 1992). Thus it has been possible to separate the data by degree of variation in depth over the basic interval of echo integration, 0.1 nmi for the present data. The increased power of discrimination has also increased the complexity of analysis. This is reflected in Table 3, where values of the ratio σ_e/σ_b are observed to vary for the same data series simply due to changing the requirement on bottom depth stability through the parameter dz.

Maintaining dz at a low value presumably ensures a greater flatness, hence homogeneity too, of scattering from the bottom. A standard reference target, but one that is distributed over the beam cross-section at about 500-m range, is what is sought. The penalty for requiring dz to be small is a reduced number of data.

Here the trade-off between the requirement of flatness over 0.1-nmi intervals of sailed distance and numbers of data is resolved by choosing dz=1 m. This corresponds to a bottom slope no greater than one part in 185. Further requirement that there be at least 100 intervals in each data set restricts the results in Table 3 to just three, for series numbers 1, 3, and 4. These results are presented again in Table 4, with results from the previous investigations.

As before, the range of values for the ratio is apparently uncomfortably high. Nonetheless, in the context of the values from 1988–1991, the new data are consistent. It seems reasonable to average the three new values for application in correcting the echo integration data for extinction. The results of this averaging are the following: Ave(σ_e/σ_b)=2.41, s.d.(σ_e/σ_b)=0.33, and σ_e=22.7 cm^2.

Certainly the question may be raised as to whether the earlier data should also be averaged in forming a best estimate of the ratio of extinction and backscattering cross-sections. At present, one obstacle to this is the lack of depth data with resolution comparable to that described in Tables 1 and 3 for the 1994 measurements. A second obstacle that applies to three of the four cases is the substantially smaller number of basis data. In the fourth case, that for 1990 daytime, n_s=324 and the value of σ_e/σ_b of 2.28 reduces the average ratio by just 0.03. This is well within the confidence limit of 0.33 for the three 1994 values.

Attempts to explain the variation in values for σ_e/σ_b by day/night effects have failed. There is simply insufficient evidence for such effects. This could reflect the difficulty of making a measurement that requires a large quantity of fish to appear over a flat bottom at the precise time available for investigation.

It might be speculated that the size distribution of fish changed in the course of the three measurement series reported in Table 4. Reference to the biological data

Table 2. Fish capture stations performed in outer Ofotfjorden during the period 5–15 January 1994, excepting possibly the first with unconfirmed date, with following statistics of distribution of total fish length: mean $\bar{\ell}$, root-mean-square ℓ_{rms}, and standard deviation $\Delta\ell$. The sample size is denoted n_s.

Vessel	Date	n_s	$\bar{\ell}$ (cm)	ℓ_{rms} (cm)	$\Delta\ell$ (cm)
"Inger Hildur"	[0105]	100	33.7	33.8	2.8
"Inger Hildur"	0105	100	33.9	34.0	2.5
"Frantzen Jr"	0106	155	34.2	34.4	3.1
"Inger Hildur"	0107	100	33.5	33.6	2.6
RV "Johan Hjort"	0109	100	35.1	35.2	3.0
"Frantzen Jr"	0111	100	34.1	34.2	2.6
"Inger Hildur"	0112	100	33.7	33.8	2.7
RV "Johan Hjort"	0114	100	34.1	34.3	3.8
RV "Johan Hjort"	0114	100	33.7	33.9	3.7
"Inger Hildur"	0114	100	33.3	33.4	3.0
"Inger Hildur"	0114	100	31.3	31.5	3.2
RV "Johan Hjort"	0115	100	36.1	36.2	2.6

Table 3. Results of the linear regression analysis for σ_e/σ_b and lower and upper bounds with 95% confidence. The parameter dz indicates the maximum allowable variations in depth over individual 0.1-nmi intervals of sailed distance, and n_s is the number of such intervals.

Series no.	dz (m)	n_s	σ_e/σ_b	$(\sigma_e/\sigma_b)_-$	$(\sigma_e/\sigma_b)_+$	σ_e (cm^2)
1	0	142	2.78	2.47	3.07	26.1
1	1	295	2.56	2.30	2.82	24.1
1	2	315	2.57	2.31	2.82	24.1
1	5	330	2.59	2.33	2.85	24.4
2	0	39	3.15	1.07	5.05	29.6
2	1	70	3.07	1.28	4.75	28.9
2	2	75	2.97	1.18	4.64	27.9
2	5	84	2.83	1.49	4.10	26.6
3	0	183	1.97	1.79	2.15	18.5
3	1	293	2.02	1.87	2.16	18.9
3	2	303	2.03	1.90	2.17	19.1
3	5	322	2.05	1.92	2.17	19.2
4	0	207	2.48	2.00	2.94	23.4
4	1	300	2.65	2.17	3.11	24.9
4	2	314	2.82	2.33	3.29	26.5
4	5	326	2.96	2.44	3.45	27.8
5	0	21	3.52	2.98	4.04	33.1
5	1	42	3.26	2.88	3.63	30.7
5	2	46	3.71	3.10	4.28	34.9
5	5	47	3.53	2.90	4.13	33.2
6	0	32	3.39	1.95	4.68	31.8
6	1	75	3.06	2.29	3.78	28.7
6	2	82	3.50	2.86	4.11	32.9
6	5	92	2.62	1.67	3.49	24.6

contradicts this, however, for there seems to have been no significant change in the length distribution over the duration of the measurements, 9–14 January 1994, described in Table 1.

Natural variation in the scattering properties of the bottom could also introduce a source of variability in the results. Thus far, there is no particular evidence for a strong variation in properties, if only because of the empirical finding of a more or less consistent relationship between the area backscattering coefficients of bottom and fish. Whatever variation there has been in purely bottom backscattering has not been sufficiently large to obscure the dependence of the bottom echo on the overlying layer of fish. In addition, the method of determination of the extinction cross-section is relative, which further lessens the influence on natural variations in bottom echoes. Recently, during a cruise with RV "Johan Hjort" to Ofotfjorden in December 1998, three bottom samples were taken from the area by means of a grab. While these await fine-grained analysis, they

Table 4. Summary of new data compared with earlier measurements of σ_e/σ_b. The category of day/night (D/N) for the 1994 data is that of the preponderance. Units of $\bar{b}$ and s_e are those of s_A multipled by 10^6. The bounds of the ratio σ_e/σ_b apply with 95% confidence. The associated mean lengths for 1988, 1990, and 1991 are 30.9, 32.9, and 34.3 cm, with the same standard error of the mean of 0.1 cm.

Year	D/N	$\bar{a}$	$\bar{b}$	s_e	n_e	σ_e/σ_b	Ratio bounds Lower	Ratio bounds Upper	σ_b (cm^2)	σ_e (cm^2)
1988	D	1.01	1.06	0.144	45	1.64	0.97	2.24	7.7	12.7
1990	D	1.55	1.16	0.191	324	2.28	2.10	2.46	8.8	20.0
1991	D	1.30	1.92	0.204	120	1.17	1.06	1.26	9.5	11.2
1991	N	2.32	1.78	0.169	140	2.24	2.10	2.37	9.5	21.4
1994	$\underline{D}$+N	2.67	1.78	0.378	295	2.56	2.30	2.82	9.4	24.1
1994	D	1.90	1.62	0.243	293	2.02	1.87	2.16	9.4	18.9
1994	D+$\underline{N}$	3.06	1.98	0.674	300	2.65	2.17	3.11	9.4	24.9

appear to consist of the same gray clay. The grab stations span a total distance of 9.9 nmi.

It is possible that the behaviour of the fish changed. The fact that the fish were observed to begin their outwards migration from Ofotfjorden and Tysfjorden during the cruise makes this more plausible.

Two mechanisms for the effect of behaviour on the extinction cross-section are those of orientation and swimbladder state. Data on these are lacking. The depth range of fish varied slightly, as the fish remained at depths greater than 200 m at all times.

If the orientation distribution were to change, the effect on echo energy would be immediate (Foote, 1980; Furusawa, 1988). Presumably the extinction cross-section would also change. The optics literature may offer particular insight here, for extinction is studied and measured to a much greater degree than in underwater sound. Use of lidar, the light-analogue of sonar, as a quantitative instrument, is especially sensitive to extinction relative to backscattering (Hooper, 1993), notwithstanding the exception of Raman lidar (Ansmann *et al.*, 1990). The sensitive effect of particle orientation on extinction in addition to backscattering is recognized (Bohren and Huffman, 1983). Frequency-dependent scattering effects, for both spherical and non-spherical scatterers, are also well recognized (McCartney, 1976; Ulaby *et al.*, 1981).

Interest in the optics literature in the dual subjects of backscattering and extinction is current for a number of reasons. Use of lidar has already been mentioned. A second major reason is found in the importance of albedo and absorption due to aerosols on the Earth radiation budget (Lovelock and Kump, 1994; Taylor and Penner, 1994), for which calculations have been performed for over 20 years (Charlson *et al.*, 1987).

Multiple-frequency measurements in acoustics may be expected to give insight into the connection of extinction and backscattering cross-sections, as through inference of the orientation distribution. It requires a scattering model for the fish, however, and for the physostomous herring this is still lacking.

Acknowledgements

Fellow participants on the cruise when the new data were collected are thanked for their several contributions. K. A. Hansen is particularly thanked for interpreting the echosounder data and ensuring their systematic integration. I. Røttingen's assembly of the fish capture data is gratefully acknowledged. R. Skeide's organization of the grab stations on the cruise in December 1998 is appreciated. The EU is thanked for partial support through RTD—contract no. AIR2-CT94-1007.

References

Ansmann, A., Riebesell, M., and Weitkamp, C. 1990. Measurement of atmospheric aerosol extinction profiles with a Raman lidar. Optics Letters, 15: 746–748.

Bodholt, H., Nes, H., and Solli, H. 1989. A new echo-sounder system. Proceedings of the Institute of Acoustics, 11(3): 123–130.

Bohren, C. F., and Huffman, D. R. 1983. Absorption and scattering of light by small particles. Wiley, New York. 530 pp.

Born, M., and Wolf, E. 1970. Principles of optics. Fourth edition. Pergamon Press, Oxford. 808 pp.

Bowman, J. J., Senior, T. B. A., and Uslenghi, P. L. E. (eds) 1969. Electromagnetic and acoustic scattering by simple shapes. North Holland, Amsterdam. 728 pp.

Charlson, R. J., Lovelock, J. E., Andreae, M. O., and Warren, S. G. 1987. Oceanic phytoplankton, atmospheric sulphur, cloud albedo and climate. Nature, 326: 655–661.

Foote, K. G. 1978. Analysis of empirical observations on the scattering of sound by encaged aggregations of fish. Fiskeridirektoratets Skrifter, Serie Havundersøkelser, 16: 423–456.

Foote, K. G. 1980. Effect of fish behaviour on echo energy: the need for measurements of orientation distributions. Journal du Conseil international pour l'Exploration de la Mer, 39: 193–201.

Foote, K. G. 1983. Linearity of fisheries acoustics, with addition theorems. Journal of the Acoustical Society of America, 73: 1932–1940.

Foote, K. G. 1987. Fish target strengths for use in echo integrator surveys. Journal of the Acoustical Society of America, 82: 981–987.

Foote, K. G. 1990. Correcting acoustic measurements of scatterer density for extinction. Journal of the Acoustical Society of America, 88: 1543–1546.

Foote, K. G. 1993. Abundance estimation of herring hibernating in a fjord. ICES CM 1993/D:45. 12 pp.

Foote, K. G., and Knudsen, H. P. 1994. Physical measurement with modern echo integrators. Journal of the Acoustical Society of Japan (E), 15: 393–395.

Foote, K. G., and Røttingen, I. 1995. Acoustic assessment of Norwegian spring spawning herring in the wintering area, December 1994 and January 1995. ICES CM 1995/H:9. 22 pp.

Foote, K. G., Knudsen, H. P., Vestnes, G., MacLennan, D. N., and Simmonds, E. J. 1987. Calibration of acoustic instruments for fish density estimation: a practical guide. ICES Cooperative Research Report, 144. 69 pp.

Foote, K. G., Knudsen, H. P., Korneliussen, R. J., Nordbø, P. E., and Røang, K. 1991. Postprocessing system for echo sounder data. Journal of the Acoustical Society of America, 90: 37–47.

Foote, K. G., Ona, E., and Toresen, R. 1992. Determining the extinction cross section of aggregating fish. Journal of the Acoustical Society of America, 91: 1983–1989.

Foote, K. G., Ostrowski, M., Røttingen, I., Engås, A., Hansen, K. A., Hauge, K. H., Skeide, R., Slotte, A., and Torgersen, Ø. 1996. Acoustic abundance estimation of the stock of Norwegian spring spawning herring, winter 1995–1996. ICES CM 1996/H:33. 13 pp.+6 tables+13 figs.

Foote, K. G., Ostrowski, M., Røttingen, I., and Slotte, A. 1997. Abundance estimation of Norwegian spring spawning herring wintering in the Vestfjord system, December 1996. ICES CM 1997/FF:13. 8 pp.+4 tables+10 figs.

Furusawa, M. 1988. Prolate spheroidal models for predicting general trends of fish target strength. Journal of the Acoustical Society of Japan (E), 9: 13–24.

Furusawa, M., Ishii, K., Miyanohana, Y., and Maniwa, Y. 1984. Experimental investigation of an acoustic method to estimate fish abundance using culture nets. Japanese Journal of Applied Physics, 23: 101–103.

Furusawa, M., Ishii, K., and Miyanohana, Y. 1992. Attenuation of sound by schooling fish. Journal of the Acoustical Society of America, 92: 987–994.

Hald, A. 1952. Statistical tables and formulas. Wiley, New York. 97 pp.

Hooper, W. P. 1993. Aureole lidar: instrument design, data analysis, and comparison with aircraft spectrometer measurements. Applied Optics, 32: 4019–4027.

Ishii, K., Furusawa, M., and Miyanohana, Y. 1983. Measurements of attenuation of sound by schooling fish. Technical Report of the National Research Institute of Fisheries Engineering and Fishing Boat Instrumentation, 4: 73–94.

Knudsen, H. P. 1990. The Bergen Echo Integrator: an introduction. Journal du Conseil international pour l'Exploration de la Mer, 47: 167–174.

Lovelock, J. E., and Kump, L. R. 1994. Failure of climate regulation in a geophysical model. Nature, 369: 732–734.

MacLennan, D. N., Armstrong, F., and Simmonds, E. J. 1990. Further observations on the attenuation of sound by aggregations of fish. Proceedings of the Institute of Acoustics, 12(1): 99–106.

McCartney, E. J. 1976. Optics of the atmosphere: scattering by molecules and particles. Wiley, New York. 408 pp.

Morse, P. M., and Ingard, K. U. 1968. Theoretical acoustics. Princeton University Press, Princeton, New Jersey. 927 pp.

Ona, E. 1990. Physiological factors causing natural variations in acoustic target strength of fish. Journal of the Marine Biological Association of the United Kingdom, 70: 107–127.

Røttingen, I. 1976. On the relation between echo intensity and fish density. Fiskeridirektoratets Skrifter, Serie Havundersøkelser, 16: 301–314.

Røttingen, I., Foote, K. G., Huse, I., and Ona, E. 1994. Acoustic abundance estimation of wintering Norwegian spring spawning herring, with emphasis on methodological aspects. ICES CM 1994/(B+D+G+H):1. 17 pp.

Seber, G. A. F. 1977. Linear regression analysis. Wiley, New York. 465 pp.

Taylor, K. E., and Penner, J. E. 1994. Response of the climate system to atmospheric aerosols and greenhouse gases. Nature, 369: 734–737.

Toresen, R. 1991. Absorption of acoustic energy in dense herring schools studied by the attenuation in the bottom echo signal. Fisheries Research, 10: 317–327.

Ulaby, F. T., Moore, R. K., and Fung, A. K. 1981. Microwave remote sensing: active and passive. Vol. 1: Microwave remote sensing fundamentals and radiometry. Addison-Wesley, Reading, Massachusetts.

Zelen, M., and Severo, N. C. 1965. Probability functions. *In* Handbook of Mathematical Functions, pp. 925–995. Ed. by M. Abramowitz, and I. A. Stegun. Dover, New York.

Depth-dependent target strengths of gadoids by the boundary-element method

David T. I. Francis
Department of Electronic, Electrical and Computer Engineering, University of Birmingham, Edgbaston, Birmingham B15 2TT, United Kingdom

Kenneth G. Foote[a)]
Woods Hole Oceanographic Institution, Woods Hole, Massachusetts 02543

(Received 5 October 2002; revised 24 July 2003; accepted 25 August 2003)

The depth dependence of fish target strength has mostly eluded experimental investigation because of the need to distinguish it from depth-dependent behavioral effects, which may change the orientation distribution. The boundary-element method (BEM) offers an avenue of approach. Based on detailed morphometric data on 15 gadoid swimbladders, the BEM has been exercised to determine how the orientation dependence of target strength changes with pressure under the assumption that the fish swimbladder remains constant in shape and volume. The backscattering cross section has been computed at a nominal frequency of 38 kHz as a function of orientation for each of three pressures: 1, 11, and 51 atm. Increased variability in target strength and more abundant and stronger resonances are both observed with increasing depth. The respective backscattering cross sections have been averaged with respect to each of four normal distributions of tilt angle, and the corresponding target strengths have been regressed on the logarithm of fish length. The tilt-angle-averaged backscattering cross sections at the highest pressure have also been averaged with respect to frequency over a 2-kHz band for representative conditions of insonification. For all averaging methods, the mean target strength changes only slightly with depth. © *2003 Acoustical Society of America.* [DOI: 10.1121/1.1619982]

PACS numbers: 43.30.Gv, 43.30.Sf [RAS] Pages: 3136–3146

I. INTRODUCTION

Numerous studies witness to the importance of fish target strength.[1–5] This is, for example, a key quantity in the echo integration method of determining the numerical density of fish.[6] It is also important in the echo counting method of density determination, as it appears in the sampling-volume term.[7]

In general, the target strength depends on fish size, orientation relative to the direction of incidence, acoustic frequency, biological state, depth, and depth history. A large number of studies have attempted to elucidate some of these dependences. References 4 and 8–12 are illustrative.

Determination of the depth dependence has been problematical for several reasons. *In-situ* observation based on free-swimming, unconfined fish is difficult for want of control over the fish, especially that of behavior through the orientation distribution, which may change with depth. When confined, the influence of captivity as a stressor must be suspected. The degree to which the fish controls the surface tension on the swimbladder wall may be significant, thus potentially affecting the target strength.[13,14]

Notwithstanding these comments, the depth dependence of target strength from swimbladdered fish lacking *rete mirabile* seems clear: Boyle's law, or the inverse relationship of ambient pressure and volume, is operative. The mass of gas in the swimbladder is constant, and the swimbladder volume diminishes with depth, affecting the target strength.[11] For swimbladdered fish possessing *rete mirabile*, the swimbladder volume can be regulated, presumably to maintain a state of fixed buoyancy independent of depth. Given the similar mass densities of fish flesh and sea water and similar compressibilities, such fish may be expected to maintain their swimbladders in a state of constant volume. If the swimbladder shape also remains constant, the target strength may be expected to remain more or less constant, with any difference in target strength being due to the increased mass density of gas with depth.

It is the present aim to investigate the effect of increased mass density of swimbladder gas with depth on the target strength of swimbladdered fish that maintain a constant gas volume. The particular fish are members of the gadoid family, specifically pollack (*Pollachius pollachius*) and saithe (*Pollachius virens*) for which the orientation dependence of target strength has already been measured[15] and swimbladder morphometrics, performed by Ona's method,[16] are available. The approach is by theoretical modeling with the boundary-element method, applied in a preceding study to the same specimens, but under assumption there of an empty swimbladder volume corresponding to an ideal pressure-release boundary.[17]

II. BOUNDARY-ELEMENT METHOD (BEM)

In the acoustic boundary-element method, the Helmholtz equation $(\nabla^2+k^2)p=0$, where k is the wavenumber, is recast as an integral equation in which the acoustic pressure p

---

[a)] Author to whom correspondence should be addressed. Electronic mail: kfoote@whoi.edu at any point is expressed in terms of the pressure and normal displacement (or velocity) fields on the surface S of the scatterer.[18–20] To solve for the unknown fields, this integral equation is evaluated at each node associated with the set of discrete elements that collectively span S, thus producing a system of simultaneous equations for the pressures and displacements at those nodes. The solution to this system may then be used to determine the pressure at any other point using a numerical form of the original integral equation.

The exterior form of the standard integral equation is known to suffer from singularities at certain critical frequencies.[21] Solutions to the integral equation may be nonunique. At critical frequencies, the aberrant solutions are physically inadmissible,[22] which raises the problem of distinguishing these in numerical solutions.

Various methods exist to overcome the problem of critical frequencies, for example, those described in Refs. 23–28. The method available to the authors is based on Burton and Miller's approach,[24] in the particular form developed in Ref. 29 and applied in Ref. 17. This incorporates a second integral equation, the normal derivative form, which is obtained by differentiating the standard form with respect to the normal direction at the surface. The two integral equations are combined by adding a multiple α of the normal derivative form to the standard form. The value of this coupling parameter was not specified by Burton and Miller; later authors have made various suggestions, e.g., Refs. 30–32, the consensus being that α should have a non-zero imaginary part and vary inversely as the wavenumber. Terai's recommendation[31] that $\alpha=-i/k$ has been adopted in the present work. The combined integral equation approach, in the particular formulation used here, is referred to as the partial Helmholtz gradient formulation (pHGF), while that of the standard integral equation is referred to simply as the standard formulation (SF).

Interestingly, inclusion of a fluid region interior to the scattering surface S, as in the current work, may be sufficient in itself to render the standard integral equation reliable at all frequencies, although this remains unproven. Because of the higher degrees of singularity of integrands in the pHGF, which are integrable, there is a nominal penalty to be paid: lesser precision relative to that achieved with the SF at noncritical frequencies.

To achieve the highest precision and accuracy, therefore, the pHGF is used to identify possible critical frequencies. In their apparent absence, the SF is used to describe the numerical results. The general pHGF is now introduced; the SF is derived from this by equating α to zero.

A. Exterior equations

The system of equations, in matrix form, is given by

$$\mathbf{A}\mathbf{p}=\mathbf{B}\mathbf{u}-\mathbf{p}_{\text{inc}}-\alpha\frac{\partial \mathbf{p}_{\text{inc}}}{\partial n} \tag{1}$$

where $\mathbf{p}$ is the pressure field and $\mathbf{u}$ is the normal component of the displacement field due to the incident pressure field $\mathbf{p}_{\text{inc}}$, with time variation $\exp(i\omega t)$ understood, where ω is the angular frequency. The coefficients of the matrices $\mathbf{A}$ and $\mathbf{B}$ are assembled from local matrices pertaining to each element of the mesh. In performing the assembly, it is necessary to distinguish between the *global* label of a node, which is the label in the complete, global mesh, and the *local* node, which is the label of the node relative to an element on which it lies. With the calculation point of the Helmholtz integral taken at global node i, with position $\mathbf{r}_i$, integration over element m provides the following coefficients in the standard formulation:

$$a_{mn}^{(1)}(\mathbf{r}_i)=\int_{S_m} N_n(\mathbf{q})\frac{\partial G(\mathbf{r}_i,\mathbf{q})}{\partial n_q}\,\mathrm{d}S_q, \tag{2a}$$

$$b_{mn}^{(1)}(\mathbf{r}_i)=\rho\omega^2\int_{S_m} N_n(\mathbf{q})\cos\theta_{mn}G(\mathbf{r}_i,\mathbf{q})\,\mathrm{d}S_q, \tag{2b}$$

where ρ is the fluid density, $\omega=ck$, c is the speed of sound, $\mathbf{q}$ is the position vector of the integration point on the element surface S_m, G is the Green's function, given by $G(\mathbf{r}_i,\mathbf{q})=e^{-ik|\mathbf{r}_i-\mathbf{q}|}/4\pi|\mathbf{r}_i-\mathbf{q}|$, n is the local nodal label, and $N_n(\mathbf{q})$ ($n=1,2,\ldots,6$ for triangular elements, $n=1,2,\ldots,8$ for quadrilateral elements) are the shape functions, which are of the standard second-order, or quadratic, form.[33] The factor $\cos\theta_{mn}$ is included to allow for the deviation θ_{mn} of the normal to the element m at local node n from the mean normal at that node. This deviation is inherent in the quadratic formulation. The mean is weighted according to the differential area of each element at the node where they meet.

The normal derivative form of the Helmholtz integral equation, calculated at the centroids $\overline{\mathbf{r}}_l$ of the elements, similarly provides coefficients as follows:

$$a_{mn}^{(2)}(\overline{\mathbf{r}}_l)=\int_{S_m} N_n(\mathbf{q})\frac{\partial^2 G(\overline{\mathbf{r}}_l,\mathbf{q})}{\partial n_r\partial n_q}\,\mathrm{d}S_q, \tag{3a}$$

$$b_{mn}^{(2)}(\overline{\mathbf{r}}_l)=\rho\omega^2\int_{S_m} N_n(\mathbf{q})\cos\theta_{mn}\frac{\partial G(\overline{\mathbf{r}}_l,\mathbf{q})}{\partial n_r}\,\mathrm{d}S_q, \tag{3b}$$

where the normal derivative is evaluated at the centroid. These are combined with the previous coefficients by adding a multiple of $a_{mn}^{(2)}(\overline{\mathbf{r}}_l)$ or $b_{mn}^{(2)}(\overline{\mathbf{r}}_l)$, respectively, for all elements l on which global node i lies, i.e.,

$$a_{mn}(\mathbf{r}_i)=a_{mn}^{(1)}(\mathbf{r}_i)+\alpha_i\sum_{l:i\in S_l} a_{mn}^{(2)}(\overline{\mathbf{r}}_l), \tag{4a}$$

$$b_{mn}(\mathbf{r}_i)=b_{mn}^{(1)}(\mathbf{r}_i)+\alpha_i\sum_{l:i\in S_l} b_{mn}^{(2)}(\overline{\mathbf{r}}_l), \tag{4b}$$

where the combination factor α_i is taken to be $-i/kM_i$, following Terai's recommendation,[31] but allowing for the number M_i of elements meeting at node i.[29–31]

The coefficients $a_{mn}(\mathbf{r}_i)$ and $b_{mn}(\mathbf{r}_i)$ are assembled into the global matrices $\mathbf{A}$ and $\mathbf{B}$ by summing the coefficients that correspond to the same global node, thus

$$A_{ij}=\sum_{m,n:C(m,n)=j} a_{mn}(\mathbf{r}_i)-\beta(\mathbf{r}_i)\delta_{ij}, \tag{5a}$$

$$B_{ij}=\sum_{m,n:C(m,n)=j} b_{mn}(\mathbf{r}_i), \tag{5b}$$

where $C(m,n)$ is the global node label of local node n on element m. The quantity $4\pi\beta(\mathbf{r})$ is the solid angle occupied by the fluid region surrounding the point $\mathbf{r}$.[31] For $\mathbf{r}$ entirely within the fluid region, $\beta=1$; for $\mathbf{r}$ on the surface S separating the fluid region from its neighbor, $\beta=0.5$ provided that S is smooth at $\mathbf{r}$. For non-smooth surfaces such as those defined by the boundary-element meshes, methods of determining β are described in Ref. 29.

The source terms in Eq. (1) are evaluated thus:

$$\mathbf{p}_{\mathrm{inc}}(\mathbf{r}_i)+\alpha_i\sum\frac{\partial p_{\mathrm{inc}}(\bar{\mathbf{r}}_l)}{\partial n_r},$$

where the summation is performed for all elements l on which the global node i lies.

B. Interior equations

The fundamental equation in the interior of the swimbladder resembles that of Eq. (1) but without the exciting pressure field $\mathbf{p}_{\mathrm{inc}}$. Thus,

$$\mathbf{A}_1\mathbf{p}-\mathbf{B}_1\mathbf{u}=0. \tag{6}$$

The matrices $\mathbf{A}_1$ and $\mathbf{B}_1$ resemble the respective matrices $\mathbf{A}$ and $\mathbf{B}$, but use the properties of the internal gas rather than those of the external fluid. In addition, the normal direction is oriented into the gas, hence it is reversed with respect to the normal direction in the exterior. The solid angle is similarly referred to the interior, hence

$$\beta_1=1-\beta, \tag{7}$$

at any point on S. With these conditions, a set of equations similar to those of Eqs. (2)–(5) can be developed.

C. Simultaneous solution

Pressure and normal displacement are continuous across the water–gas interface S, i.e., the nodal pressures and normal displacements in Eq. (1) are identical to those in Eq. (6). There are therefore as many unknown values of pressure and displacement as there are independent equations, namely $2N$, where N is the number of nodes on S. The simultaneous solution of Eqs. (1) and (6) is derived directly:

$$\mathbf{u}=(\mathbf{B}-\mathbf{A}\mathbf{A}_1^{-1}\mathbf{B}_1)^{-1}\left(\mathbf{p}_{\mathrm{inc}}+\alpha\frac{\partial\mathbf{p}_{\mathrm{inc}}}{\partial n}\right), \tag{8}$$

and

$$\mathbf{p}=\mathbf{A}_1^{-1}\mathbf{B}_1\mathbf{u}. \tag{9}$$

D. Scattered field

The scattered pressure at an exterior point $\mathbf{r}$ is obtained from the standard integral equation by calculating coefficients similar to $a_{mn}^{(1)}(\mathbf{r}_i)$ and $b_{mn}^{(1)}(\mathbf{r}_i)$, but with $\mathbf{r}_i$ replaced by the position vector $\mathbf{r}$:

$$a_j^{(3)}(\mathbf{r})=\sum_{m,n:C(m,n)=j}\int_{S_m}N_n(\mathbf{q})\frac{\partial G(\mathbf{r},\mathbf{q})}{\partial n_q}\,\mathrm{d}S_q, \tag{10a}$$

$$b_j^{(3)}(\mathbf{r})=\rho\omega^2\sum_{m,n:C(m,n)=j}\int_{S_m}N_n(\mathbf{q})\cos\theta_{mn}G(\mathbf{r},\mathbf{q})\,\mathrm{d}S_q, \tag{10b}$$

and then

$$p(\mathbf{r})=\mathbf{a}^{(3)}(\mathbf{r})\cdot\mathbf{p}-\mathbf{b}^{(3)}(\mathbf{r})\cdot\mathbf{u}, \tag{11}$$

where the dot-product operations are indicated. The backscattering amplitude at finite range r is

$$f(r)=\frac{r|p(\mathbf{r})|}{|p_{\mathrm{inc}}|}. \tag{12}$$

The farfield backscattering amplitude f is the limit of $f(r)$ as r approaches infinity. Expressions for the backscattering cross section σ and target strength TS are derived by substituting $f(r)$, or f, in the following equations:

$$\sigma=4\pi|f|^2 \tag{13}$$

and

$$\mathrm{TS}=10\log\left[\frac{\sigma}{4\pi r_0^2}\right], \tag{14}$$

where r_0 is a reference distance, assumed here to be 1 m.

E. Numerical evaluation techniques

The elements used here are quadrilaterals and triangles of the quadratic isoparametric type, in which both the geometric and acoustic quantities are interpolated from the nodal values using quadratic shape functions, the nodes being situated at the vertices and mid-sides.[33] Experience suggests that good representation of the acoustic variables is obtained if the lengths of the sides of the elements are less than one-third of a wavelength.[17] The accuracy of geometrical representation depends on the degree of undulation of the surface, but it should be noted that the quadratic interpolation allows the sides and faces of the elements to be curved. Further details of the formulation and equations can be found in Ref. 29.

In evaluating the coefficients in Eqs. (1) and (6), Gauss quadrature is used.

III. INDEPENDENT VALIDATION OF BEM

The BEM has been validated previously for application to surface-adapted gadoids, but assuming that the swimbladder acts as a void.[17] The BEM was also tested against the example of scattering by a spherical void for which a series solution is available.

For application to problems of scattering by a swimbladdered fish at depth, the method is tested against the analytical (series) solutions[34,35] for two test cases. The object in both cases is a constant-volume gas-filled sphere of diameter 50 mm. In the first case, bistatic scattering for an incident wave of frequency 50 kHz is described over the angular range 180° as measured from the forward direction at each of two pressures, 1 and 51 atm, corresponding to the nominal depths of 0 and 500 m. The values of density ρ and sound speed c were taken to be 1025 kg/m^3 and 1470 m/s, respectively, in water; 1.247 kg/m^3 and 337.4 m/s, respectively, in air at 1 atm; and 63.597 kg/m^3 and 337.4 m/s, respectively, in air at 51 atm. The mass density of swimbladder gas is assumed to change in proportion to pressure to maintain a constant volume. For the BEM, the mesh representing the sphere was formed from elements delineated by lines of latitude and

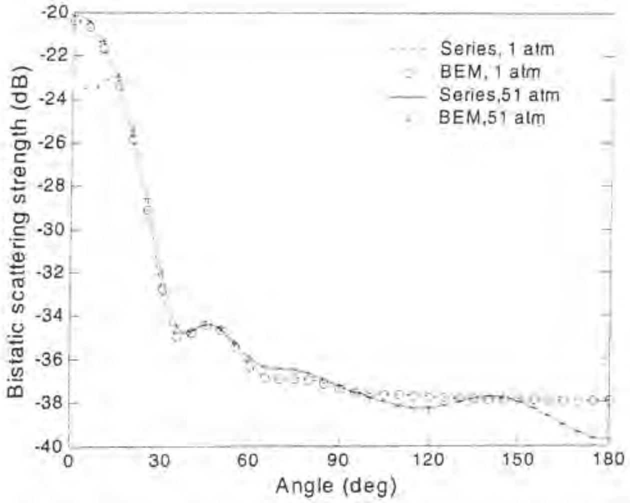

FIG. 1. Bistatic scattering strength in decibels as a function of scattering angle for a plane wave of frequency 50 kHz incident on a spherical air bubble of diameter 50 mm, at pressures of 1 and 51 atm. The analytical (series) solution is shown by the continuous and broken lines, while the BEM predictions are shown as discrete points. The scattering angle is relative to the direction of incidence, so that 0° represents the forward direction.

longitude at 2.25° intervals. By invoking rotational symmetry, the problem was reduced to one of solving for the surface pressures and displacements on only one segment, consisting of 80 elements between adjacent meridians. The results shown in Fig. 1 indicate an excellent agreement between the BEM and the analytical solution. Results with the pHGF and SF are indistinguishable.

In the second test case, the target strength of a similar gas-filled sphere is computed over the frequency range 1 Hz to 50 kHz, again at pressures of 1 and 51 atm, with densities and sound speeds as given above. The target strength was initially calculated using the analytical solution at 1-Hz intervals. In the neighborhood of each of the numerous peaks and troughs identified from these initial results, further calculations were then performed at increasing resolution, down to 0.001 Hz as required, in order to identify the peak or trough TS values to within 0.1 dB. For the BEM, the longer computing times made it impractical to compute solutions to the same resolution of 1 Hz over the whole frequency range. Instead, the target strength was calculated initially at 100-Hz intervals, and then at finer resolution around the peaks and troughs as identified in the analytical solution, again with the aim of determining the predicted peak or trough TS value to within 0.1 dB.

The same mesh as described in the first test case was used in the frequency range 25–50 kHz. For lower frequencies, where the condition that the nodal separation should be less than $\frac{1}{6}$ of the wavelength allows for larger elements, similar meshes were used but at intervals in latitude and longitude of 4.5° for the range 12.5–25 kHz and 9° for the range 0–12.5 kHz.

The results are plotted in Fig. 2(a) for a pressure of 1

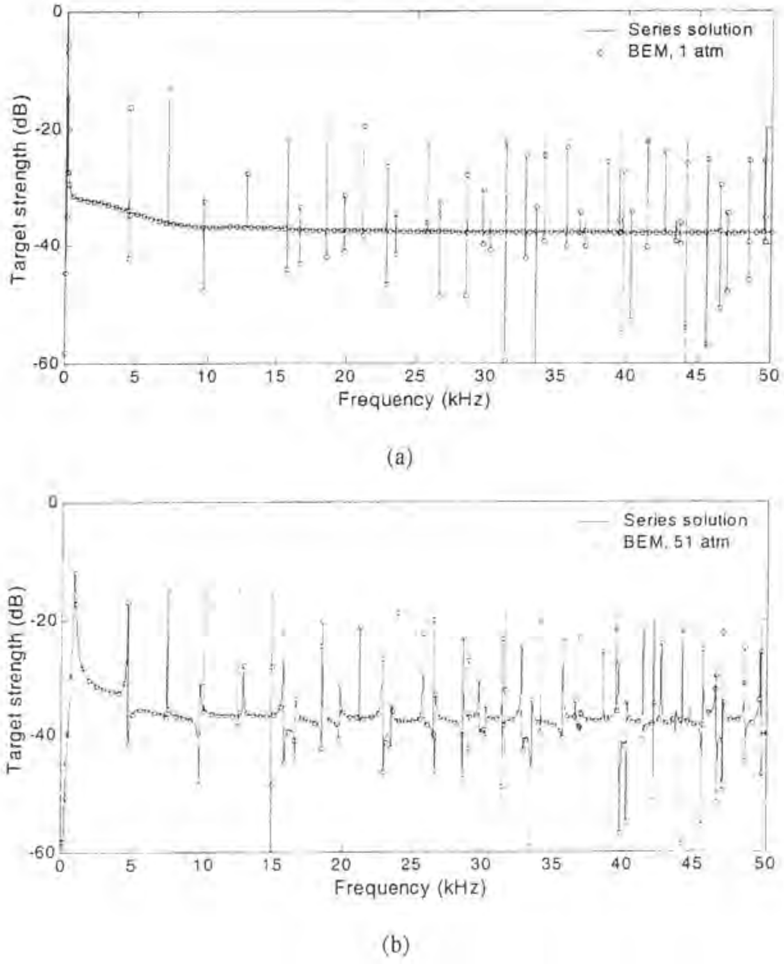

(a)

(b)

FIG. 2. Target strength of a spherical air bubble of diameter 50 mm in water at (a) 1 atm and (b) 51 atm. The analytical solution is shown by a continuous line, the BEM predictions as discrete points. In (a), the first peak, at 0.13 kHz with a TS of 5.1 dB, is truncated.

TABLE I. Properties of the 15 swimbladders and the meshes used to represent them.

Fish no.	Species	Fish length (cm)	Fish mass (g)	Meshes n_{elem}	Meshes n_{nodes}	Swimbladder Surface area (cm^2)	Swimbladder Volume (cm^3)	Nodal separation 95% limit (cm)	Nodal separation 99% limit (cm)	Nodal separation Max (cm)
201	Pollack	31.5	195	1168	3364	33.01	6.91	0.111	0.120	0.221
202	Pollack	44.0	533	1389	4041	58.83	16.33	0.126	0.137	0.177
204	Pollack	35.5	321	1078	3116	42.39	10.03	0.131	0.141	0.172
205	Pollack	39.0	380	1107	3181	45.75	11.34	0.132	0.143	0.193
206	Pollack	35.0	287	1159	3347	31.37	7.75	0.104	0.117	0.146
207	Pollack	44.5	635	1487	4363	65.24	19.15	0.124	0.134	0.161
209	Saithe	38.5	385	1501	4387	43.29	10.08	0.100	0.106	0.139
213	Pollack	34.5	259	1039	2935	34.11	7.83	0.123	0.133	0.161
214	Pollack	39.0	406	1164	3362	44.14	10.15	0.125	0.134	0.153
215	Pollack	37.0	332	1076	3092	38.89	8.75	0.124	0.134	0.174
216	Pollack	36.5	343	1062	3060	43.33	10.85	0.131	0.140	0.164
217	Pollack	34.5	253	1662	4840	32.15	6.57	0.081	0.088	0.134
218	Pollack	32.5	257	1327	3879	29.75	6.27	0.092	0.100	0.139
219	Pollack	35.5	292	1039	3005	35.74	8.15	0.120	0.127	0.153
220	Saithe	38.0	406	1321	3857	44.32	10.46	0.106	0.113	0.132

atm, and Fig. 2(b) for a pressure of 51 atm. For clarity, the BEM predictions, shown as discrete points, are plotted at intervals of 500 Hz, with the addition of the peak and trough values. The SF results are shown for giving slightly better agreement with the exact series solution. This agreement is excellent away from the peaks and in the values of the frequencies at which the peaks and troughs occur: the main discrepancies occur in the predictions of the peak and trough values at high-Q resonances. At these frequencies the system of equations solved in Eq. (8) may be less well conditioned, and numerical errors in the coefficients and in the solution of the system of equations become more significant.

While the original purpose of this test case was to investigate the performance of the BEM, the results in Fig. 2 provide insight into the effect of pressure on the target strength response when the interior fluid is included in the analysis. No resonances appear when the bubble is treated as a void, which is illustrated in Ref. 17, Fig. 2. At 1 atm, resonances appear, but with very narrow bandwidths, typically less than 1 Hz for the case considered. These bandwidths increase with increasing pressure. At 51 atm, there is a notable effect, with deviations from the smooth line of the solution for a void in the frequency bands between neighboring resonances.

IV. SWIMBLADDER MORPHOMETRY

The swimbladder morphometric data were derived from a study performed in 1980 on surface-adapted gadoids[15] by Ona's method of cryomicrotoming.[16] The data were reduced to a set of curvilinear quadrilaterals and triangles spanning each swimbladder surface, as described in Ref. 17. The statistics of the nodes at which the fundamental equations (8) and (9) were solved are described in Table I, which also summarizes information on the specimens themselves: species, length, mass, and so forth. An example of one of the meshes, that for specimen 217,[36] is shown in Fig. 3.

As earlier noted,[17] the BEM is considered valid for nodal spacings less than one-sixth of the acoustic wavelength. It is important to note that, in the case of gas-filled swimbladders, the relevant wavelength is that of the acoustic field inside the swimbladder. Relative to the wavelength λ in the exterior immersion medium with sound speed c, the interior wavelength λ_1 is

$$\lambda_1=\frac{\lambda c_1}{c}, \tag{15}$$

where c_1 is the speed of sound in the gas. Thus, whereas the nodal spacings were adequate for computations at 120 kHz in the preceding work on scattering by voids, the nodal spacings are only adequate here for computations up to about 40 kHz.

V. COMPUTATIONAL PARAMETERS

The mass density of the gas in the swimbladder at atmospheric pressure is assumed to be that of air at standard condition, namely 1.247 kg/m^3. At ambient pressure P atm, the mass density is assumed to be 1.247 P kg/m^3. The speed of sound in the gas is assumed to be 337.4 m/s, independent of depth.

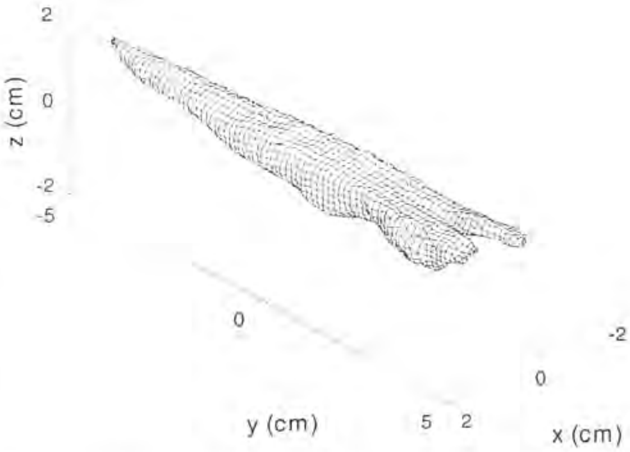

FIG. 3. Boundary-element mesh of the swimbladder to specimen 217 of Ref. 36. The meshed swimbladder length is 108 mm and the mesh has 1662 elements and 4840 nodes.

The mass density of the surrounding fish flesh is assumed to be identical to that of the seawater immersion medium, namely 1025 kg/m^3. For the assumed temperature of 5 °C and salinity of 35 ppt, the nominal sound speed in the immersion medium is 1470 m/s.

The numbers of elements and nodes for each swimbladder are given in Table I. Statistical measures of the distance between nearest-neighbor nodes are given in the same table. As mentioned, this limits the upper frequency of computation to about 40 kHz, on the basis that the length of element sides, nominally double the nodal separation, should be less than one-third of a wavelength in air.

The backscattering cross section given by Eq. (13) is averaged with respect to the orientation distribution, then expressed in the logarithmic domain according to Eq. (14). Each of four normal distributions of tilt angle are considered: N(0,0), N(0,5), N(0,10), and N(−4.4,16)°. The last distribution is derived from *in-situ* photographic observations on cod (*Gadus morhua*).[37]

Because of the effect of perspective,[38] the effective standard deviations for the four cases are 2.5, 5.5, 10.2, and 16°, respectively.[36] In terms of the normal distribution g of tilt angle θ, with mean $\bar{\theta}$ and effective standard deviation s_θ, the average backscattering cross section at frequency ν is

$$\bar{\sigma}(\nu)=\int g(\theta)\sigma(\nu,\theta)\,d\theta \Big/ \int g(\theta)\,d\theta, \qquad (16)$$

where the integration is performed over the range $[\bar{\theta}-3s_\theta,\bar{\theta}+3s_\theta]$.

Because of the presence of gas in the swimbladder cavity, resonances occur, even at high frequencies beyond the low-frequency breathing-mode resonance.[39] These could be troublesome, particularly at greater depths since the greater bandwidths of the resonances, observed in the results for the spherical bubble, make it more likely that a particular frequency will fall within such a resonance. However, there are no infinite-duration, single-frequency signals in practice: sonar measurements are performed with finite-duration signals, hence with bandwidth. Realizable receivers also have an associated bandwidth of processing. These effects have been dealt with in Ref. 40 through the following operational average of the backscattering cross section as a function of tilt angle θ for a downward-pointing transducer, here expressed in terms of the tilt-angle-averaged cross section:

$$\bar{\bar{\sigma}}=\int |SH|^2\bar{\sigma}(\nu)\,d\nu \Big/ \int |SH|^2\,d\nu, \qquad (17)$$

where S is the transmit signal spectrum and H is the receiver frequency response function, all functions of frequency ν. In the computations reported here, S is the Fourier spectrum corresponding to the signal $s(t)=\cos(2\pi\nu_0 t)\mathrm{rect}(t/\tau)$, where ν_0 is the center frequency of the transmit signal, τ is the signal duration, assumed to be 0.64 ms, and $\mathrm{rect}(x)$ is 0 for $|x|>0.5$ and 1 for $|x|\leq 0.5$. Thus, $S(\nu)=(\sin y)/y$, where $y=(\nu-\nu_0)\tau/2$. The function H is described in Fig. 4 for $\nu_0=38$ kHz.

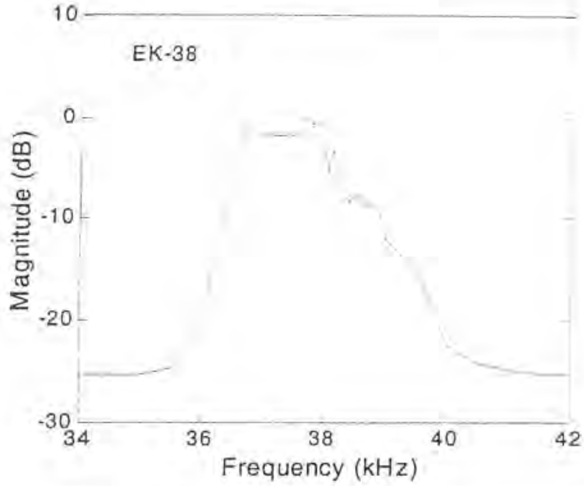

FIG. 4. Magnitude of the frequency response function of the receiver of the EK-38 echo sounder, from Fig. 4 of Ref. 40.

VI. RESULTS AND DISCUSSION

A. Comparison of computations with standard and partial Helmholtz gradient formulations

Results with the two approaches are illustrated in Fig. 5 for specimens 217 and 219. The resolution of the pHGF results is 50 Hz; that of the SF results is 25 Hz. Evidently, the agreement is very strong, but with a few differences where the pHGF results appear to be slightly more dispersed, suggesting a somewhat greater variability. As mentioned in Sec. II, this is believed to be due to the higher degrees of singularity of integrands in the pHGF compared with those in the SF, witness Eq. (3a) compared with Eq. (2b), with corresponding loss of numerical precision. By reason of assumed greater precision and accuracy, the SF is used to derive the computational results presented below.

Agreement of the corresponding results for the two approaches is poorer for some other specimens, especially when their nodal spacing approaches the λ/6-limit of applicability, where λ is the wavelength of sound in the gaseous interior of the swimbladder. At 38.1 kHz, with speed of sound in the gas of 337.4 m/s, λ/6=0.144 cm. Referring to Table I, 95% of the nodal spacings for specimen no. 219 are less than 0.120 cm. This is within 10% of the corresponding value for nodal spacing with the coarsest mesh, which applies to specimen 205.

B. Depth dependence of target strength for a single specimen

The tilt-angle dependence of target strength has been computed for each specimen at each of three pressures: 1, 11, and 51 atm. The dependences for the swimbladder modeled as a void[17] and at pressures of 1 and 11 atm are in very close agreement.

The computed tilt-angle dependence of target strength is shown for a single specimen, a 34.5-cm-long pollack, in Fig. 6. Also shown are the dependences for the case of a void of the same shape[17] and for actual measurements of the whole fish with intact swimbladder.[36]

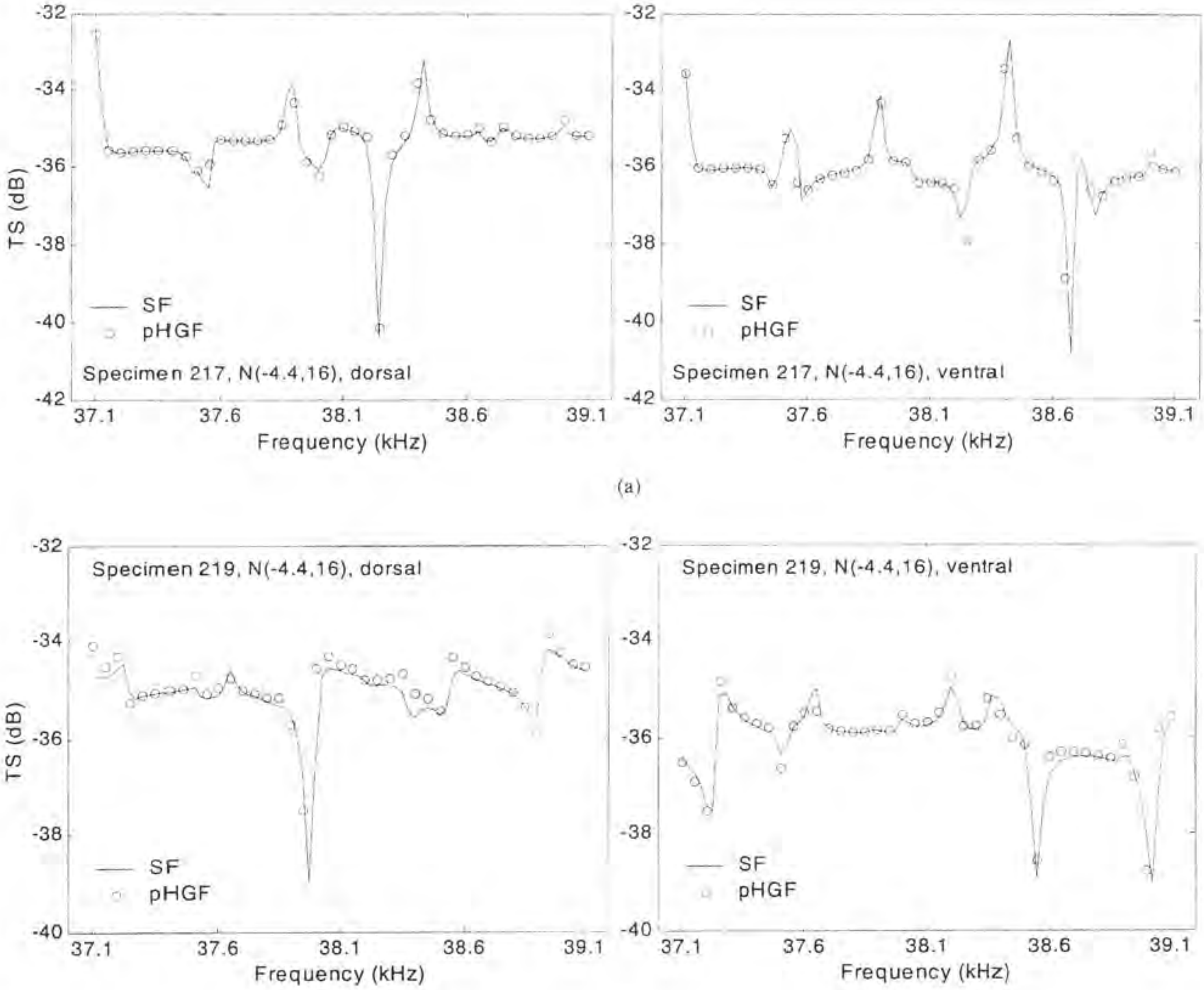

(a)

(b)

FIG. 5. Predicted target strength versus frequency for (a) specimen 217 and (b) specimen 219 in the range 37.1–39.1 kHz, at a pressure of 51 atm. Results obtained using the standard formulation (SF) of the BEM, at intervals of 25 Hz, are shown by the continuous lines; results from the partial Helmholtz gradient formulation (pHGF) are shown as discrete points, at intervals of 50 Hz.

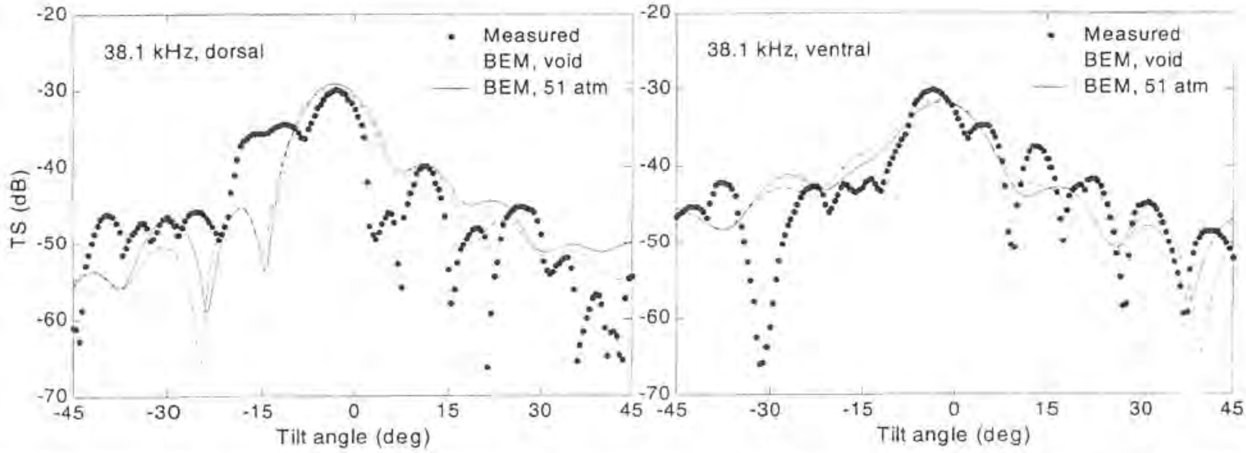

FIG 6. BEM computations of target strength as a function of tilt angle for swimbladder specimen 217, treated as a void and as gas-filled at a depth of 500 m, compared against direct measurements at 2.5-m depth. The functions are shown for both dorsal and ventral aspects at a frequency of 38.1 kHz.

TABLE II. Regression analyses of target strength on fish length, based on BEM computations of TS for 15 specimens in dorsal aspect. Averaging is performed with respect to each of four normal distributions of tilt angle at each of four pressures: 0, 1, 11, and 51 atm. The tilt-angle-averaged results at 51 atm are additionally averaged with respect to frequency, using Eq. (17), and presented in the final row for each tilt-angle distribution. Results are expressed through the regression coefficient b in Eq. (18) and standard error SE of the regression. The correlation coefficient ρ of underlying target strength values in each set is also shown.

Frequency kHz	Tilt angle (degrees)		Pressure (atm)	BEM computed TS functions		
	Mean	s.d.		ρ	b	SE
38.1	0.0	0.0	0	0.933	−61.36	1.00
38.1	0.0	0.0	1	0.933	−61.36	1.00
38.1	0.0	0.0	11	0.930	−61.38	1.00
38.1	0.0	0.0	51	0.747	−61.30	1.37
37.1–39.1	0.0	0.0	51	0.922	−61.46	1.00
38.1	0.0	5.0	0	0.945	−62.44	0.66
38.1	0.0	5.0	1	0.945	−62.44	0.65
38.1	0.0	5.0	11	0.938	−62.45	0.66
38.1	0.0	5.0	51	0.709	−62.40	1.09
37.1–39.1	0.0	5.0	51	0.930	−62.55	0.67
38.1	0.0	10.0	0	0.946	−64.18	0.47
38.1	0.0	10.0	1	0.947	−64.18	0.46
38.1	0.0	10.0	11	0.938	−64.19	0.47
38.1	0.0	10.0	51	0.664	−64.14	0.98
37.1–39.1	0.0	10.0	51	0.930	−64.28	0.49
38.1	−4.4	16.0	0	0.941	−65.76	0.40
38.1	−4.4	16.0	1	0.942	−65.76	0.39
38.1	−4.4	16.0	11	0.931	−65.76	0.41
38.1	−4.4	16.0	51	0.610	−65.68	0.96
37.1–39.1	−4.4	16.0	51	0.924	−65.81	0.43

The effect of pressure on the orientation dependence of target strength of the other 14 specimens is similar, if differing in the precise details of deviations from the respective void case and measurements.

C. Target strength—length regressions

The large number of computations that have been performed for the 15 swimbladders have been combined by averaging. In particular, the backscattering cross section computed with the BEM, and illustrated in Fig. 6 for a single specimen, have been averaged with respect to the tilt-angle distributions according to Eq. (16). The target strength corresponding to $\bar{\sigma}$ has then been computed according to Eq. (14), and the regression equation

$$\mathrm{TS}=20\log l+b \tag{18}$$

computed by the method of least squares, where l is the total fish length in centimeters. Results are shown in Table II for dorsal aspect and in Table III for ventral aspect. Scatter diagrams of target strength and fish length have been prepared for the tilt-angle distribution N(−4.4,16)° for a void and at a pressure of 51 atm. They are presented in Fig. 7.

In general, the modeled target strengths display increasing variability with increasing depth. The physical explanation for this is presently unclear, but based on the second validation example, in Fig. 2, with evidence of resonances at frequencies above the ordinary very-low-frequency breathing-mode resonance, it is speculated that stronger resonances are excited more easily at greater pressures. Thus, TS values are likely to be elevated or depressed depending on the proximity of a resonance or anti-resonance, respectively, for each specimen. Physically, the potential of the swimbladder under pressure to store acoustic energy and act as a resonator, or absorber, of incident acoustic energy seems to increase with depth. The condition that the swimbladder maintain a constant volume ensures that the mass of enclosed gas increases with ambient pressure, hence depth.

The results so far described have been for calculations of TS at single frequencies. However, as mentioned in Sec. V, sonar measurements use signals of finite duration and therefore possess bandwidth. In order to reproduce this characteristic more faithfully in the BEM predictions, further computations were undertaken in a frequency band around 38.1 kHz at the highest pressure of 51 atm, where the effect of resonance is likely to be most significant. Equation (17) provides a basis for then determining a frequency-averaged TS. A spectral band of ±1 kHz about the center frequency was found to be sufficient to account for 95% of the scattered energy. Within this band, BEM predictions were made at intervals of 50 Hz. The integral in the numerator of Eq. (17) was evaluated numerically, first as a Riemann summation, and second by fitting a cubic spline to the TS response and integrating using Simpson's rule with an interval of 10 Hz. The results of the latter method were virtually identical to those of the former, the difference in the eventual value of b in Eq. (18), for example, being generally less than 0.02 dB.

The frequency-averaged results are included in Tables II and III, as the final line in each set of results for a given tilt distribution. Scatter diagrams and regression lines are plotted

TABLE III. As Table II, but in ventral aspect.

Frequency kHz	Tilt angle (degrees)		Pressure (atm)	BEM computed TS functions		
	Mean	s.d.		ρ	b	SE
38.1	0.0	0.0	0	0.427	−64.84	1.85
38.1	0.0	0.0	1	0.425	−64.84	1.84
38.1	0.0	0.0	11	0.451	−64.91	1.87
38.1	0.0	0.0	51	0.494	−64.88	1.89
37.1–39.1	0.0	0.0	51	0.453	−64.79	1.75
38.1	0.0	5.0	0	0.684	−65.03	1.15
38.1	0.0	5.0	1	0.682	−65.03	1.14
38.1	0.0	5.0	11	0.703	−65.09	1.17
38.1	0.0	5.0	51	0.653	−65.12	1.43
37.1–39.1	0.0	5.0	51	0.736	−64.95	1.02
38.1	0.0	10.0	0	0.875	−65.79	0.66
38.1	0.0	10.0	1	0.874	−65.79	0.66
38.1	0.0	10.0	11	0.878	−65.84	0.70
38.1	0.0	10.0	51	0.823	−65.83	0.93
37.1–39.1	0.0	10.0	51	0.907	−65.69	0.57
38.1	−4.4	16.0	0	0.950	−66.74	0.41
38.1	−4.4	16.0	1	0.948	−66.74	0.41
38.1	−4.4	16.0	11	0.941	−66.79	0.47
38.1	−4.4	16.0	51	0.875	−66.74	0.74
37.1–39.1	−4.4	16.0	51	0.952	−66.62	0.39

in Fig. 8 for the tilt distribution N(−4.4,16)°, allowing a direct comparison with Fig. 7.

In the dorsal aspect, the effects of averaging over the bandwidth of the signal are to slightly decrease the TS level as given by the value of b in Eq. (18), increase the correlation, and decrease the variability when compared with the corresponding single-frequency results. In the ventral aspect, the TS level is slightly increased. The correlation is increased

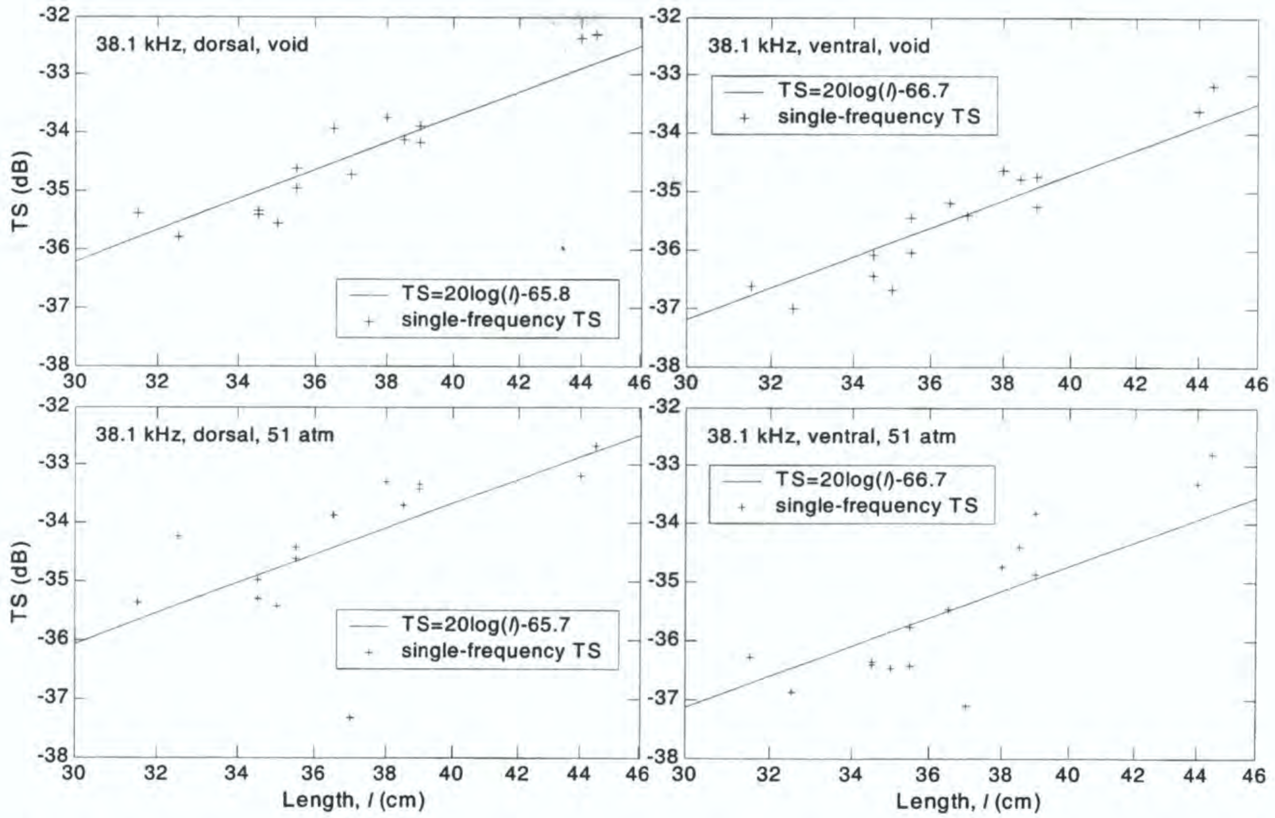

FIG. 7. Scatter diagram of target strength versus length l, expressed on a logarithmic scale, at the single frequency of 38.1 kHz for the tilt distribution (−4.4,16), for a void, and at a pressure of 51 atm, for dorsal and ventral aspects. The regression equation $\mathrm{TS}=20\log l+b$ is shown by the continuous line in each case.

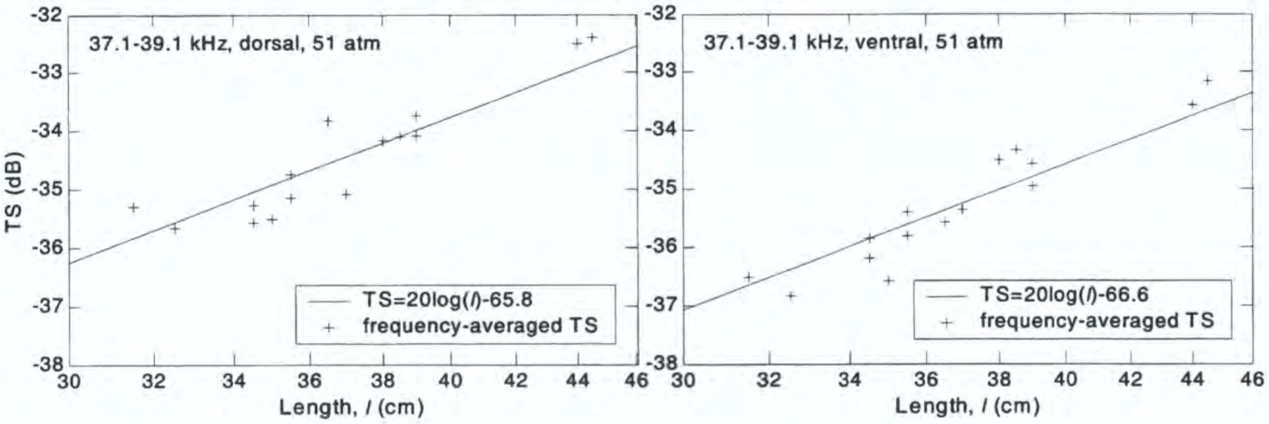

FIG. 8. As Fig. 7 at 51 atm, but for target strength averaged over the frequency band 37.1–39.1 kHz, using Eq. (17).

in all cases but one, and the variability is decreased. These weak trends probably reflect the particular locations and magnitudes of resonance frequencies in the 2-kHz band of averaging. The sample size of 15 specimens is simply too small, and the four orientation distributions are too dependent, to permit drawing stronger conclusions.

Since the depth dependence of target strength is weak, both the echo integration and echo counting methods can be applied as they are at present with at most minor corrections. More importantly, possible observed differences in *in-situ* target strength of depth-adapted gadoids may be attributed to behavior, as manifested through the orientation distribution, rather than to the simple effect of depth acting on the swimbladder volume.

D. Future work

Exercise of the BEM for the test case of a spherical gas-filled bubble revealed low- and high-frequency resonances, if without inclusion of internal damping. Only the lowest-frequency resonance seems to have been studied, suggesting future areas of experimental and theoretical investigation.

The size and shape of each swimbladder have been assumed to be constant, independent of depth. Insofar as the computations are meant to explore the depth dependence of target strength, these would describe situations in which the fish are fully depth-adapted, with inflated swimbladders. Under some circumstances of vertical migration, the rate of change in depth is so rapid that compensation by the *rete mirabile* lags behind, leading to situations of negative or positive buoyancy, as the fish is migrating respectively downwards or upwards. Examination of the change in target strength under uncompensated or partially compensated depth changes would be valuable, but requires a separate investigation. A prerequisite is knowledge of the manner of swimbladder form change with pressure change, which presently is mostly speculative.

Other swimbladder shapes and types should be amenable to computation with the BEM. A study of the Atlantic herring swimbladder, lacking *rete mirabile*, would be of particular value given that the fish is acoustically surveyed for purposes of estimating stock abundance.

Another problem waiting to be addressed is that of the induced surface velocity field on the swimbladder wall and its possible relationship to auditory function. The BEM has already been used in a preliminary study to generate the surface-velocity field,[41] and should shed light on the relationship of external acoustic stimuli and their transmission to the presumed organ of hearing.

VII. CONCLUSIONS

The effect of depth on the target strength of depth-adapted gadoids has been modeled by the boundary-element method. The mean target strength, based on the averaged backscattering cross section, has been found to change insignificantly with depth. There is, however, increased variability in the orientation dependence of target strength. In addition, it is evidently easier to excite high-frequency resonances with increasing depth.

Thus, for applications of the echo counting and integration methods[6] in acoustic surveys of gadoid abundance, there need be no change either in execution of the surveys or in interpretation of forthcoming echo data. This assumes that the gadoid swimbladder remains fully inflated at all depths of measurement. In the event that depth excursions occur or are undertaken without concurrent compensation to maintain a constant state of inflation, the target strength may be expected to change, very possibly to a significant degree depending on the extent and rapidity of the depth excursion.

ACKNOWLEDGMENTS

This work began with sponsorship by the European Commission through its RTD-program, Contract No. MAS3-CT95-0031 (BASS), and was completed with support by the Office of Naval Research, Contract No. N000140310368. Dr. P. J. Harris, University of Brighton, is thanked for discussions on the Burton–Miller formulation. Professor A. D. Pierce is thanked for discussions on the question of uniqueness. Dr. V. R. Starczak is thanked for assistance in executing preliminary BEM computations. A. Norton is thanked for much valued assistance in the technical editing. This is Woods Hole Oceanographic Institution Contribution No. 10839.

[1] R. H. Love, "Measurements of fish target strength: a review," Fish. Bull. U.S. **69**, 703–715 (1971).

[2] L. Midttun, "Fish and other organisms as acoustic targets," Rapp. P.-V. Reun.-Cons. Int. Explor. Mer **184**, 25–33 (1984).

[3] K. G. Foote, "Summary of methods for determining fish target strength at ultrasonic frequencies," ICES J. Mar. Sci. **48**, 211–217 (1991).

[4] S. McClatchie, G. Macaulay, R. F. Coombs, P. Grimes, and A. Hart, "Target strength of an oily deep-water fish, orange roughy (*Hoplostethus atlanticus*) I. Experiments," J. Acoust. Soc. Am. **106**, 131–142 (1999).

[5] K. G. Foote, "Target strength of fish," in *Encyclopedia of Acoustics*, edited by M. J. Crocker (Wiley, New York, 1997), pp. 493–500.

[6] D. N. MacLennan, "Acoustical measurement of fish abundance," J. Acoust. Soc. Am. **87**, 1–15 (1990).

[7] K. G. Foote, "Acoustic sampling volume," J. Acoust. Soc. Am. **90**, 959–964 (1991).

[8] O. Nakken and K. Olsen, "Target strength measurements of fish," Rapp. P.-V. Reun.-Cons. Int. Explor. Mer **170**, 52–69 (1977).

[9] Y. Miyanohana, K. Ishii, and M. Furusawa, "Measurements and analyses of dorsal-aspect target strength of six species of fish at four frequencies," Rapp. P.-V. Reun.-Cons. Int. Explor. Mer **189**, 317–324 (1990).

[10] S. McClatchie, J. Alsop, and R. F. Coombs, "A re-evaluation of relationships between fish size, acoustic frequency, and target strength," ICES J. Mar. Sci. **53**, 780–791 (1996).

[11] T. Mukai and K. Iida, "Depth dependences of target strength of live kokanee salmon in accordance with Boyle's Law," ICES J. Mar. Sci. **53**, 245–248 (1996).

[12] K. Sawada, Z. Ye, R. Kieser, G. A. McFarlane, Y. Miyanohana, and M. Furusawa, "Target strength measurements and modeling of walleye pollock and Pacific hake," Fish. Sci. **65**, 193–205 (1999).

[13] R. H. Love, "Resonant acoustic scattering by swimbladder-bearing fish," J. Acoust. Soc. Am. **64**, 571–580 (1978).

[14] C. Feuillade and R. W. Nero, "A viscous-elastic swimbladder model for describing enhanced-frequency resonance scattering from fish," J. Acoust. Soc. Am. **103**, 3245–3255 (1998).

[15] K. G. Foote, "Linearity of fisheries acoustics, with addition theorems," J. Acoust. Soc. Am. **73**, 1932–1940 (1983).

[16] E. Ona, "Physiological factors causing natural variations in acoustic target strength of fish," J. Mar. Biol. Assoc. U.K. **70**, 107–127 (1990).

[17] K. G. Foote and D. T. I. Francis, "Comparing Kirchhoff-approximation and boundary-element models for computing gadoid target strengths," J. Acoust. Soc. Am. **111**, 1644–1654 (2002).

[18] L. H. Chen and D. G. Scheikert, "Sound radiation from an arbitrary body," J. Acoust. Soc. Am. **35**, 1626–1632 (1963).

[19] G. Chertock, "Sound radiation from vibrating surfaces," J. Acoust. Soc. Am. **36**, 1305–1313 (1964).

[20] L. G. Copley, "Integral equation method for radiation from vibrating bodies," J. Acoust. Soc. Am. **41**, 807–816 (1967).

[21] L. G. Copley, "Fundamental results concerning integral representations in acoustic radiation," J. Acoust. Soc. Am. **44**, 28–32 (1968).

[22] A. D. Pierce, "Variational formulations in acoustic radiation and scattering," in *Underwater Scattering and Radiation*, edited by A. D. Pierce and R. N. Thurston (Academic, San Diego, 1992), pp. 195–371.

[23] H. A. Schenck, "Improved integral formulation for acoustic radiation problems," J. Acoust. Soc. Am. **44**, 41–58 (1968).

[24] A. J. Burton and G. F. Miller, "The application of integral equation methods to the numerical solutions of some exterior boundary problems," Proc. R. Soc. London, Ser. A **323**, 201–210 (1971).

[25] A. F. Seybert, B. Soenarko, F. J. Rizzo, and D. J. Shippy, "An advanced computational method for radiation and scattering of acoustic waves in three dimensions," J. Acoust. Soc. Am. **77**, 362–368 (1985).

[26] T. W. Wu, A. F. Seybert, and G. C. Wan, "On the numerical implementation of a Cauchy principal value integral to insure a unique solution for acoustic radiation and scattering," J. Acoust. Soc. Am. **90**, 554–560 (1991).

[27] T. W. Wu and A. F. Seybert, "A weighted residual formulation for the CHIEF method in acoustics," J. Acoust. Soc. Am. **90**, 1608–1614 (1991).

[28] D. J. Segalman and D. W. Lobitz, "A method to overcome computational difficulties in the exterior acoustics problem," J. Acoust. Soc. Am. **91**, 1855–1861 (1992).

[29] D. T. I. Francis, "A gradient formulation of the Helmholtz integral equation for acoustic radiation and scattering," J. Acoust. Soc. Am. **93**, 1700–1709 (1993).

[30] W. L. Meyer, W. A. Bell, M. P. Stallybrass, and B. T. Zinn, "Prediction of the sound field radiated from axisymmetric surfaces," J. Acoust. Soc. Am. **65**, 631–638 (1979).

[31] T. Terai, "On calculation of sound fields around three dimensional objects by integral equation methods," J. Sound Vib. **69**, 71–100 (1980).

[32] K. A. Cunefare and G. Koopman, "A boundary element method for acoustic radiation valid for all wavenumbers," J. Acoust. Soc. Am. **85**, 39–48 (1989).

[33] O. C. Zienkiewicz and R. L. Taylor, *The Finite Element Method*, 4th ed. (McGraw–Hill, London, 1989), Vol. 1.

[34] V. C. Anderson, "Sound scattering from a fluid sphere," J. Acoust. Soc. Am. **22**, 426–431 (1950).

[35] R. R. Goodman and R. Stern, "Reflection and transmission of sound by elastic spherical shells," J. Acoust. Soc. Am. **34**, 338–344 (1962).

[36] K. G. Foote, "Rather-high-frequency sound scattering by swimbladdered fish," J. Acoust. Soc. Am. **78**, 688–700 (1985).

[37] K. Olsen, "Orientation measurements of cod in Lofoten obtained from underwater photography, and their relation to target strength," Counc. Meet. Int. Counc. Explor. Sea 1971/B:17.

[38] K. G. Foote, "Averaging of fish target strength functions," J. Acoust. Soc. Am. **67**, 504–515 (1980).

[39] National Defense Research Committee, "Physics of sound in the sea" (Department of the Navy, Washington, D.C., 1969), Chap. 28.

[40] K. G. Foote, "Optimizing copper spheres for precision calibration of hydroacoustic equipment," J. Acoust. Soc. Am. **71**, 742–747 (1982).

[41] D. T. I. Francis and K. G. Foote, "Acoustic excitation of the fish swimbladder," Bioacoustics **12**, 265–267 (2002).

Technical Communications

A Technique for Calibration of Monostatic Echosounder Systems

Svein Vagle, Kenneth G. Foote,
Mark V. Trevorrow, and David M. Farmer

***Abstract*—A calibration technique has been adapted to render complete system calibrations of high-frequency acoustical instrumentation. This is based on standard targets; specifically, precisely manufactured spheres composed of tungsten carbide with 6% cobalt binder. The use of multiple sphere sizes was found to be advantageous, both as an independent check of the calibrations, and so that resonances in the sphere responses at certain frequencies could be avoided. Complete system gains and beam patterns, which include effects of bandpass filters and finite-pulse lengths, were determined by moving the spheres individually in the transducer far-fields. Use of this procedure ensures control over the acoustical characteristics of transducers, which may change from the time of manufacture and first testing due, for example, to platform mounting. It also provides a direct means of measuring the sampling volume at relatively high and constant signal-to-noise ratios. Implementation of this technique is discussed using a multifrequency sonar system as an example.**

I. Introduction

High-frequency sonar systems are being used extensively for biological and physical studies. The use of multiple frequencies makes it possible to discriminate between different sizes and species of zooplankton and fish as well as different bubble sizes [1], [2]. Here, a generally applicable accurate calibration technique is presented, based on the use of spheres composed of tungsten carbide with 6% cobalt binder, referred to simply as tungsten carbide spheres. In this technique consistency is checked through use of several different sphere sizes. Beam shape characteristics are measured by moving the target sphere following a known pattern in the transducer far field. The combined intensity response from transmitter and receiver electronics is determined by matching observed echo intensity on the transducer main axis to calculated sphere target strength. This technique calibrates the entire acoustic system in an *in situ* operational state, and thus includes influences of sonar mounting, underwater cabling, salt vs. fresh water, etc.

Studies by Miyanohana and his co-workers [3] have shown that tungsten carbide is a superior material to use at higher acoustical frequencies. Calibration using backscatter from standard targets is common for the comparatively low frequencies (<200 kHz) used in fisheries research [4]. Several multifrequency systems for plankton survey have been calibrated using the principle of self-reciprocity with the ocean surface as a reflector [5], [6]. However, it is often difficult to ensure absolutely flat surface conditions, especially for high frequency sonars and often the surface returns are strongly saturated. One of the main advantages of the calibration scheme presented here is that the instrumentation to be calibrated is configured in its field operation mode. It is fortunate that the tungsten carbide calibration spheres have scattering characteristics similar to the targets of interest, such as micro-bubbles, zooplankton and fish. Several papers discuss the use of a single target sphere to calibrate wide-band fish-measuring systems [7], [8]. However, these systems operate at frequencies well below the first resonance of the chosen target. Foote [9] proposed the use of several calibration spheres with different radii to avoid the resonant frequencies of any particular sphere, and Miyanohana *et al.* [3] demonstrated that echo-sounders operating at any frequencies between 10 and 200 kHz can be calibrated using readily available calibration spheres. With these calibration methods the appropriate sphere must be carefully positioned on the main axis of the transducer being calibrated, generally requiring controlled laboratory conditions.

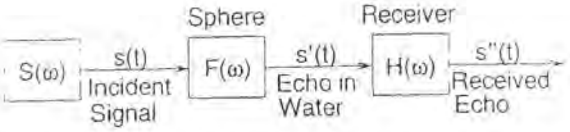

Fig. 1. Schematic diagram of acoustic backscattering as a filtering process.

Here, we discuss the implementation of this approach with a motor driven target support that moves the spheres in a raster scan. A specific application to a multifrequency sonar is used to illustrate the technique.

II. Theory

There are three common methods for calibration of acoustical instruments comparison with a calibrated transducer or hydrophone, surface reciprocity, and backscatter from standard targets. It is the third approach that is followed here. Several studies have established the utility of solid elastic spheres as calibration targets [10], [11]. Acoustic backscatter from a discrete body consists of ensonification, echo formation, and echo reception. Several earlier theoretical studies have been based on the assumption of continuous-wave ensonification [12] or hydrophone-type reception, i.e., with flat receive frequency response function [13], [14]. Here, the operational effects of observing finite-duration echoes using intrinsically narrow-band, frequency sensitive transducers such as sonars must be incorporated directly into theory [10].

For a generic monostatic acoustical system, the total response to distributed volume scatterers can be expressed using the standard sonar equation [6],

$$\mathrm{TS} \equiv 10\log_{10} S_V r_0 = \mathrm{RL{-}SL} + 2\mathrm{TL} - 10\log_{10} V \qquad (1)$$

where TS is the target strength (dB), which is defined in terms of the backscattering cross section per unit volume S_V as shown. Also, RL–SL represents the ratio of the received acoustical power (receive level) to the transmitted power (source level), 2TL is the two way transmission loss due to spherical spreading and frequency dependent absorption [$\mathrm{TL} = 20\log_{10} r + \alpha(f)\cdot r$], where r is the range from the transducer, V is the insonified volume and r_0 is the reference distance of 1 m. The nominal insonified volume depends on the beam pattern of any individual transducer and the pulse length, L, as

$$V = \left(\frac{\Phi}{3}\right)\left[\left(r + \frac{L}{4}\right)^3 - \left(r - \frac{L}{4}\right)^3\right] \qquad (2)$$

Manuscript received June 21, 1994; revised February 13, 1996.

S. Vagle, M. V. Trevorrow, and D. M. Farmer are with the Acoustical Oceanography Group, Institute of Ocean Sciences, 9860 W. Saanich Road, P.O. Box 6000, Sidney, BC V8L 4B2 Canada.

K. G. Foote is with the Institute of Marine Research, P.O. Box 1870 Nordnes, N-5024 Bergen, Norway.

Publisher Item Identifier S 0364-9059(96)05665-8.

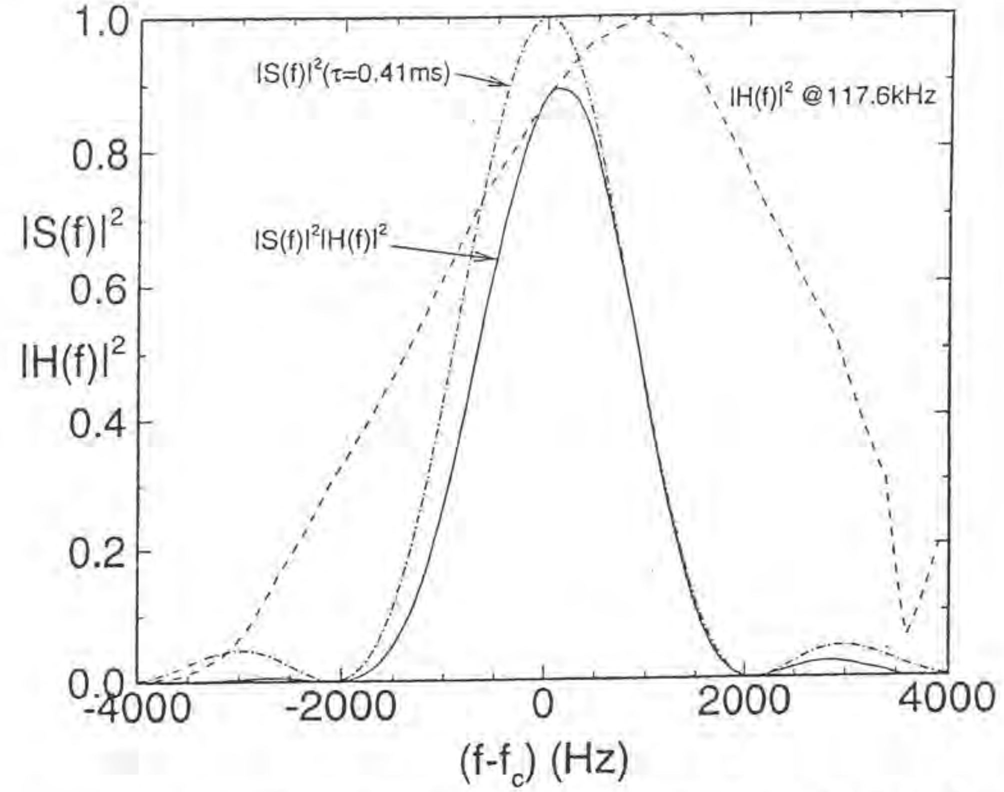

Fig. 2. Total receive frequency response $|H(f)|^2$ for a 117.6-kHz sonar. Also shown is the transmit spectrum $|S(f)|^2$ for a square pulse of length 0.41 ms, and the product $|S(f)|^2|H(f)|^2$. Here, f_c is the transmit frequency.

where $L = c\tau$, τ is the transmit pulse duration in seconds (see Table II), c is the local sound speed, and Φ is the equivalent solid angle of the beam pattern. Here, Φ is defined as the solid angle in which an ideal beam pattern of unit relative response replaces the actual measured beam pattern. Beyond Φ the relative response is zero. This solid angle is one of the parameters to be determined for each transducer by these calibrations. The absorption coefficient, $\alpha(f)$ is a function of frequency, temperature and salinity. The range from the transducers to a given target and the pulse length are calculated using the local sound speed c derived from CTD (conductivity, temperature versus depth) data [15].

By using the filtering analogy outlined in Fig. 1, and the common assumption of linearity, the component processes are strictly multiplicative in the frequency domain. The frequency spectrum $S_R(f)$ of the received time-signal $s_R(t)$ is related to the spectra $S(f)$ of the transmitted signal $s(t)$, and $S'(f)$ of the reflected signal $s'(t)$ by the relation

$$S_R(f) = S'(f)H(f) = S(f)F(f)H(f) \tag{3}$$

where $H(f)$ is the frequency response function of the receiver, and $F(f)$ is the monochromatic backscattering amplitude of the target. For present purposes, this is assumed to be indistinguishable from the corresponding far-field amplitude, which is justifiable since typical measurement ranges (see Section IV) far exceed the factor of ten times the sphere radius specified by Hickling [16] as a condition for using the far-field or plane-wave amplitude instead of the rigorous finite-field-distance or spherical-wave amplitude. Then the basic definition of the sphere backscatter cross section σ is

$$\sigma \equiv 4\pi \frac{\int_0^\infty |\mathrm{SFH}|^2\, df}{\int_0^\infty |\mathrm{SH}|^2\, df} = 4\pi \frac{\int_0^\infty |S|^2|F|^2|H|^2\, df}{\int_0^\infty |S|^2|H|^2\, df}. \tag{4}$$

The target strength for a single object in the beam is defined as $10\log_{10}\sigma/(4\pi r_0^2)$, where $r_0 = 1$ m. In the limit as the insonifying wave becomes monochromatic, $\sigma = 4\pi|F|^2$. Expressions for $|S|^2$, $|H|^2$, and $|F|^2$ are now obtained.

1) Finite-Pulse Ensonification: Digitally produced transmit signals generated in sonar systems have time variations which closely resemble square pulses. For a sinusoidal signal with center frequency f_c and duration τ, $|S|$ will have the characteristic $\sin(x)/x$ form, where $x = \pi(f - f_c)\tau$. Therefore,

$$|S|^2 = \left(\frac{\sin(\pi(f - f_c)\tau)}{\pi(f - f_c)\tau}\right)^2. \tag{5}$$

In Fig. 2, $|S|^2$ is plotted for a pulse duration of 0.41 ms.

2) Receiver Frequency Response: The total frequency response function of a receiver system, $H(f)$, result from a combination of the frequency characteristic of the specific transducer and the frequency response of the analog and digital receiver circuitry. The transducer response function is commonly supplied by the transducer manufacturer or can easily be obtained from straight-forward transmission measurements with a source of known frequency response. The frequency response of the receiver systems can be determined by feeding electrical signals of known frequency and amplitude into the analog receiver circuitry and recording the resultant output. Fig. 2 shows the total frequency response function and its product with the transmitter spectrum for a 117.6 kHz sonar.

3) Monochromatic Scattering from Tungsten Carbide Spheres: The monochromatic far-field backscattering amplitude $F(f)$ in (4) is well known (e.g., [16], with comments on a missing factor [3] and [10]). This backscatter amplitude is a complicated function of frequency, sphere size and elastic properties, and water properties. It is necessary to compute these functions numerically for each of the

TABLE I
PHYSICAL CONSTANTS USED FOR CALCULATING THE TARGET STRENGTH OF TUNGSTEN CARBIDE CALIBRATION SPHERES IN SEA WATER ASSUMING WATER TEMPERATURE OF 10.9 °C AND SALINITY OF 31 ppt

Constant	Value
sphere material	tungsten carbide with 6% Cobalt
sphere radius	0.01905, 0.0200, and 0.0215 m
sphere density	14900 kg/m^3
sphere compressional sound speed	6853 m/s
sphere transverse sound speed	4171 m/s
water density	1022.7 kg/m^3
sound speed in water	1486.5 m/s

TABLE II
SUMMARY OF SONAR CHARACTERISTICS. THE VALUES FOR THE ABSORPTION COEFFICIENT $\alpha(f)$ TAKEN FROM [18], ASSUMING WATER TEMPERATURE OF 10.9 °C AND SALINITY OF 31 ppt

Transmit frequency, f_c (Hz)	Pulse duration, τ (ms)	Far-field range (m)	Absorption, α (dB/m)
29400	0.54	1.40	0.006
51450	0.41	0.83	0.014
88200	0.41	0.74	0.030
117600	0.41	2.30	0.040
198450	0.41	3.98	0.060
396900	0.41	2.69	0.1

sonar frequency bands and ambient water properties. The quantity $|F|^2$ is plotted in Fig. 3 over the frequency range from 20 to 415 kHz for the three sphere sizes. The constants used in the calculations are summarized in Table I for the water properties discussed in Section IV. For frequencies less than approximately 75 kHz, $|F|^2$ is a relatively smooth function of frequency for all three spheres. However, at higher frequencies the sphere cross-sections reveal prominent peaks and dips corresponding to resonant frequencies of elastic oscillations of the sphere [17], sometimes exceeding a factor of 100 reduction. Also, the precise resonant frequencies are very sensitive to small changes in sphere characteristics and water properties. Because of the finite bandwidth of the transmitted signals (approx. ±2 kHz), these resonant drop-outs must be included in the estimation of effective sphere cross-section. The frequency integral approach specified in (4) should (theoretically) handle these resonant drop-outs, but small errors in sphere and water properties have the potential for altering the effective cross section. For example, at a frequency of 88 kHz the results from the 38.1 and 40.0 mm spheres could be sub-optimal. The use of three spheres allows some assessment of the magnitude of this uncertainty.

4) Sensitivity Analysis: The backscattering cross section in (4) was evaluated over a range of conditions in addition to the nominal condition described in Table II. These evaluations explored effects due to variations in water temperature, sphere elastic properties, transmit frequency, and pulse duration. From this it was apparent that the different sphere sizes are not equally usable for all sonar frequencies, reinforcing the impression given by inspection of Fig. 3. This also provided quantitative grounds on which to decide which sphere or spheres to use for a particular sonar channel.

5) Target Strength Calibrations: The backscatter amplitude at the center of the insonifying beam of each transducer is determined by searching for the maximum echo intensity from the sphere. The fundamental quantity of interest is the total energy content in the target echo as compared to the total energy in the transmitted pulse, represented in (1) as the terms RL–SL. The total energy output of the pulse will be proportional to the transmitted voltage, U_t, and the corresponding backscattered energy will be proportional to the transducer received voltage, U_r. Then, for finite-duration pulses the measured backscattering cross section, σ_m, is proportional to time integrals of U_t and U_r, i.e.,

$$\sigma_m = K \frac{\int_{t_1}^{t_2} |U_r|^2 \, dt}{\int_0^{\tau} |U_t|^2 \, dt} \tag{6}$$

where K is a proportionality constant and the integration limits are chosen to include the periods when the received signals are significantly above the noise level, which typically included between 7 and 10 samples. For the receiver, the digitally recorded 16-b amplitudes, N, are proportional to the received voltage from the transducer, U_r, i.e., as

$$N = \beta \cdot U_r \tag{7}$$

where β is a proportionality coefficient including the amplifier gains and analog-to-digital conversion. By converting from time to range using the local sound speed c and combining (6) and (7), we get in terms of the range dependent recorded amplitudes, $N(r)$, that

$$\sigma_m = B \cdot \sum_{r_1}^{r_2} N(r)^2 \tag{8}$$

where B is a constant of proportionality chosen so that $10\log_{10} B$ can be equated exactly to the quantity RL–SL and the summation limits chosen to cover the range interval where the signals are significantly above the noise level. The overall calibration coefficient, B, encompasses the electrical and acoustic characteristics of the entire sonar system. By substituting this definition of measured backscatter cross section, converted to dB, into (1) in place of the terms RL–SL, and dropping the insonified volume term, the experimental calculation of the calibration coefficient becomes

$$10\log_{10} B = 10\log_{10}\sigma - 2TL - 10\log_{10}\left[\sum_{r_1}^{r_2} N(r)^2\right]. \tag{9}$$

III. CALIBRATION SYSTEM

The calibration apparatus consists of a 4 × 4 m aluminum frame that is mounted horizontally approximately 0.5 m above the high water level from a concrete pier at the Institute of Ocean Sciences, BC, Canada. A solid cross beam on which a small sled can be moved back and forth is mounted on top of the square frame (Fig. 4). There are two stepper motors which can precisely move the sled in both x (along the pier) and y (orthogonally to the pier) directions under computer control. The position of the sled with time is recorded for later comparison with the acoustic data. The acoustic platform to be calibrated is placed on the sea-bed in the center of the frame using a crane. Water depth is approximately 9 m, depending on tide.

Separate runs were made using three tungsten carbide spheres with diameters of 38.1, 40.0, and 43.0 mm. Each sphere was enmeshed in fine seine woven of monofilament nylon. To support the sphere, monofilament fishing lines were tied to the ends of a 15 × 15 cm horizontal cross bracket to minimize any sphere motion relative to the sled. This cross bracket is connected to the sled with a 2 m long rod, which can slide vertically so that the cross bracket is supported near the surface with the sphere suspended approximately 1.2 m beneath the surface. It is important to make sure that the sphere is well below the ocean surface at the lowest stage of the tidal cycle during the particular calibration run. The spheres and seines were kept in a solution of ordinary household detergent and fresh water for at least 30 min prior to use. There was no direct handling of the spheres after this to ensure that the surfaces were fully wetted. The acoustic platform under calibration was operated exactly as if deployed for open ocean measurements. The horizontal speed of the sled in the x-direction and the step size in the y-direction were adjusted so

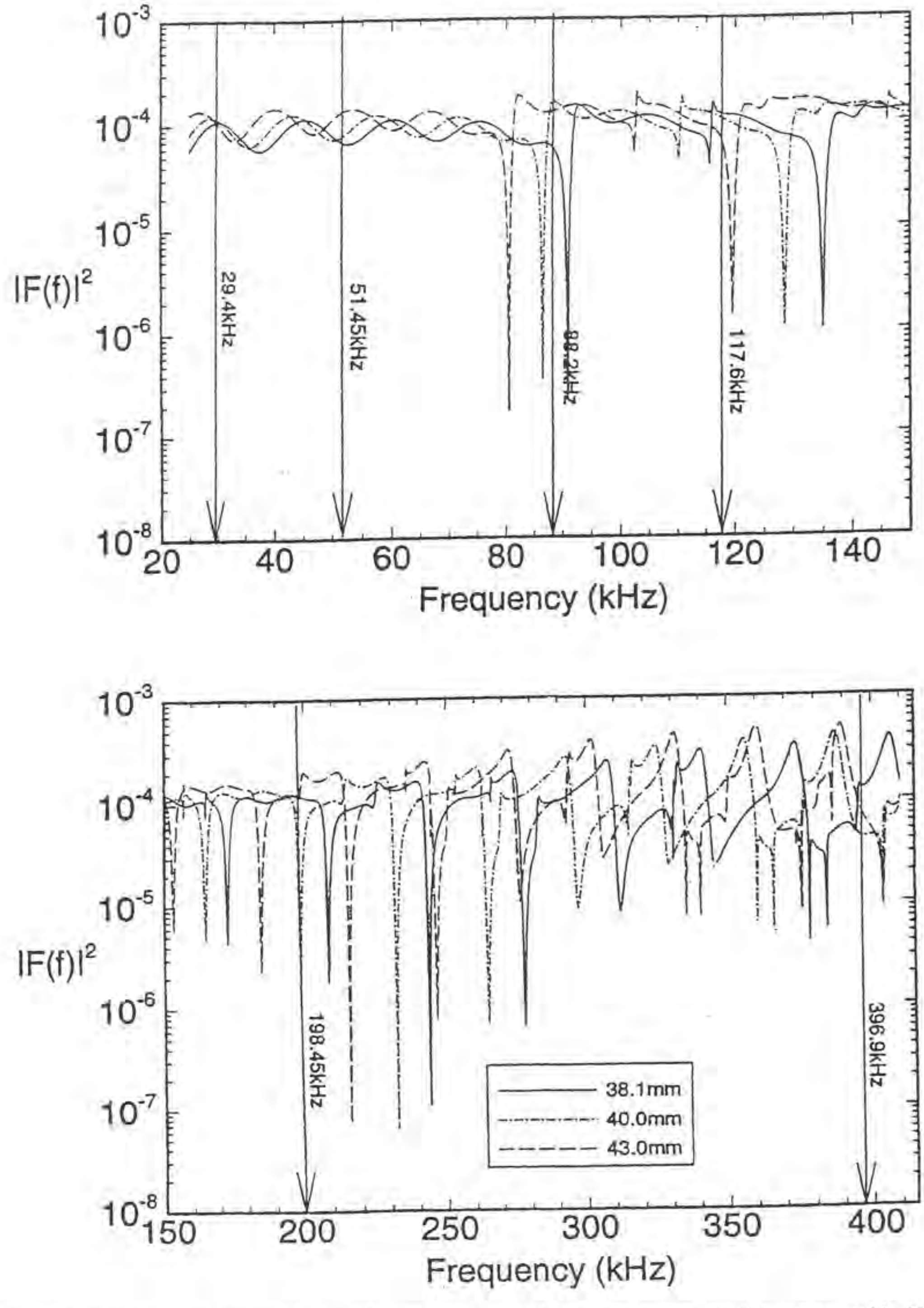

Fig. 3. Monochromatic far-field backscatter cross section as a function of frequency for the three tungsten carbide spheres used in this study. The center frequencies of the six calibrated sonar systems are indicated with vertical arrows.

that each run could be completed in less than 2 h with adequate spatial resolution. This implies a horizontal sphere x-direction speed of approximately 3 cm/s.

IV. APPLICATION

In order to illustrate the technique we describe the calibration of a multifrequency acoustics platform designed to operate as a self-contained unit while freely drifting in the open ocean. The instrument supports six echo sounders at center frequencies of 29.4, 51.45, 88.2, 117.6, 198.45, and 396.9 kHz (Table II). This frequency range is well suited for studies of macro-zooplankton, fish and bubbles. From sensitivity analysis, as discussed in Section II, it is possible to determine the best sphere to use for any particular sonar system (see Fig. 3). Hence, the preferred sphere diameters for the present sonars are: 29.4 kHz: all; 51.45 kHz: 38.1 and 43 mm; 88.2 kHz: 43 mm; 117.6 kHz: 38.1 mm; 198.45 kHz: 38.1 mm; and 396.9 kHz: 38.1 and 40 mm.

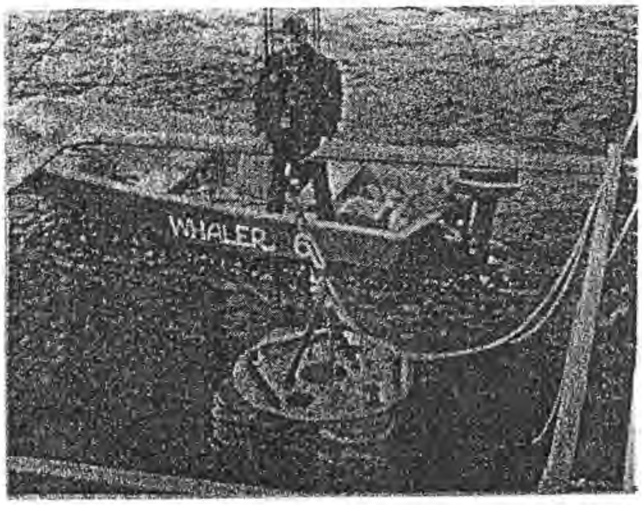

Fig. 4. Photograph showing the 4 × 4 m calibration rig mounted on the pier. The x-direction goes from left-to-right along the pier (at right in the figure) and the y-direction is positive away from the pier. The motor assembly can be seen in the *home* position (lower right corner). A sonar system is being lowered into the center of the frame for calibration.

The minimum range to ensure far-field operation for these circular piston transducers, given by the relation [6] $\pi \cdot (\text{radius})^2/\lambda$ where λ is the acoustic wavelength, ranged from 0.74 to 4.0 m. In the calibrations to follow, a minimum operating range to the calibration spheres of at least 4.5 m was maintained.

On this instrument the sonars point vertically upwards and are mounted flush with the top of a square aluminum plate (width = 1.2 m). The instrument is 1.8 m tall and is typically deployed at depths of 20 to 35 m below the mean sea surface. The pulse repetition period is 0.6 s, with pulse duration of either 410 μs, or 540 μs for the 29 kHz sonar (the longer pulse is necessary to stay within the finite bandwidth of the 29 kHz sonar).

The transmit voltages are carefully regulated to maintain transmit power regardless of battery voltage during a deployment. The backscattered echo signals from the six sonars are filtered, amplified, mixed down to a carrier frequency of 3750 Hz, and digitized at a rate of 14 700 Hz with 16-b resolution. The digital data stream is then video modulated and stored on video cassette tapes. For more information about this instrument platform see Trevorrow and Teichrob [19].

1) Calibration Results: During a typical 2-h calibration run, received signals from roughly 10 000 acoustic transmissions are recorded. From each of these records, 300 digital amplitude values spanning ranges from 0.13 m to 13 m from the transducer faces are logged onto a personal computer for further processing. Based on these data, accurate range and backscattered intensity signals are to be determined as functions of horizontal position in the far-field beams of the six transducers. These data are subsequently used to calculate the transducer beam patterns, hence the insonified volumes, and the conversion between recorded values and the backscattering cross section of any target in the beams [as in (10)].

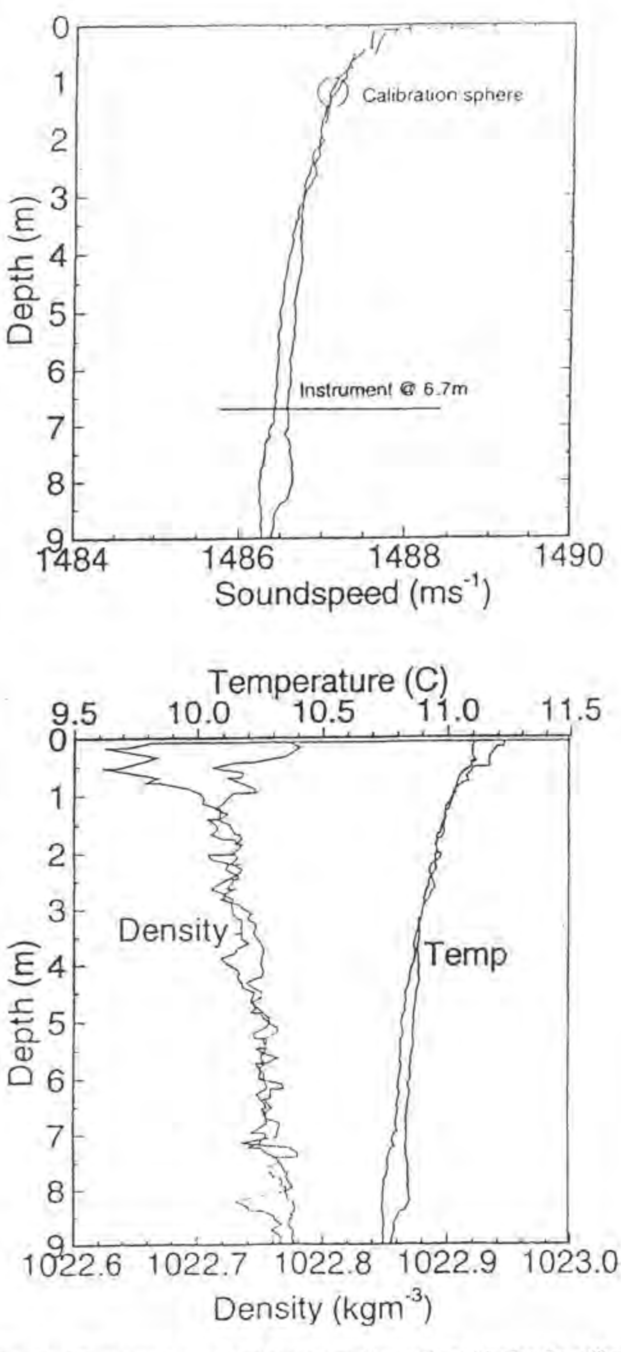

Fig. 5. Water sound speed and density profiles collected during the calibration runs. The top of the instrument was located near 6.7 m, with spheres located near 1.2-m depth, depending on tide. Measured temperatures and soundspeeds are used to calculate the calibration sphere target strength.

2) Range from Transducers to Calibration Sphere: The most accurate way of determining the range from the transducers to the target sphere would have been to make direct measurements of the distance. This approach is rather difficult in practice. Therefore, the range is obtained indirectly by measuring the time delay. The sound speed was computed from CTD profiles according to Mackenzie's relation [15]. Fig. 5 shows two sound speed and density profiles taken at the beginning of the first calibration run (38.1-mm sphere) and after the last run (43.0 mm sphere). The water column was weakly stratified, with average sound speeds varying between 1486.8 m/s at the position of the calibration sphere to 1486.4 m/s at the approximate depth of the transducers. For the present calculations we assume a mean sound speed of 1486.5 m/s. The range to the sphere is determined as the position where the signal first rises above the noise level, e.g., for the 38.1 mm sphere, at a time delay of 7.68 ms that corresponds to a range of 6.70 m. As previously explained, the width of the echoes are related in a complicated fashion to the transmit pulse duration, frequency, and characteristics of the calibration sphere itself.

3) Transducer Beam Patterns: The acoustical amplitude data together with the sphere position data recorded on the calibration

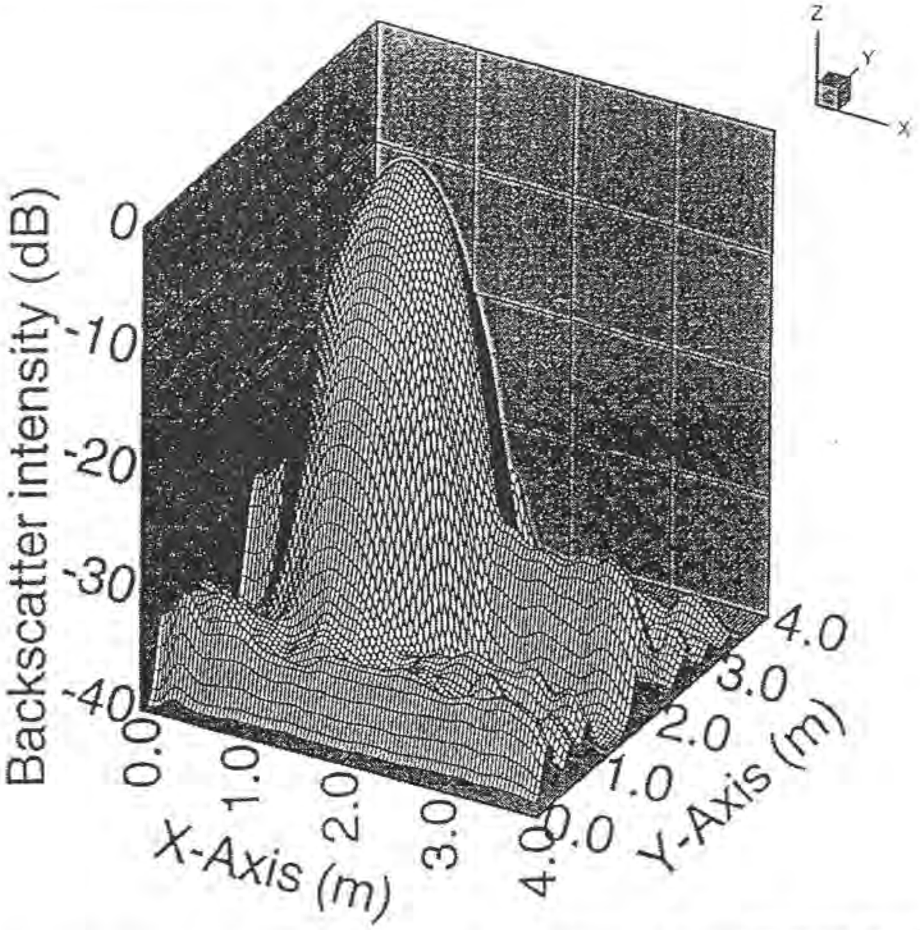

Fig. 6. Surface plot of the backscattered intensity at each acoustic transmission plotted versus x and y directions for the 117.6-kHz sonar using the 38.1-mm tungsten carbide target sphere.

control computer make it possible to allocate a horizontal (x, y) position to each backscatter amplitude value. Fig. 6 shows an example surface plot of the maximum backscatter intensity from each transmission versus x and y for the 117.6 kHz sonar using the 38.1-mm calibration sphere. The global peak of this surface represents the position of the maximum backscatter amplitude within each sonar beam. By using this peak position as an origin one can either perform direct integration to obtain the equivalent solid angle of the beam pattern Φ, or make cuts in the x and y planes to obtain the directional response of the transducer, typically summarized using the -3-dB angular width. The beam angle θ is related to the horizontal coordinates via $\theta_x = \tan^{-1}((x - x_0)/r)$ and $\theta_y = \tan^{-1}((y - y_0)/r)$ where (x_0, y_0) represent the peak position coordinates and r is the range from the transducer to the sphere. The beam patterns were found to be symmetrical around a central axis perpendicular to the transducer face. This can be seen better in Fig. 7, which shows nearly identical x- and y-direction transects through the beam patterns for this 117.6 kHz transducer shown in Fig. 6. The measured -3-dB beam widths and integrated solid angles extracted from intensity surfaces are listed in Table III.

Also listed in Table III are the idealized -3-dB beamwidths, which are calculated assuming a beam response, $D(\theta)$, for a circular piston transducer of the form [6]

$$D(\theta) = \frac{2J_1(ka \sin \theta)}{ka \sin \theta} \tag{10}$$

where k is the acoustic wavenumber, a is the transducer radius, and $J_1(\cdot)$ is the first-order Bessel function. Overall, the beam pattern results summarized in Table III show that there is basic agreement among the three different sphere runs, and between the measured and idealized beam-widths. For the 198- and 397-kHz transducers (which had very narrow beams), the measured widths are slightly larger than the ideal values, due in part to measurement error caused by the small size of the -3-dB beamwidth at these close ranges (i.e., for a 2.0° beam at 5-m range, the beamwidth has radius of 9 cm).

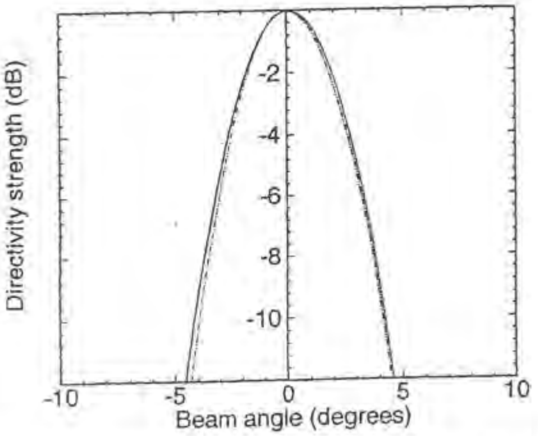

Fig. 7. Directivity strength (dB) in x(solid line) and y(broken line)-direction transects as a function of beam angle, θ, for the 117.6 kHz sonar using the 38.1-mm tungsten carbide calibration sphere.

TABLE III
MEASURED AND IDEAL −3dB BEAM ANGLES AND INTEGRATED SOLID ANGLE, Φ, FROM THE EXAMPLE CALIBRATIONS

Sonar (kHz)	Measured -3 dB beam-width	Ideal -3 dB beam-width	Φ (Steradians)
38.1 mm sphere			
29.40	10.9°	10.3°	0.0284
51.45	10.3°	10.2°	0.0254
88.20	9.1°	8.2°	0.0198
117.60	4.7°	4.0°	0.00528
198.45	3.5°	2.4°	0.00293
396.90	2.2°	2.0°	0.00116
40.0 mm sphere			
29.40	10.6°	10.3°	0.0269
51.45	9.9°	10.2°	0.0234
88.20	8.7°	8.2°	0.0181
117.60	4.6°	4.0°	0.00506
198.45	3.3°	2.4°	0.00261
396.90	2.1°	2.0°	0.00106
43.0 mm sphere			
29.40	10.6°	10.3°	0.0270
51.45	10.6°	10.2°	0.0269
88.20	8.9°	8.2°	0.0189
117.60	5.1°	4.0°	0.00622
198.45	4.1°	2.4°	0.00402
396.90	2.8°	2.0°	0.00188

TABLE IV
CALIBRATION VALUES FOR EXAMPLE MULTIFREQUENCY SONAR SYSTEM

Sonar (kHz)	Range, r (m)	$10\log\left[\frac{\sigma}{4\pi r_0^2}\right]$ (dB)	$2\,TL$ (dB)	$10\log\left[\int_{r_1}^{r_2} N^2 dr\right]$ (dB)	$10\log H$ (dB)
38.1 mm sphere					
29.40	5.80	-28.91	30.61	73.79	-133.3*
51.45	5.80	-30.71	30.72	68.68	-130.1*
88.20	5.80	-32.40	30.90	69.01	-132.3
117.60	5.80	-28.46	30.99	86.12	-145.6*
198.45	5.80	-28.45	31.19	84.07	-143.7*
396.90	5.80	-27.18	31.66	80.74	-139.6*
40.0 mm sphere					
29.40	5.90	-28.45	30.90	74.99	-134.3*
51.45	5.90	-29.43	31.02	69.10	-129.6
88.20	5.90	-28.33	31.20	71.50	-131.0
117.60	5.90	-29.27	31.29	85.79	-146.3
198.45	5.90	-33.35	31.49	78.06	-142.9
396.90	5.90	-32.72	31.98	73.65	-138.4*
43.0 mm sphere					
29.40	4.70	-28.47	26.94	78.93	-134.3*
51.45	4.70	-27.66	27.03	73.48	-128.2*
88.20	4.70	-27.48	27.18	76.81	-131.5*
117.60	4.70	-30.92	27.25	85.82	-144.0
198.45	4.70	-27.82	27.41	85.54	-140.8
396.90	4.70	-30.77	27.80	82.55	-141.1

Asterisks indicate preferred sphere diameter at that particular frequency.

V. DISCUSSION

The target strength calibration results for the example sonar system, using three different calibration spheres, are summarized in Table IV. In general the results from the three different sphere runs for each sonar channel agree to within 1 to 2 dB, when results from spheres considered suboptimal are discounted. For example, with the 397.6 kHz sonar, the 38.1-mm and 40-mm sphere results differ by 1.0 dB, while the 43-mm sphere result (which was considered unreliable) is 2.7 dB lower than the 40-mm result. The three results at 29.4 kHz, which do not encompass any resonant drop-outs (Fig. 3), all agree to within 1 dB. However, the data from the 51.45-kHz sonar, which is also without resonant drop-outs, show discrepancies as large as 1.9 dB suggesting stability problems or drifts within the electronics or perhaps the transducer itself for this channel. Surprisingly, some results for unreliable sphere sizes were very good; e.g., the 38.1-mm and 40-mm spheres at 88-kHz agree reasonably with the 43-mm sphere result, indicating that the frequency integration method outlined in (4) successfully handles the resonant behavior in this frequency range. Finally, to extract final values of the calibration coefficients for each sonar channel, results can be averaged among reliable sphere sizes.

On occasions some mobile acoustic scatterers entered the insonified volume close to the calibration sphere and partially contaminated the results, such that the calibration run had to be repeated. Visually this contamination was attributed to a school of small fish. Fortunately, periods could be found when the water was free from these unwanted scatterers. If this calibration technique is to be used on a more regular basis it might be desirable to surround the calibration rig by a fine-meshed net.

The particular choice of sphere sizes used in this study has been determined at least in part by considerations of expediency. In fact, a measure of optimization could be achieved by computing target strengths over a range of sphere sizes for each of the echo sounders, and choosing a small set of sizes for which the target strengths are relatively insensitive to the several parameters of variation, for example, medium sound speed and temperature changes, and uncertainties in physical parameters of the sphere material. In such a design, the flatter areas of the form function, plotted in Fig. 6, would be sought. A nondimensional representation, such as that in [14], is observed to be very useful.

REFERENCES

[1] S. Vagle and D. M. Farmer, "The measurement of bubble size distributions by acoustical backscatter," *J. Atmos. Oceanic Technol.*, vol. 49, pp. 630–644, 1992.

[2] J. M. Napp, P. B. Ortner, R. E. Pieper, and D. V. Holliday, "Biovolume-size spectra of epipelagic zooplankton using a multi-frequency acoustic profiling system (MAPS)," *Deep-Sea Res.*, vol. 40, pp. 445–459, 1993.

[3] Y. Miyanohana, K. Ishii, and M. Furusawa, "Spheres to calibrate echo sounders at any frequency," *Nippon Suisan Gakkaishi*, vol. 59, pp. 933–942, 1993.

[4] K. G. Foote, H. P. Knudsen, G. Vestnes, D. N. MacLennan, and E. J. Simmonds, "Calibration of acoustic instruments for fish density estimation: a practical guide," *Coop. Res. Rep. Const. Int. Explor. Mer*, vol. 144, 69 pp., 1987.

[5] R. Patterson, "Using the ocean surface as a reflector for a self-reciprocity calibration of a transducer," *J. Acoust. Soc. Amer.*, vol. 42, pp. 653–655, 1967.

[6] R. J. Urick, *Principles of underwater sound*, second ed. New York: McGraw-Hill, 1975.

[7] E. J. Simmonds, "Frequency dependence of herring and cod target strengths," *ICES C.M. 1986/B*, vol. 6, 1986.

[8] E. J. Simmonds and P. J. Copeland, "A wide band constant beam width echo sounder for fish abundance estimation," in *Proc. Inst. Acoustics*, vol. 8, 1986, pt. 3, pp. 173–180.

[9] K. G. Foote, "Spheres for calibrating an eleven-frequency acoustic measurement system," *J. Const. Int. Explor. Mer*, vol. 46, pp. 284–286, 1990.

[10] K. G. Foote, "Optimizing copper spheres for precision calibration of hydroacoustic equipment," *J. Acoust. Soc. Amer.*, vol. 71, pp. 742–747, 1982.

[11] K. G. Foote and D. N. MacLennan, "Comparison of copper and tungsten carbide calibration spheres," *J. Acoust. Soc. Amer.*, vol. 75, pp. 612–616, 1984.

[12] W. G. Neubauer, R. H. Vogt, and L. R. Dragonette, "Acoustic reflection from elastic spheres. I. Steady-state signals," *J. Acoust. Soc. Amer.*, vol. 55, pp. 1123–1129, 1974.

[13] L. R. Dragonette, S. K. Numrich, and L. J. Frank, "Calibration technique for acoustic scattering measurements," *J. Acoust. Soc. Amer.*, vol. 69, pp. 1186–1189, 1981.

[14] L. R. Dragonette, R. H. Vogt, L. Flax, and W. G. Neubauer, "Acoustic reflection from elastic spheres and rigid spheres and spheroids. II. Transient analysis," *J. Acoust. Soc. Amer.*, vol. 55, pp. 1130–1137, 1974.

[15] K. V. Mackenzie, "Nine-term equation for sound speed in the oceans," *J. Acoust. Soc. Amer.*, vol. 70, pp. 807–812, 1981.

[16] R. Hickling, "Analysis of echoes from a solid elastic sphere in water," *J. Acoust. Soc. Amer.*, vol. 34, pp. 1582–1592, 1962.

[17] T. Hasegawa, Y. Hino, A. Annou, H. Noda, M. Kato, and N. Inoue, "Acoustic radiation pressure acting on spherical and cylindrical shells," *J. Acoust. Soc. Amer.*, vol. 93, pp. 154–161, 1993.

[18] R. E. Francois and G. R. Garrison, "Sound absorption based on ocean measurements, part II: Boric acid contribution and equation for total absorption," *J. Acoust. Soc. Amer.*, vol. 72, pp. 1879–1890, 1982.

[19] M. V. Trevorrow and R. Teichrob, "Self-contained acoustics platforms for probing ocean surface processes," *IEEE J. Oceanic Eng.*, vol. 19, pp. 483–492, 1994.

Acoustic detection and quantification of benthic egg beds of the squid *Loligo opalescens* in Monterey Bay, California

Kenneth G. Foote
Woods Hole Oceanographic Institution, Woods Hole, Massachusetts 02543

Roger T. Hanlon
Marine Biological Laboratory, Woods Hole, Massachusetts 02543

Pat J. Iampietro and Rikk G. Kvitek
California State University Monterey Bay, Seaside, California 93955

(Received 12 May 2005; revised 13 October 2005; accepted 15 November 2005)

The squid *Loligo opalescens* is a key species in the nearshore pelagic community of California, supporting the most valuable state marine fishery, yet the stock biomass is unknown. In southern Monterey Bay, extensive beds occur on a flat, sandy bottom, water depths 20–60 m, thus sidescan sonar is a *prima-facie* candidate for use in rapid, synoptic, and noninvasive surveying. The present study describes development of an acoustic method to detect, identify, and quantify squid egg beds by means of high-frequency sidescan-sonar imagery. Verification of the method has been undertaken with a video camera carried on a remotely operated vehicle. It has been established that sidescan sonar images can be used to predict the presence or absence of squid egg beds. The lower size limit of detectability of an isolated egg bed is about 0.5 m with a 400-kHz sidescan sonar used with a 50-m range when towed at 3 knots. It is possible to estimate the abundance of eggs in a region of interest by computing the cumulative area covered by the egg beds according to the sidescan sonar image. In a selected quadrat one arc second on each side, the estimated number of eggs was 36.5 million. [DOI: 10.1121/1.2149840]

PACS number(s): 43.30.Gv, 43.30.Sf, 43.30.Xm, 43.80.Jz [WMC] Pages: 844–856

I. INTRODUCTION

A. Ecological and economic importance of *Loligo opalescens*

Squids, which are cephalopod mollusks, are key players in many marine ecosystems, both as predator and prey.[1] *Loligo opalescens* is a major prey species in the central and southern California coastal ecosystem. In Monterey Bay, juvenile and adult squids of this species are important food items in the diets of 19 fish, nine bird, and two marine mammal species.[2] According to this enumeration, *Loligo opalescens* has the greatest number of predator species in the particular nearshore pelagic ecosystem.

Loligo opalescens supports the most valuable marine fishery in California. This fishery is 140 years old,[3,4] has quadrupled in the past decade, and is estimated to be at maximum exploitation, yet no fishery management plan has existed until autumn 2004.[5,6] The management plan is based largely on an "egg escapement model,"[7] and thus it might be useful to learn the extent of actual egg laying in any given season or year. Most loliginid squids, such as *Loligo opalescens*[3] and *Loligo vulgaris reynaudii*,[8] are among the very few marine species that deposit their gelatinous egg capsules in mops directly on the substrate, thus rendering their spatial distribution immediately accessible to direct measurement.

Timely, synoptic data on the spatial distribution and abundance of *Loligo opalescens* in Monterey Bay are of particular interest both for management and for understanding the ecology, including that of the larger Monterey Bay National Marine Sanctuary. Given accessibility of the squid, acoustics would appear to be a useful tool for such work.

B. Overview of acoustic methods to quantify squid

Traditionally, several direct and indirect methods have been employed to assess squid stocks. These methods include, for example, those based on catch-per-unit effort (CPUE) and swept area of bottom trawl, with various applications to *Loligo pealeii*,[9] *Loligo forbesi*,[10] and *Loligo gahi*.[11] Known difficulties in assessing demersal fish by bottom trawl[12,13] also apply to squid. Use of pelagic trawl or plankton net is also difficult, as when surveying cephalopod larvae, including *Loligo opalescens* larvae,[14] to achieve adequate areal coverage. Some aspects of fishery dynamics have been measured remotely to yield a proxy for fishing effort, thence enabling abundance to be assessed indirectly through a landings-per-unit-of-effort (LPUE) measure.[15] The method of biomass estimation by enumerating squid beaks in the stomachs of predators is known to be problematical.[16] For *Loligo opalescens*, egg and larval surveys have not succeeded.[17] The potential of camera-based surveys has been recognized, but principally for quantification of benthic eggs rather than swimming animals that may avoid lights.[17] Other, generic difficulties apply, including that of efficiency when having to survey a rather large area with an instrument dependent on underwater visibility. Advantages of the direct acoustic surveying method for general fisheries applications are thus appreciated: they are rapid, remote, noninvasive, synoptic, and quantifiable.[13,18] General disadvantages of acoustic methods are associated with detection, identification, and knowing the applicable characteristic scattering properties of individual organisms in order to be able to reduce acoustic measures of organism density to biological measures of concentration density. Specific disadvantages for squid according to Thorne and Starr[19] are those of near-bottom detection, identification without having recourse to other means, and quantification in the presence of avoidance behavior or in the case of dense schools causing extinction.

The feasibility of estimating squid stock abundance by acoustic means has been established in a number of studies, including demonstrations through sea trials. Examples are *Loligo gahi* and *Martialia hyadesi* on the Falkland Shelf in the South Atlantic[20] and *Loligo vulgaris reynaudii* off the south coast of South Africa.[21] Acoustic data were derived from echo sounders with vertically oriented beams at 38 and 120 kHz for the first two species and at 38 kHz for the third species. In recent years, the abundance of *Todarodes pacificus* on the major fishing ground off northern Honshu, Japan, has been estimated at 38 kHz by the echo integration method (Ref. 22 and A. Kawabata, pers. comm.). Acoustic trials are also being performed on the same species around Hokkaido, Japan, and on *Loligo edulis* in the East China Sea (A. Kawabata pers. comm.).

The acoustic detectability of *Loligo opalescens* aggregations in the water column was established by Vaughan and Recksiek[23,24] in Monterey Bay. Several distinctive echo types were observed at 38, 50, 75, and 200 kHz. These were associated with proximity to the bottom and time of day.

Loligo opalescens has also been observed acoustically off the central Oregon coast by Jefferts *et al.*[25] This was quantified by means of integration of echo sounder data at 120 kHz. In addition, the target strengths of resolved individual squid were measured directly by means of the dual-beam function of the same echo sounder.[26]

C. Biology of *Loligo opalescens*

Loligo opalescens is very fast-growing, short-lived, and highly mobile, as described in, for example, Refs. 3 and 27–30. Little is known in detail about its whereabouts for much of its life history. The exceptions are the end points defined by spawning. Near the end of its 6–12 month life span, *Loligo opalescens* migrates inshore and spawns, laying eggs in capsules on the shallow coastal seafloor. After about one month, paralarvae, which are morphologically similar to the adult, emerge from the capsules to enter the plankton stage; their movements are generally unknown.[31] Those individuals that survive predation and other forms of mortality return as adults to spawn. Significantly for acoustic investigations, the egg laying seems to occur mainly on flat sandy bottoms in depths of 20–60 m.[31–37]

The eggs are laid in gelatinous capsules containing 100–200 eggs, each in its own Voronoi-like cell[38] called a chorion. Initially, the capsules are cylindrical in form, *ca.* 16 mm in diameter and about 9–10 cm long, expanding to 20–25 cm after a few days.[39] The female cements each capsule in the sand, and they stand vertically, bending and swaying under the influence of currents. The presence of egg capsules attracts other spawning squid, which tend to deposit their egg capsules contiguously with existing capsules. In this way, benthic *egg mops* of diameter 20–100 cm and *egg beds* of diameter greater than 1 m are formed (Fig. 1). For simplicity, these are often referred to generically as egg beds. These can become massive, reaching 12 m in extent,[39] and may even consist of multiple tiers rising 40–60 cm off the sea floor or, as reported anecdotally in Ref. 3, in a pillar 1.5-m high. Hatching occurs about one month after egg-laying, depending upon temperature.[28] The period of peak spawning in Monterey Bay is thought to coincide with peak fishery catches during April–May. Squids continue to be fished through the summer, with a secondary capture peak in September–October.[6] Eggs are present throughout this period. One record exists of the presence and absence of eggs following an El Nino event;[40] however, no maps are published of egg distribution or abundance, either yearly or seasonal.

The primary spawning grounds of *Loligo opalescens* in central California are located in the southern part of Monterey Bay over an area that is about 10 km^2. This is small compared to the larger habitat, but is still large for detailed surveying. Currently, the State of California closes

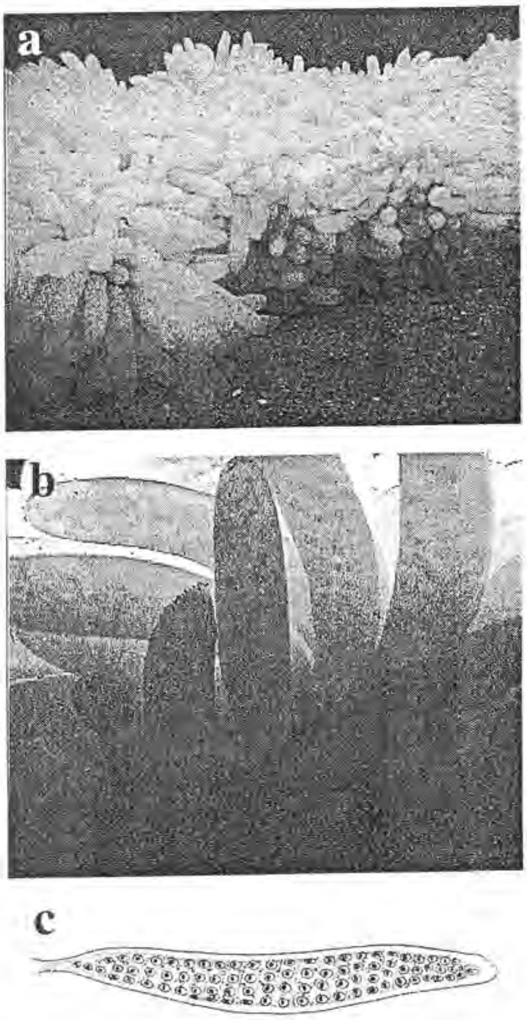

FIG. 1. Egg bed of the squid *Loligo opalescens*. (a) Section of egg bed. (b) Detailed view. Individual chorions can be seen. (c) Sketch of egg capsule [redrawn from C. F. E. Roper, Bull. Mar. Sci. **15**, 589–598 (1965)].

squid fishing two days per week,[35] but no benthic habitat for squid egg beds is protected. Successful annual recruitment is required to sustain squid populations.[41] If fishing pressure continues to increase, it may be prudent to restrict fishing directly over the largest egg beds to allow the normal progression of sexual selection and egg-laying behaviors.[34,37]

D. Acoustic technology

The unique loliginid habit of laying massive benthic egg beds can be exploited in surveying egg beds and thus using egg capsule production as a proxy for reproductive success. Certainly the advantages of surveying a stationary resource and performing analyses based on spatial information are both prominent and tempting in choosing a method. To meet the requirements of resolution and detectable backscatter, it would seem that a sonar with a very directional beam and rather low grazing angle relative to the bottom would be most effective; this defines a towed, high-frequency sidescan sonar.[42,43]

E. Outline of this paper

The plan of this work is to describe development of an acoustic method to detect, identify, and quantify egg beds of *Loligo opalescens*. In the following, preliminary investigations on squid egg capsules and beds are summarized. The design of an experiment to verify the acoustic method is elaborated. Details are given on the instrumentation, equipment, platforms, and methods. Video and acoustic images of the same regions of interest are included in the results. The abundance of eggs is estimated in a quadrat that is one arc-second on each side. Outstanding problems connected with acoustic resolution, use of alternate platforms, automated recognition of egg-bed echoes, squid biology, monitoring of squid spawning grounds, and acoustic properties of egg capsules are discussed.

II. PRELIMINARY ACOUSTIC OBSERVATIONS OF SQUID EGG BEDS

Acoustic detectability of egg capsules of *Loligo pealeii* was established at the Marine Resources Center, Marine Biological Laboratory, by two of the authors (KF and RH), together with J. Condiotty and C. Gubala in June 2002. Egg capsules freshly laid by the squid in a mop on the bottom of a tank, water depth 80 cm, were observed with the Simrad EY500/710-kHz echo sounder, with transducer floating on the water surface, using a short-duration pulse. *Loligo pealeii*, like *Loligo opalescens*, attaches its egg capsules to the bottom substrate, preferring to abut previously laid capsules. Relative to the echo from the bottom of the tank, the echo from the capsules arrived earlier by a time corresponding to the height of the capsules, 8 cm. Despite the particular *ex situ* conditions, this measurement gave tangible proof that egg capsules of squid could be detected acoustically.

In a study by Sauer *et al.*,[44] some evidence was presented for the acoustic identification of *Loligo vulgaris reynaudii* egg beds *in situ*. A commercial fisheries echo sounder, with operating frequency of 200 kHz, was used. While the identification probability was very high under the circumstances, it is not clear that the significant part of the echo was due to the egg beds themselves and not to bottom morphological features or spawning squid in the vicinity of the egg beds.

The initial acoustic investigation in the field was conducted in May 2003 in Monterey Bay. A 400-kHz sidescan sonar was towed from the California Department of Fish and Game (CDFG) research vessel Mako. Within minutes of commencing the first sidescan sonar transect off Del Monte Beach, with bottom depth of 20–30 m, a distinct dapple or mottling was observed on the sidescan sonar echo record. The size, shape, and proximity of the small features were reminiscent of squid egg beds that SCUBA divers in the scientific party had earlier observed.

Because of the proximity of the beach and exposure of the site to the open ocean, a second site was visited, just north of the breakwater and several hundred meters off Cannery Row. The sidescan sonar observations were similar to those off the beach. SCUBA divers descended to confirm a large concentration of squid egg beds. Various attempts were made to establish a close correlation of the sidescan sonar recordings and squid egg beds. Navigation was a limiting factor, but the results were strongly suggestive.

Efforts to detect the squid egg beds with the Simrad EK60 scientific echo sounder,[45] the successor to the EK500 scientific echo sounder,[46] with split-beam transducer at 200 kHz, were unsuccessful. Echoes from the egg beds and bottom could not be distinguished, which is not surprising, given the pulse length 10 cm, nominal 9–10 cm height of newly laid egg capsules, bottom depth of 20–30 m, sea state, and vessel mounting of the transducer.

A second acoustic investigation in the field was performed about the Channel Islands in southern California in late February and early March 2004. A 600-kHz sidescan sonar was towed from the NOAA Channel Islands National Marine Sanctuary research vessel Shearwater. This was configured with a video camera, with downward orientation. Squid egg beds were observed simultaneously with both systems, if at different ranges. An unexpectedly strong current dragged a bottom-mounted array of acoustic reflectors including floats, out of alignment, preventing repeated observations of the reflectors and squid egg beds.

III. EXPERIMENTAL DESIGN

Based on the preceding investigations, with their suggestive findings and association of certain characteristic features on the sidescan sonar image and squid egg beds, it was decided to perform a larger-scale verification trial on the spawning grounds in Monterey Bay. The principal acoustic instrument would be a high-frequency sidescan sonar with integrated geo-referencing processing system. The major verification tools would be video cameras. One would be a drop camera, to be suspended over the side of the vessel for reconnaissance use, and the second would be ROV-borne for investigations with a relatively high degree of operator control.

Initially, a region of high concentration of egg beds had to be found. This was done by means of the drop camera over traditional spawning areas. A survey region of interest (roi) was defined. This was surveyed systematically by sidescan sonar along parallel transects, as in Refs. 47 and 48, with substantial overlapping coverage to enable a map, or mosaic, of seafloor backscattering to be assembled.

Locations with markings suggestive of squid egg beds were noted. Following the sidescan sonar survey, the same roi was surveyed by means of a ROV-borne video camera. The degree of coverage was much less, but the entire roi was sampled along a few transects. The ROV was steered to investigate previously identified areas of special interest.

Precision navigation instrumentation was used. A differential Global Positioning System (dGPS) was used to determine the positions of the sidescan sonar transducer arrays and ROV-borne video camera. An acoustic tracking system was used for precise determination of the position of the video camera relative to the vessel.

Given both sonar and video data on the roi, tests were devised to prove that characteristic sidescan sonar features could be associated unambiguously with the presence or absence of egg beds. Two tests were designed, one with the sidescan sonar data enabling predictions to be made for verification by the video-camera images, and *vice versa*. Statistics could then be employed to assign significance levels.

In addition, the sidescan sonar data provided the grist for quantification of the egg beds within a defined area. This served as an example of the feasibility of abundance estimation.

IV. MATERIALS

A. Acoustic instrumentation

1. Sidescan sonar

The principal acoustic instrument was the EdgeTech model 260-TH Image Correcting Side Scan Sonar, with model 272-TD dual-frequency analog towed vehicle, called a towfish, with time-varied gain (TVG). This was used to detect and image the squid egg beds. Two longitudinally oriented, parallel transducer arrays were mounted on each side of the towfish, with nominal operating frequencies of 100 and 500 kHz, as casually described by the manufacturer, but with the higher frequency being much closer to 400 kHz. A deck unit supplied power to the towfish, controlled this, printed the paper record, and sent the analog signal to the Isis Sonar digital acquisition system contained in the model 260-TH Image Correcting Side Scan Sonar.

Both frequencies were used. The upper frequency was in the range 390±20 kHz. The pulse duration was 0.01 ms. At 50-m range, the ping interval was 75 ms, hence the ping rate was 13/s.

The sampling frequency was 2048 16-bit pixels per channel per second, as determined by the AU-32 A/D board in the Isis acquisition system, not the sonar, which was entirely analog. The source level was 222 dB *re* 1 μPa at 1 m. The horizontal beamwidth was 0.5 deg at the -3 dB level, and the vertical beamwidth was 50-deg, tilted downward by 20 deg from the horizontal.

The lower frequency was 105±10 kHz. The pulse duration was 0.1 ms. At 50-m range, the ping interval, ping rate, and sampling frequency were the same as for the higher frequency, but the source level was 228 dB *re* 1 μPa at 1 m. The horizontal beamwidth was 1.2 deg, and the vertical beamwidth was 50 deg, tilted down 20 deg from the horizontal.

2. Fishing echo sounder

A Furuno Fish Finder, model FCV582L echo sounder, was used for general inspection of the water column and occasional detection of squid aggregations in advance of sonar or video observations of egg beds and part of the water column. The echo sounder operated at both 50 and 200 kHz, with a nominal maximum range of 750 m at the lower frequency, with 600-W output power. Echo data were converted to a video signal and displayed on a color liquid crystal display (LCD). Automatic gain control was used but not monitored.

B. Video cameras

1. Drop camera

The reconnaissance camera was suspended on a weighted line from the vessel. This was the Deep Blue Pro Color camera, which forms a National Television System Committee (NTSC) composite video image with 480 TV lines. This was a compact unit, with 3.6-mm wide-angle lens, focus fixed at 2.54 cm to infinity, sensitivity 0.3 lux, and electronic iris. Image data were transferred by cable to the vessel and stored on a JVC BR-DV600A mini-digital video camera recorder (VCR). Telemetry and other information were overlaid on the video image.

2. ROV-carried camera

The camera used in the verification exercises was that mounted inside the remotely operated vehicle (ROV): a JVC model with 470-lines resolution, 0.95–lux color charge-coupled device (CCD) and F 0.8 Pentax lens. Through its internal mounting, it could tilt and view through 360 deg. Panning of the camera was achieved by rotating the vehicle, which could turn on its own axis. Image data were transferred through the ROV tether and, as with the drop camera, recorded on an on-board JVC BR-DV600A mini-digital VCR.

C. Platforms and positioning devices

1. Research vessel MacGinitie

The principal platform was R/V MacGinitie, an aluminum hydrographic survey launch, overall length 9.6 m, draft 0.5 m, beam 2.7 m, gross weight 4.5 metric tons fully equipped, cruising speed 18–28 knots depending on conditions, electrical power 30-A 110-V ac and 12-V dc. It carried state-of-the-art sonar mapping and ROV technology like that found on large hydrographic research vessels, but in a towable configuration designed for nearshore shallow-water habitat work. It is owned and operated by the Seafloor Mapping Laboratory of California State University, Monterey Bay.

2. *Remotely operated vehicle Hyball*

A platform for the JVC video camera was the Hyball ROV, which has a 300-m depth capability and is fitted with four thrusters. Two main thrusters provide forward, reverse, and rotational movement, and two vertran thrusters provide vertical and lateral movement. This small unit was easy to deploy and retrieve and proved sufficiently maneuverable in depths up to 34 m with mild or no current.

D. Positioning systems

1. *Global Positioning System*

Research vessel MacGinitie has a differential GPS (dGPS). This is fully integrated with the PC-based Nobeltec/Sitex navigation system of the vessel, which also includes digital charting, radar, and autopilot. Data from the dGPS could be attached to the sonar and video data at the time of their collection.

2. *Trackpoint*

The Hyball ROV was tracked and its position determined by a Trackpoint II+ ultra-short baseline acoustic tracking system (ORE International, Houston, Texas). The Trackpoint system has a 0.5-m slant-range accuracy and a total horizontal position accuracy of less than 0.5% root-mean square of slant range. Depth information was provided by a pressure sensor on the vehicle as well as by a 4337B Trackpoint multibeacon with depth telemetry. The Trackpoint system was interfaced to the top-side vessel survey navigation system with dGPS and provided real-world (x,y,z)-positioning of the ROV with accuracy ±2 m by means of the Coastal Oceanographics Hypack Max software. The National Marine Electronics Association (NMEA) position data were also recorded directly on the digital video (DV) tape using a Horita GPS-3 encoder. This device recorded the position data in an audio track on the videotape, where they could be accessed without obscuring the video imagery.

V. FIELD METHODS

The field work was conducted on the traditional spawning grounds of *Loligo opalescens* in southern Monterey Bay during the period 13–16 May 2004. This work began with a reconnaissance with the drop camera to locate a region abundant in egg beds. The identified region was then surveyed systematically by sidescan sonar. It was subsequently surveyed by ROV-borne camera to verify the sidescan sonar observations.

A. Drop-camera reconnaissance

The initial drop-camera reconnaissance was performed on 13 May over a flat sandy bottom off the breakwater and in view of Cannery Row at four stations with the vessel drifting at 0.5–1 knot. The approximate depth range was 26–34 m. Small numbers of lone squids were observed scattered widely on the bottom, generally in the vicinity of eggs, but neither adults nor eggs were numerous.

The reconnaissance was continued on 14 May, drifting from north of Lovers Point to Hopkins Marine Station at the approximate speed 0.5–1 knot. The drift path followed that of a fault line, depth difference 6–7 m, dividing an otherwise flat sandy bottom within the depth range 25–40 m. The drift path was maintained near the fault line by use of the vessel motor when necessary. Sparsely and richly populated patches of squid egg beds were observed.

On both days notable features were marked. This operation generated a computer file with paired geographical positions and time codes, as well as biological annotations. The drop-camera position was assumed to be identical to that of the vessel since the camera was suspended from the drifting vessel over a rather short distance, and the line was observed to be vertical.

B. Sidescan sonar survey

The fault-line area identified by the drop-camera reconnaissance was surveyed with the sidescan sonar on 15 May (Fig. 2). Twenty parallel transects were performed at the speed 2–4 knots with the maximum range of 50 m to each side of the towed arrays. The sidescan sonar was maintained about 5–10 m over the seafloor, whose depth varied over the approximate range 25–40 m. The first 15 transects were performed at the upper frequency, about 400 kHz, and the last five at the lower frequency, about 100 kHz. The first 15 transects were performed with a track spacing of 50 m, ensuring 100% overlap in the port or starboard swath. Working conditions were characterized by a fresh onshore breeze and short, steep seas of wave amplitude 1–2 m.

C. ROV-borne video camera investigations

At the beginning of the field work on 16 May, the vessel flux-gate compass was calibrated in two exercises performed off Cannery Row. This enabled the vessel heading to be determined to within ±1 deg. The flux-gate compass was interfaced with the Trackpoint system (Sec. IV D 2), enabling the ROV position to be given in absolute rather than relative coordinates.

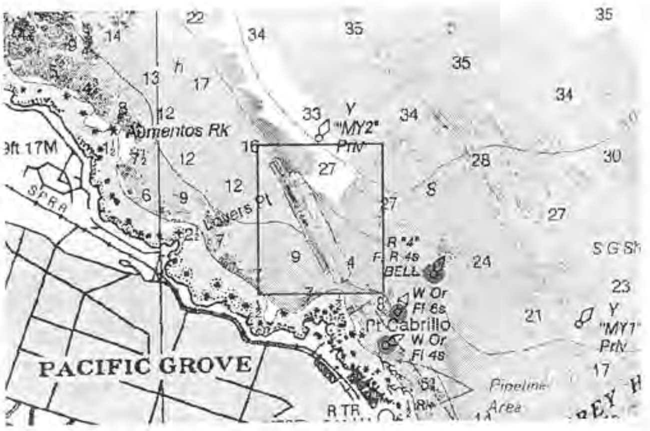

FIG. 2. Geographical region of the sidescan sonar survey off Pacific Grove in southern Monterey Bay on 15 May 2004, showing the high-frequency sidescan sonar mosaic.

The ROV was deployed with the vessel drifting or motoring gently to maintain a track parallel to the fault line. Three parallel track lines, located within the sidescan sonar survey area, were surveyed, with a nominal separation distance of 20 m. One of the track lines is shown in Fig. 3. Several large, dense aggregations of squid egg beds were circumnavigated in an attempt to map their extents, occasionally exceeding 10 m. The ROV was kept approximately 1–2 m from the bottom, with a forward/downward viewing angle of approximately 45 deg. Video from the ROV was recorded with the JVC unit on mini-digital videotape format. ROV positions were determined using a Trackpoint II+ ultra-short-baseline acoustic tracking system (ORE International, Houston, TX) and the vessel dGPS to yield real-world (x,y,z)-coordinates with ±2-m accuracy. The ROV depth was also determined by a pressure sensor mounted on the vehicle. ROV position, pressure-determined depth, and time in UTC were recorded onto the videotape using a Horita GPS-3 encoder.

Lone squids were observed in the vicinity of some egg beds. Occasional pairings and contested pairings were also observed, although the observations of spawning squid were incidental to the objective of surveying the egg beds.

VI. DATA POSTPROCESSING

Several data processing operations were undertaken in the Seafloor Mapping Laboratory immediately after completion of the cruises.

A. Postprocessing and mosaicking of sidescan sonar data

Digital processing and mosaicking of the 400-kHz sidescan sonar data were accomplished using the Isis Sonar and Delph Map software packages (Triton Elics International, Watsonville, California) and TNT Mips geographical information system (GIS) software (Microimages, Inc., Lincoln, Nebraska). Individual xtf track-line files were replayed, and bottom tracking of the sonar was supervised to aid in proper slant-range correction. Line files were snipped to remove portions with poor imagery from the beginning and/or end of the track line. Track lines were corrected for slant-range, layback, and lateral offset, and the position data for each line were smoothed using a speed filter. Each line was then gridded, geo-referenced, and exported from Isis Sonar/Delph Map in geo-referenced Tag(ged) Image File Format (GeoTIFF) (0.20-m and 0.10-m pixel size, UTM Zone 10, WGS84). Individual track-line TIFF images were imported into TNT Mips GIS software and areas of poor image quality were extracted and removed. Individual track lines were then overlaid to produce a mosaic image.

FIG. 3. First track of the ROV-borne video camera on 16 May 2004, superimposed on the sidescan sonar mosaic. The distance between the marked end points of the track is 603 m.

B. Video-data postprocessing

Video-data processing was completed using a JVC BR-DV600A mini-DV VCR with monitor display. Tapes were reviewed and positional data retrieved using the Horita GPS-3 decoder. The precise locations of squid egg bed observations were recorded in a text file, together with observational data regarding egg bed density, substrate type, and other characteristics. Information from the log sheets and text files was integrated into a database.

C. Entry of data into geographical information system (GIS)

Mosaic GeoTIFF images were exported from TNT Mips at 0.20- and 0.10-m resolutions into ArcGIS 8.3 software (ESRI, Redlands, California). An attribute table that included the parameters logged during the video-camera data analysis was also imported into the same GIS.

Use of ArcGIS enabled both the sonar data and video-camera tracks to be visualized. Individual or multiple sidescan sonar swaths could be displayed, as could video-camera tracks, at the command of the operator. In addition to simple visualization of data, GIS confers other benefits.[49] These include, for example, displaying the data at different scale sizes, expressing the cursor position in geographical coordinates, overlaying fields with a coordinate grid, measuring the distance between points, marking particular features with a polygon, among other things. Extracted images could also be exported for use outside the GIS.

VII. DATA ANALYSES

The first analysis involved presence–absence testing; the second, determination of the detection size limit; and the third, abundance estimation of squid eggs over an area.

A. Presence–absence testing

The primary goal of the testing was to prove, or verify, the association of characteristic features on the sidescan sonar images with the presence of squid egg beds, as well as the absence of squid egg beds in the absence of those same characteristic features. A secondary goal was to establish the size limit of detectability.

Test 1. By means of the ArcMap module within ArcGIS, the sidescan imagery was reviewed in fine detail by one of the co-authors (KF). Geographical areas with dapples or mottling believed characteristic of the presence of squid egg beds were identified. Areas lacking these features were also

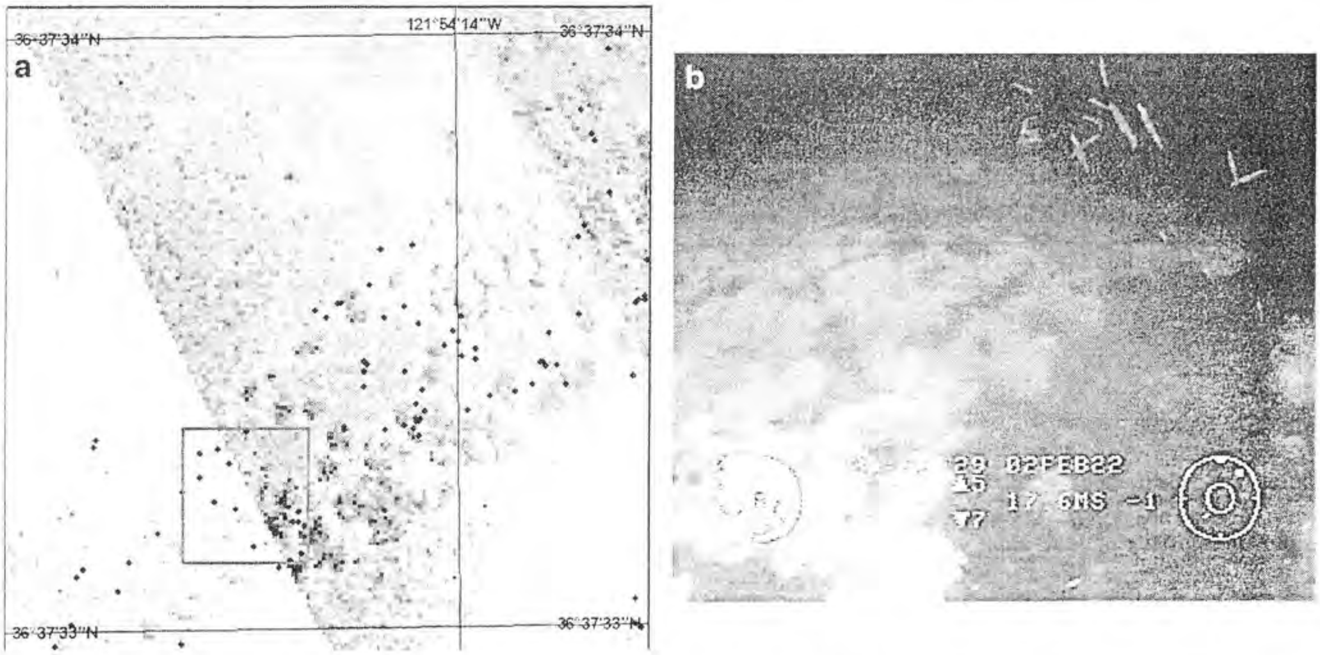

FIG. 4. Pair of images taken from the first test. Excerpt of sidescan sonar mosaic (a), with box indicating the region where the video-camera image (b) was captured. Adult squid are observed in the upper right corner of (b).

identified. A selected example of apparent egg presence is shown in Fig. 4(a). This area was also observed by the ROV-borne video camera. Time codes corresponding to the period that the ROV was inside the indicated box in Fig. 4(a) were determined. The particular time codes, together with time codes from another 29 selected regions of interest, were listed without reference to position or sidescan sonar observations to define a first test. These were used blindly by another co-author (RH) when examining the video-camera recordings to describe the presence or absence of squid egg beds. Related observations were made on the size, shape, and distribution of egg mops or beds or other benthos, e.g., kelp fronds, starfish, and sea stars, among other things.

Test 2. The process of formulating Test 1 was reversed in preparing a second blind test, which also endeavored to define the limits of detectability by sidescan sonar. An example of a video image selected for this test is shown in Fig. 5(a). The second co-author (RH) reviewed the ROV-borne video-camera tapes in detail, without reference to the sidescan sonar data, choosing a total of 30 representative regions of interest containing or lacking squid egg mops or beds. A list of the corresponding time codes was prepared without

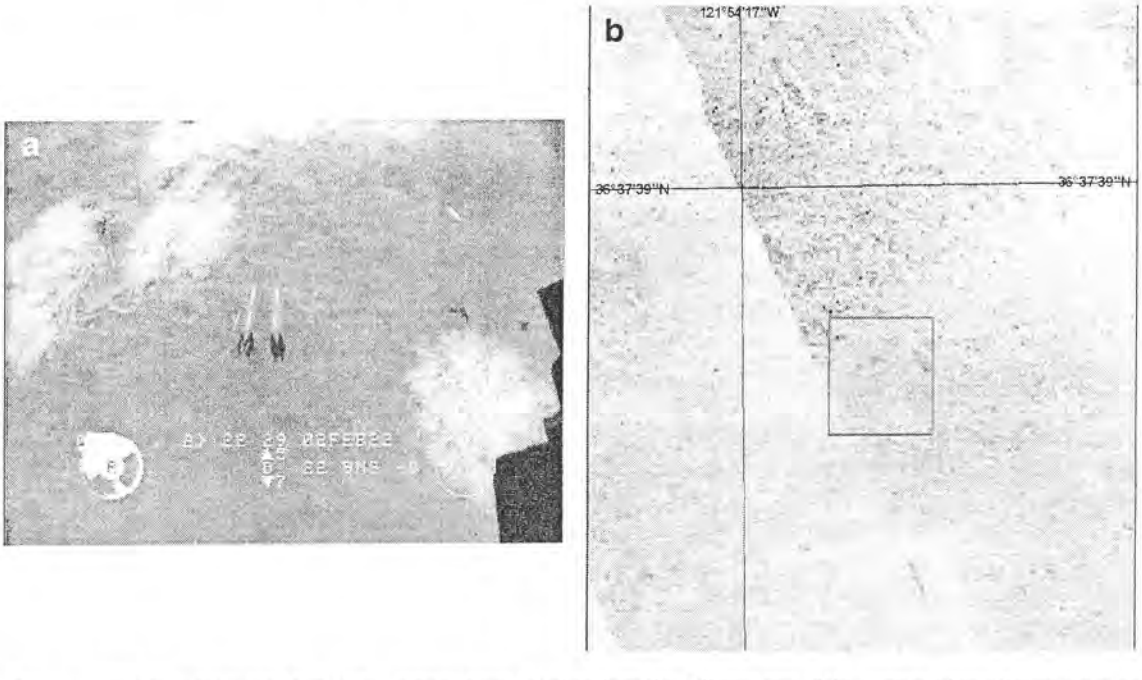

FIG. 5. Pair of images taken from the second test. Video–camera image (a) taken from the indicated area of the corresponding sidescan sonar mosaic excerpt (b). Two mating pairs and two loan squids are also visible in (a).

information on the video-based observations. The time codes were translated into geographical positions. The first coauthor (KF) then reviewed and interpreted the sidescan sonar imagery in a blind test to describe the markings as believed indicative of the presence or absence of squid egg beds.

The statistical significance of each test was gauged by means of both the binomial and Fisher exact test.[50]

B. Detection limit

The spatial resolution of the 400-kHz sidescan sonar array is about 10–20 cm over the range interval 12–23 m. Thus, there will be a lower limit to the size of egg beds that can be detected and identified. Determination of this limit was a secondary goal of the testing. Materials for the determination of the size limit were contained in the presence–absence testing. The associated video record was examined to establish the sizes of individual egg mops or beds when these were well separated from other clusters. Discrepancies in the statistical testing mentioned in the previous section were given particular attention.

C. Abundance estimation

A further analysis was performed to illustrate the quantification process. A quadrat of side length one arcsecond on each side, 30.9 m in the N–S direction and 24.8 m in the E–W direction, was defined, and the fraction of area covered by the squid egg beds was estimated. Assuming a mean diameter of egg capsules of 16 mm, based on several direct measurements, and mean number of eggs per capsule of 150, based on recent counts of eggs in sampled capsules, the total number, or abundance, of eggs in the quadrat was estimated.

VIII. RESULTS

Positions at which sidescan-sonar-based predictions of squid-egg presence or absence were subsequently, independently judged by reference to the video record are shown in Fig. 6. Agreement of the respective data is indicated by the use of open symbols; disagreement, by filled symbols.

Positions at which video observations of the presence or absence of squid eggs were subsequently, independently interpreted by the sidescan sonar images are shown in Fig. 7. As in the previous figure, agreement is indicated by open symbols and disagreement by filled symbols.

Both the binomial test and the Fisher exact test[50] were used to test the null hypothesis that the observed agreement in corresponding sonar and video images was due entirely to chance. Contingency tables are presented for the two tests in Tables I and II.

Each test involved 30 trials, each coincidentally yielding 24 positive outcomes in which the presence or absence of eggs was verified by the video record (Table I) or interpreted by the sonar imagery (Table II). The probability that 24 or more outcomes would have agreed was computed according to the binomial distribution assuming a probability of any single outcome being 0.5. The result was 0.7155×10^{-3} for each test.

The Fisher exact test was similarly applied to each set of data. The probability was computed of the distribution of outcomes shown in the respective tables together with their more extreme cases. The result for the first test (Table I) was 0.5939×10^{-4} and for the second (Table II), 0.4082×10^{-7}.

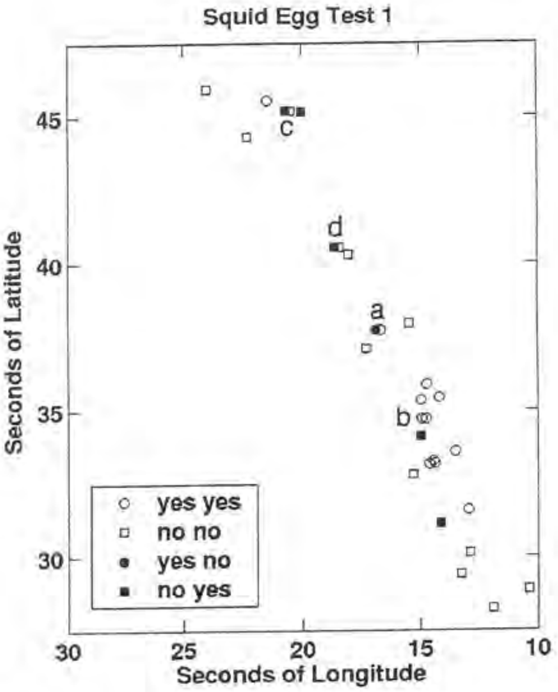

FIG. 6. Positions where sidescan-sonar-based predictions of squid-egg presence or absence were subsequently, independently judged by the video record. Agreement of the respective data is indicated by the use of open symbols; disagreement, by filled symbols.

Thus, at least at the 0.001 level, no matter which test is used, the null hypothesis can be rejected. Characteristic features on the sidescan sonar images can be associated with the presence or absence of squid egg beds.

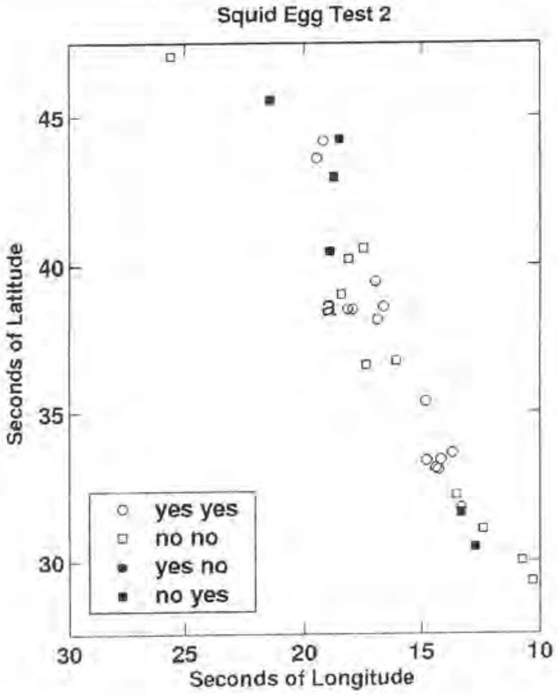

FIG. 7. Positions where video observations of squid-egg presence or absence were subsequently, independently interpreted by the sidescan sonar images. Agreement is indicated by open symbols; disagreement, by filled symbols.

TABLE I. Contingency table for Test 1, in which sidescan sonar predictions were made at selected positions, which were subsequently used to specify where to examine the video-camera record.

		Sidescan sonar		
		Presence	Absence	Sum
Video camera	Presence	12	5	17
	Absence	1	12	13
	Sum	13	17	30

A quadrat has been defined by the one-arc-second area at N 36° 37′33–34″ and W 121° 54′14–15″. The sidescan sonar image is shown in Fig. 8. The quadrat area is 764.6 m^2. The cumulative area covered by the squid egg beds according to the characteristic dapples was estimated by a graphical method as 49.0 m^2, or 6.4% of the whole. Assuming that the mean diameter of an egg capsule is 16 mm, which was measured for a limited number of retrieved capsules, the estimated number of capsules in the quadrat is 2.44×10^5. Based on an average number of eggs per capsule of 150, the estimated total number of eggs in the quadrat is 3.65×10^7.

TABLE II. Contingency table for Test 2, in which video-camera observations were made at selected positions, which were subsequently used to specify where to examine the sidescan sonar images.

		Video camera		
		Presence	Absence	Sum
Sidescan sonar	Presence	14	0	14
	Absence	6	10	16
	Sum	20	10	30

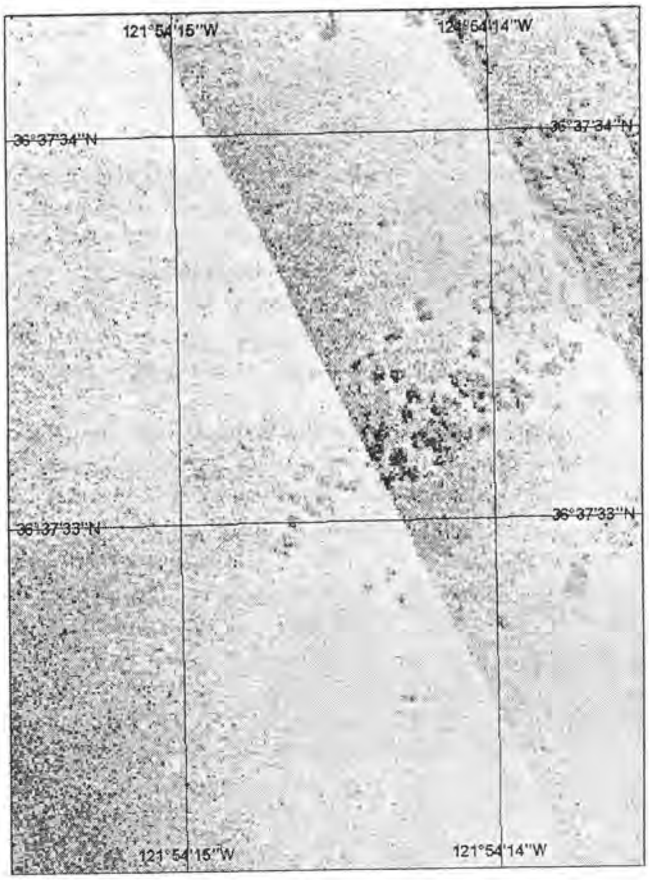

FIG. 8. Sidescan sonar image of a quadrat at N 36° 37′33–34″ and W 121° 54′14–15″ selected for estimating squid-egg abundance.

IX. DISCUSSION

A. Statistical tests

Characteristic dapple or mottling on the sidescan sonar images at 100 and 400 kHz was first associated with squid egg beds during a cruise in Monterey Bay in May 2003. Data collected one year later, which are analyzed in this work only at the higher frequency, verify the association. The visual images in Figs. 4 and 5 are clearly suggestive, but the robustness of the association has been statistically established through two blind tests.

In the first test, predictions of the presence or absence of squid egg beds were made solely on the basis of the sidescan sonar data, then tested by reference to the video camera recordings. In the second test, areas observed to contain or lack egg beds were used to specify regions of interest in the sidescan sonar images requiring interpretation. Each test was prepared by a co-author and taken by another co-author without knowing the initial sonar interpretation or video observation. The null hypothesis, that the apparent agreement of predictions or interpretations with observations was due entirely to chance, was tested by each of two tests. The null hypothesis was rejected at the 0.001 confidence level by the binomial test and the 0.0001 confidence level by the Fisher exact test.

It is illuminating to examine the failed examples in the two tests. In the first test, in which sonar images were used to specify positions for examination of the video record, there were a total of six failures. Comments made during review of the video record in Test 1 are listed for each instance of disagreement. In only one case did the sidescan sonar image indicate the presence of eggs that was not verified by the video record. In the region of pair a, eggs were not observed along the third ROV track, although their presence was confirmed by the second ROV track. This probably represents a simple miss due to the video camera being oriented in the wrong direction when passing the egg beds. In the other five cases of disagreement, the sidescan sonar images did not indicate the presence of eggs, which were subsequently observed on the video record. The following comments are arranged in order of position from north to south. (i) Two very small mops were observed along the second ROV track, but not along the first ROV track, indicated in pair c. (ii) One tiny egg mop was seen along the first ROV track at the edge of the region of interest. (iii) A few very small, widely dispersed mops were seen along the third ROV track, but not along the second ROV track, in pair d. (iv) A few large clumps, *ca.* 1–3 m, were observed along the third ROV track at the edge of the region of interest. (v) Two small patches were observed along the third ROV track. In four of the five cases here, the eggs occurred in small mops of diameter less than 0.5 m.

In the second test, there were no instances when the video record indicated the absence of eggs and the sidescan sonar imagery suggested their presence. There were six instances when the sidescan sonar imagery failed to register the presence of eggs that had been seen initially on the video record. The following comments were made on these instances during preparation of Test 2: 4–6 small patches *ca.* 0.5 m each; 1–2 very small egg patches; linear string of eggs; 1 patch *ca.* 10 capsules; 2 patches *ca.* 1 m; and 1 small patch. In four of these cases, the egg mops were, at most, 0.5 m in diameter. In the other cases, the linear string of eggs was missed, possibly because of its unusual shape; and in the other case, of two patches *ca.* 1 m each, possibly because of inaccurate positioning.

B. Size detectability

In view of the failed examples in the two tests, it appears that egg mops smaller than about 0.5 m cannot be detected with the system as currently configured and used. This approximate detection limit applies to the use of a 400-kHz sidescan sonar of 0.5-deg beamwidth when towed at 3-knot speed with a ping rate of 13/s. The resolution is about 10–20 cm out to about the 25-m range on either side of the towfish. Thus, an object of 50-cm diameter will be spanned by about 3–5 pixels, with corresponding size in the image. This number is evidently too small to resolve squid egg beds.

The present analysis has only attempted to distinguish the presence and absence of squid eggs. Observed aggregations of eggs ranged in size from roughly circular mops smaller than 0.5 m to much larger, irregularly shaped clusters of beds. Two such aggregations were measured according to their sidescan sonar image; one was roughly elliptical in shape, with axes 2.7 and 7.4 m; another was cross-shaped, with similar 5-m axes. Egg mops greater than 0.5 m and egg beds greater than 1 m have been detected by the sidescan sonar imagery.

Other organisms were also observed in the video record. Examination of the sidescan sonar images at the corresponding locations has failed to reveal identified individual drift kelp fronds (*Macrocystis pyrifera*) and sea stars, e.g., *Pycnopodia helianthoides* and *Asterina miniata*. It is appreciated that these were typically below the detectability size limit, although some kelp strands and the largest *Pycnopodia* sea stars exceeded 0.5 m and still did not appear as distinctive features in the acoustic records. The low vertical relief of these targets was probably the primary reason that the sidescan sonar failed to effectively image them.

C. Positioning issues when comparing diverse data

Comparison of the sonar and video data, which were collected on different days from different submerged platforms, has also required a closer look at the issues of positioning accuracy and precision. While differential GPS was used, this is updated only at intervals, with an intrinsic accuracy of about ±1–2 m in the Monterey Bay region. The accuracy in positioning the sidescan sonar towfish (Sec. IV A 1) is poorer since it is towed, and its position must be estimated from the amount of cable deployed and its depth. Further, the towfish is subject to accelerations due to wave action on the towing vessel, which can change the velocity and position of the towfish relative to the dGPS receiver. Making allowance for this, inaccuracies in towfish positioning can be ±5 m, depending on the exact circumstances of towing, including sea state, currents, and direction of ship movement. The accuracy in positioning the ROV-borne video camera is better than that of the towfish, for the ROV is decoupled from vessel motions by having a slack tether, and the ROV is acoustically tracked from the vessel. Thus the positions of the towfish and ROV-borne video camera can each be known to within about ±1–2 m under good conditions, but closer to ±5 m under poorer conditions, as with a fresh breeze. In addition, the camera height and orientation influences the field of view, which can differ from the position itself by several meters. Under the worst circumstances, the combined uncertainty of these two can be as much as ±10 m. In comparing the sonar and video observations, agreement was sought to within 3–5 m, occasionally up to about 6–7 m.

Performance of mosaicking also requires comparison of data from transect to transect, if of similar origin. Clues to positioning inaccuracy are evident in the sidescan sonar record. Distortions may be noticed, as in stretched egg bed features in some images. The process of mosaicking can be improved, but the experience of fine-scale optical mosaicking in the laboratory indicates that this is an intricate problem that is inherently three-dimensional in character.[51] The use of terrain constraints can significantly improve underwater mosaicking, whether optical or acoustical, if the number of images to be combined is not excessive (C. Roman, pers. comm.).

D. An abundance estimation

The abundance of squid eggs was estimated for a particular quadrat, yielding the number 3.65×10^7. This quantity is not dissimilar from an estimation performed in a different quadrat the preceding year. This is the first numerical estimate of egg abundance over a region of interest by a rapid, remote, synoptic, noninvasive method. Extension of the quadrat-based estimation to a larger survey area is straightforward.

The authors know of no other acoustic estimate of the abundance of benthic eggs of any squid species. The authors know of two studies reporting abundance estimates of benthic eggs of squid species, but based on SCUBA-diver surveys using principles of random or nonrandom sampling. In a study by Sauer *et al.*,[44] two basic abundance estimates of eggs of *Loligo vulgaris reynaudii* were derived, distinguished by the respective statistical analyses: 3.162×10^9 and 1.290×10^8 eggs over respective areas of 74.36 and 1.646 km^2. Corresponding numerical densities were 42.52 eggs/m^2 in the larger area and 78.32 eggs/m^2 in the smaller area. In a study by Moltschaniwskyj and Pecl,[52] abundance estimates of benthic eggs of southern calamary (*Sepioteuthis australis*) were derived for two different bays in each of two years. The numbers for one bay were 7.68×10^6 and 1.14×10^7 eggs over respective areas of 3.67 and 4.19 ha, and 2.47×10^6 and 1.43×10^6 eggs over respective areas of 1.35 and 1.36 ha. The corresponding numerical densities were 209 and 272 eggs/m^2 for the first bay and 182 and 105 eggs/m^2 for the second. These numbers are compared with the numerical density of *Loligo opalescens* eggs determined by the acoustic method reported here, namely 47 720 eggs/m^2, that is, about three orders of magnitude greater, although estimated over an area that is less than 1/1000 of the areas in the first study and 1/10 of the areas in the second study. Another major difference is represented by the relative areal coverage. This was partial in the SCUBA-diver surveys, but total in the present acoustic survey using sidescan sonar.

E. Future work

It should be possible to resolve squid egg beds of dimensions smaller than 0.5 m, as with a more directional, higher-frequency sidescan sonar, with a higher ping rate and a smaller maximum range than was used in the reported work. This would be very useful for extending the detection and identification capability of the method, hence its quantification capability as well. Distinguishing other benthic organisms, e.g., kelp and starfish, would also be useful.

It would be interesting and potentially useful to perform sidescan sonar surveying from other platforms, especially from autonomous underwater vehicles (AUVs). The example of the Remotely Environmental UnitS (REMUS) AUV[53] comes to mind as a particularly attractive vehicle because it carries sidescan sonars on port and starboard sides as standard equipment. The operating frequency of these is either 600 or 900 kHz.

Automatic recognition of squid egg beds on the sidescan sonar image should be possible, as should computation of areas covered by the egg beds. However, can this be done reliably, accurately and with minimal operator intervention?

Combining observation of squid egg beds with that of adult squid in the water column is also important. Acoustic measurement of squid in the water column is eminently feasible, as demonstrated through a number of works cited in Sec. I B. In this way, local population recruitment could be measured directly, and potential future recruitment could be estimated by quantification of the egg beds. The complex of interactions that govern the success of recruitment, including the known attractive effects of egg beds, could help gauge these components as well as others used by fishery managers and population biologists.

It is expected that some basic questions on the biology of *Loligo opalescens* may be answered through the extended use of acoustic methods. These include, for example, questions on the geographical distribution of egg beds and their association with the benthic habitat. Statistical properties of aggregation can be determined by application of the variogram, the basic structural tool of geostatistics.[54,55] The potential of acoustics for monitoring extent and rate of egg deposition on the squid spawning grounds is apparent, especially with regard to seasonal and yearly fluctuations that could be correlated eventually with fishery catch records of adults. An example of this approach is reported by Moltschaniwskyj and Pecl,[52] mentioned in Sec. IX D, who used SCUBA in shallow water to count small egg cases of *Sepioteuthis* in sea grass. The approach may serve the needs of both managers responsible for the squid fishery and scientists trying to understand the dynamics of squid spawning during an ongoing fishery.

It is a useful exercise to estimate the degree of acoustic coverage that can be achieved by sidescan sonar in a period of hours. If the full track width of sidescan sonar coverage is 100 m and 100% overlap is assumed on adjacent, port or starboard parallel tracks, then at a vessel speed of 3 knots, a 5.4-km long transect of effective area 0.27 km^2 can be covered in 1 h, 2.12 km^2 in 8 h. This is a sizable fraction of the total estimated area of the primary spawning grounds in southern Monterey Bay, namely 10 km^2.

A fundamental acoustic problem is also waiting to be solved, namely that of determining the backscattering cross section of individual squid egg capsules and how this changes with development phase. This problem might be approached through numerical solution of the wave equation by the finite-element method[56,57] but as applied to acoustic scattering problems, as in the boundary-element method, e.g., Ref. 58, or infinite-element method, e.g., Ref. 59. Data on the physical properties of individual egg capsules, namely mass density and compressibility, would be required. The scattering problem could also be addressed by measurement, but under controlled conditions.

A second outstanding acoustic problem is modeling scattering from an egg mop or bed. The morphology of the upper surface of a mop or bed is known to be knobbly, with an amplitude of unevenness of order of 1 cm. Interstices are present between neighboring egg capsules. Egg mops and beds may also bend under the influence of currents, including surface-wave action. An appropriate theory of acoustic scattering by such a surface may resemble that for sound scattering by sea ice dendrites at the air–water interface.[60]

Development of a method for calibrating sidescan sonar would also be useful. If the standard-target method[61–63] could be extended to sidescan sonar, as has recently been accomplished for multibeam sonar,[64] then the measurements could be performed in an absolute sense. Potential benefits would include demonstrable data quality and maintenance of the same over time, as well as a capability for the intercomparison of data collected with different sidescan sonars.

X. CONCLUSIONS

(1) Egg beds of *Loligo opalescens* in Monterey Bay can be detected, identified, and quantified by high-frequency sidescan sonar imagery.

(2) The lower size limit of detectability of squid egg beds by a 400-kHz sidescan sonar is about 0.5 m.

(3) The method is ready for monitoring applications.

ACKNOWLEDGMENTS

The authors acknowledge the contributions of many colleagues and organizations. C. Gubala (JC Headwaters Canada) is thanked for lending and operating an EY echo sounder during the first, laboratory-based investigation. A. Henry (California Department of Fish and Game) is thanked for valuable support, participation in the first cruise, and facilitating use of R/V Mako, with the following officers and crew: Captain M. Kibby, Engineer R. L. Michalski, R. Hornady, J. DeWitt, T. Tanaka. The following are also thanked for their participation in this first cruise: C. Chan and T. Wadsworth (CDFG); and D. Sullivan, A. Hochstaedter, Y. Yokozawa, and J. Zande (Monterey Peninsula College). Contributions by the following students are acknowledged: A. Rupp (California State University Monterey Bay), and G. Dayhuff, M. Robinson, J. Kibele, D. Williams, S. Okano, and N. Capps (MPC). The following SCUBA divers are thanked for their vital underwater labors: R. Hornady, H. King, C. Dawson, and D. Osorio (CDFG); and S. Clabuesch (University of California at Santa Cruz). G. Shipton (Triton Elics International) is thanked for preparing the sidescan sonar, and J. Condiotty (Simrad) for arranging a loan of the EK60 echo sounder. M. Windham (CDFG) is thanked for logistical support. S. Fangman, NOAA Channel Islands National Marine Sanctuary, is thanked for valuable support, including facilitating the use of R/V Shearwater during the second cruise, with NOAA captains L. Moody and T. Shinn, as well as personal participation during the cruise. CDFG is again thanked for allowing the participation of R. L. Michalski, T. Bishop, K. M. O'Brien, L. M. Laughlin, and D. Porzio during the second cruise. D. Vasey, Santa Barbara City College, is thanked for vital scientific ROV support, as well as allowing the following students to impart their general seagoing expertise in the scientific operations of the cruise: D. Adams, A. Sensabaugh, J. Valenzuela, and R. Remley. M. Parmenter, C. Sellers, and K. Buresch are all thanked for contributions to the figures. The authors are grateful for funding from the National Sea Grant, Essential Fish Habitat Program, and especially the interest of program manager E. Anderson, Sea Grant Project No. NA16RG2273. This is Woods Hole Oceanographic Institution contribution number 11372.

[1] P. R. Boyle and S. Boletzky, "Cephalopod populations: definitions and dynamics," Philos. Trans. R. Soc. London, Ser. B **351**, 985–1002 (1996).

[2] G. V. Morejohn, J. T. Harvey, and L. T. Krasnow, "The importance of *Loligo opalescens* in the food web of marine vertebrates in Monterey Bay, California," in *Biological, Oceanographic, and Acoustic Aspects of the Market Squid, Loligo opalescens Berry*, edited by C. W. Recksiek and H. W. Frey, Calif. Dep. Fish Game Fish Bull. **169**, 67–98 (1978).

[3] W. G. Fields, "The structure, development, food relations, reproduction, and life history of the squid *Loligo opalescens* Berry," Fish. Bull. **131**, 1–108 (1965).

[4] C. M. Dewees and R. J. Price, "Overview of the squid fishery on the Pacific coast of the United States," in *Proceedings of the International Squid Symposium*, 9–12 August 1981, *Boston, Massachusetts* (New England Fisheries Development Found., Boston, 1982), pp. 197–212.

[5] M. Vojkovich, "The California fishery for market squid (*Loligo opalescens*)," CalCOFI Rep. **39**, 55–60 (1998).

[6] California Department of Fish and Game, "Market squid fishery management plan: draft," State of California, The Resources Agency, Department of Fish and Game, Marine Region, 7 July 2003.

[7] B. J. Macewicz, J. R. Hunter, N. C. H. Lo, and E. L. LaCasella, "Fecundity, egg deposition, and mortality of market squid (*Loligo opalescens*)," Fish. Bull. **102**, 306–327 (2004).

[8] W. H. H. Sauer, M. J. Smale, and M. R. Lipinski, "The location of spawning grounds, spawning and schooling behaviour of the squid *Loligo vulgaris reynaudii* (Cephalopoda: Myopsida) off the Eastern Cape Coast, South Africa," Mar. Biol. (Berlin) **114**, 97–107 (1992).

[9] J. K. T. Brodziak and A. A. Rosenberg, "A method to assess squid fisheries in the north-west Atlantic," ICES J. Mar. Sci. **50**, 187–194 (1993).

[10] G. J. Pierce, N. Bailey, Y. Stratoudakis, and A. Newton, "Distribution and abundance of the fished population of *Loligo forbesi* in Scottish waters: analysis of research cruise data," ICES J. Mar. Sci. **55**, 14–33 (1998).

[11] D. J. Agnew, R. Baranowski, J. R. Beddington, S. des Clers, and C. P. Nolan, "Approaches to assessing stocks of *Loligo gahi* around the Falkland Islands," Fish. Res. **35**, 155–169 (1998).

[12] S. J. Walsh, P. A. Koeller, and W. D. McKone, eds. *Proceedings of the International Workshop on Survey Trawl Mensuration. Northwest Atlantic Fisheries Centre, St. John's, Newfoundland, March 18–19, 1991*, Canadian Tech. Rep. Fish. Aquat. Sci. **1911**, 1–114 (1993).

[13] D. R. Gunderson, *Surveys of Fisheries Resources* (Wiley, New York, 1993).

[14] T. Okutani and J. McGowan, "Systematics, distribution, and abundance of the epiplanktonic squid (Cephalopoda, Decapoda) larvae of the California Current, April, 1954–March, 1957," Bull. Scripps. Inst. Oceanogr. **14**, 1–90 (1969).

[15] M. R. Maxwell, A. Henry, C. D. Elvidge, J. Safran, V. R. Hobson, I. Nelson, B. T. Tuttle, J. B. Dietz, and J. R. Hunter, "Fishery dynamics of the California market squid (*Loligo opalescens*), as measured by satellite remote sensing," Fish. Bull. **102**, 661–670 (2004).

[16] M. Clarke, L. Allcock, and M. B. Santos, "Estimating cephalopod biomass: workshop report," Bull. Mar. Sci. **71**, 47–65 (2001).

[17] G. M. Cailliet and D. L. Vaughan, "A review of the methods and problems of quantitative assessment of *Loligo opalescens*," Biol. Oceanogr. **2**, 379–400 (1983).

[18] K. G. Foote, "Quantitative fisheries research surveys, with special reference to computers," in *Computers in Fisheries Research*, edited by B. A. Megrey and E. Moksness (Chapman and Hall, London, 1996), pp. 80–112.

[19] R. M. Starr and R. E. Thorne, "Acoustic assessment of squid stocks," in *Squid Recruitment Dynamics. The Genus Illex As a Model, the Commercial Illex Species and Influences on Variability*, edited by P. G. Rodhouse, E. G. Dawe, R. K. O'Dor, FAO Fish. Tech. Pap. **376**, 181–198 (1998).

[20] C. Goss, D. Middleton, and P. Rodhouse, "Investigations of squid stocks using acoustic survey methods," Fish. Res. **54**, 111–121 (2001).

[21] M. J. Roberts, M. Barange, M. R. Lipinski, and M. R. Prowse, "Direct hydroacoustic observations of chokka squid *Loligo vulgaris reynaudii* spawning activity in deep water," S. Afr. J. Mar. Sci. **24**, 387–393 (2002).

[22] A. Kawabata, "Target strength measurements of suspended live ommastrephid squid, *Todarodes pacificus*, and its application in density estimations," Fish. Sci. **71**, 63–72 (2005).

[23] D. L. Vaughan and C. W. Recksiek, "An acoustic investigation of market squid, *Loligo opalescens*," in *Biological, Oceanographic, and Acoustic Aspects of the Market Squid, Loligo opalescens Berry*, edited by C. W. Recksiek and H. W. Frey, Calif. Dep. Fish Game Fish Bull. **169**, 135–147 (1978).

[24] D. L. Vaughan and C. W. Recksiek, "Detection of market squid, *Loligo opalescens*, with echo sounders," CalCOFI Rep. **20**, 40–50 (1979).

[25] K. Jefferts, J. Burczynski, and W. G. Pearcy, "Acoustical assessment of squid (*Loligo opalescens*) off the Central Oregon coast," Can. J. Fish. Aquat. Sci. **44**, 1261–1267 (1987).

[26] J. E. Ehrenberg, "A comparative analysis of in situ methods for directly measuring the acoustic target strength of individual fish," IEEE J. Ocean. Eng. **OE-4**(4), 141–152 (1979).

[27] C. W. Recksiek and H. W. Frey, in *Biological, Oceanographic, and Acoustic Aspects of the Market Squid, Loligo opalescens Berry*, Calif. Dep. Fish Game Fish Bull. **169** (1978).

[28] R. F. Hixon, "*Loligo opalescens*," in *Cephalopod Life Cycles, Vol. I, Species Accounts*, edited by P. R. Boyle (Academic, London, 1983), pp. 95–114.

[29] G. D. Jackson, "Statolith age estimates of the loliginid squid *Loligo opalescens* (Mollusca: Cephalopoda): Corroboration with culture data," Bull. Mar. Sci. **54**, 554–557 (1994).

[30] J. Butler, D. Fuller, and M. Yaremko, "Age and growth of market squid (*Loligo opalescens*) off California during 1998," CalCOFI Rep. **40**, 191–195 (1999).

[31] L. D. Zeidberg and W. M. Hamner, "Distribution of squid paralarvae, *Loligo opalescens* (Cephalopoda: Myopsida), in the southern California Bight in the three years following the 1997–1998 El Nino," Mar. Biol. (Berlin) **141**, 111–122 (2002).

[32] E. S. Hobson, "Spawning in the Pacific coast squid *Loligo opalescens*," Underwat. Nat. **3**, 20–21 (1965).

[33] A. C. Hurley, "Mating behavior of the squid *Loligo opalescens*," Mar. Behav. Physiol. **4**, 195–203 (1977).

[34] R. T. Hanlon, "Mating systems and sexual selection in the squid *Loligo*:

How might commercial fishing on spawning squids affect them?" CalCOFI Rep. **39**, 92–100 (1998).

[35] R. R. Leos, "The biological characteristics of the Monterey Bay squid catch and the effect of a two-day-per-week fishing closure," CalCOFI Rep. **39**, 204–211 (1998).

[36] J. W. Forsythe, N. Kangas, and R. T. Hanlon, "Does the California Market Squid, *Loligo opalescens*, spawn naturally during the day or at night? A note on the successful use of ROVs to obtain basic fisheries biology data," Fish. Bull. **102**, 389–392 (2004).

[37] R. T. Hanlon, N. Kangas, and J. W. Forsythe, "Egg capsule deposition and how behavioral interactions influence spawning rate in the squid *Loligo opalescens* in Monterey Bay, California," Mar. Biol. (Berlin) **145**, 923–930 (2004).

[38] A. Okabe, B. Boots, K. Sugihara, and S. N. Chiu, *Spatial Tessellations: Concepts and Applications of Voronoi Diagrams* (Wiley, Chichester, 2000).

[39] J. A. McGowan, "Observations on the sexual behavior and spawning of the squid, *Loligo opalescens*, at La Jolla, California," Calif. Fish and Game **40**, 47–54 (1954).

[40] L. D. Zeidberg, W. Hamner, K. Moorehead, and E. Kristof, "Egg masses of *Loligo opalescens* (Cephalopoda: Myopsida) in Monterey Bay, California following the El Nino event of 1997–1998," Bull. Mar. Sci. **74**, 129–141 (2004).

[41] P. G. Rodhouse, E. G. Dawe, and R. K. O'Dor, in *Squid Recruitment Dynamics. The Genus Illex as a Model, the Commercial Illex Species and Influences on Variability*, FAO Fish. Tech. Pap. **376** (1998).

[42] J. P. Fish and H. A. Carr, *Sound Underwater Images, A Guide to the Generation and Interpretation of Side Scan Sonar Data*, 2nd ed. (Lower Cape Publishing, Orleans, MA, 1990).

[43] J. P. Fish and H. A. Carr, *Sound Reflections, Advanced Applications of Side Scan Sonar* (Lower Cape Publishing, Orleans, MA, 2001).

[44] W. H. H. Sauer, C. McCarthy, M. J. Smale, and A. S. Koorts, "An investigation of the egg distribution of the chokka squid, *Loligo vulgaris reynaudii*, in Krom Bay, South Africa," Bull. Mar. Sci. **53**, 1066–1077 (1993).

[45] L. N. Andersen, "The new Simrad EK60 scientific echo sounder system," J. Acoust. Soc. Am. **109**, 2336 (2001).

[46] H. Bodholt, H. Nes, and H. Solli, "A new echo-sounder system," Proc. Inst. Acoust. **11**(3), 123–130 (1989).

[47] K. G. Foote and G. Stefánsson, "Definition of the problem of estimating fish abundance over an area from acoustic line-transect measurements of density," ICES J. Mar. Sci. **50**, 369–381 (1993).

[48] H. R. Skjoldal, P. H. Wiebe, and K. G. Foote, "Sampling and experimental design," in *ICES Zooplankton Methodology Manual*, edited by R. Harris, P. Wiebe, J. Lenz, H. R. Skjoldal, and M. Huntley (Academic, San Diego, 2000), pp. 33–53.

[49] J. Breman, ed. *Marine Geography: GIS for the Oceans and Seas* (ESRI Press, Redlands, CA, 2002).

[50] J. H. Zar, *Biostatistical Analysis*, 4th ed. (Prentice-Hall, Upper Saddle River, NJ, 1999).

[51] R. Preston, "Capturing the unicorn," The New Yorker **81**(8), 28–33 (2005).

[52] N. A. Moltschaniwskyj and G. T. Pecl, "Small-scale spatial and temporal patterns of egg production by the temperate lolilginid squid *Sepioteuthis australis*," Mar. Biol. (Berlin) **142**, 509–516 (2003).

[53] B. R. Allen, R. Stokey, T. Austin, N. Forrester, R. Goldsborough, M. Purcell, and C. von Alt, "REMUS: a small, low cost AUV; system description, field trials and performance results," *Proc. MTS/IEEE Oceans'97 Conf.*, Vol. **2**, pp. 994–1000 (1997).

[54] N. A. C. Cressie, *Statistics for Spatial Data* (Wiley, New York, 1991).

[55] J. Rivoirard, J. Simmonds, K. G. Foote, P. Fernandes, and N. Bez, *Geostatistics for Estimating Fish Stock Abundance* (Blackwell Science, Oxford, 2000).

[56] O. C. Zienkiewicz and R. L. Taylor, *The Finite Element Method*, 5th ed, (Butterworth Heinemann, Oxford, 2000).

[57] D. S. Burnett, *Finite Element Analysis: from Concepts to Applications* (Addison-Wesley, Reading, MA, 1988).

[58] D. T. I. Francis, "A gradient formulation of the Helmholtz integral equation for acoustic radiation and scattering," J. Acoust. Soc. Am. **93**, 1700–1709 (1993).

[59] D. S. Burnett, "A three-dimensional acoustic infinite element based on a prolate spheroidal multipole expansion," J. Acoust. Soc. Am. **96**, 2798–2816 (1994).

[60] T. K. Stanton, K. C. Jezek, and A. J. Gow, "Acoustical reflection and scattering from the underside of laboratory grown sea ice: Measurements and predictions," J. Acoust. Soc. Am. **80**, 1486–1494 (1986).

[61] K. G. Foote, "Optimizing copper spheres for precision calibration of hydroacoustic equipment," J. Acoust. Soc. Am. **71**, 742–747 (1982).

[62] K. G. Foote, "Maintaining precision calibrations with optimal copper spheres," J. Acoust. Soc. Am. **73**, 1054–1063 (1983).

[63] K. G. Foote, H. P. Knudsen, G. Vestnes, D. N. MacLennan, and E. J. Simmonds, "Calibration of acoustic instruments for fish density estimation: a practical guide," ICES Coop. Res. Rep. **144** (1987), 69 pp.

[64] K. G. Foote, D. Chu, T. R. Hammar, K. C. Baldwin, L. A. Mayer, L. C. Hufnagle, Jr., and J. M. Jech, "Protocols for calibrating multibeam sonar," J. Acoust. Soc. Am. **117**, 2013–2027 (2005).